

Astrophysics of Stellar Multiple Systems

By

Kyle E. Conroy

Dissertation

Submitted to the Faculty of the  
Graduate School of Vanderbilt University  
in partial fulfillment of the requirements  
for the degree of

DOCTOR OF PHILOSOPHY  
in  
Physics

May 11, 2018

Nashville, Tennessee

Approved:

Keivan G. Stassun, Ph.D.

Andrej Prša, Ph.D.

David A. Weintraub, Ph.D.

Andreas A. Berlind, Ph.D.

## DEDICATION

To my family — for supporting me and my decisions to pursue astronomy over the past decade. Without your love and support, this would not have been possible.

To my committee — Keivan Stassun, Andrej Prša, David Weintraub, and Andreas Berlind — for all your advice, comments, patience, and time. It has been comforting to know that I could count on all four of you to make sure I would eventually finish.

To Keivan — for giving me the freedom to occasionally go down the “rabbit hole” and get stuck in many dead ends while still providing very helpful advice and making sure I eventually climb out, and for always having your door open and willing to put everything aside to read a draft at a moments notice.

To Andrej — for believing in me and tolerating working with me for all these years.

To my fellow graduate students, collaborators, and friends — Michael Lund, Joseph Rodriguez, Ryan Nicholl, Erica Fey, Nick Chason, Savannah Jacklin, Kelly Hambleton, Martin Horvat, Angela Kochoska, Meagan Lang, Christina Davis, Nicole Sanchez, Anna Egner, Gabriella Alvarez, Jared Coughlin, and Cindy Villamil — for very helpful discussions and support, both scientific and not, throughout this journey. I could not have remained sane without all y’all.

## ACKNOWLEDGMENTS

K. E. Conroy has been supported under NASA NESSF Fellowship NNX15AR87H and NASA ADAP grant NNX12AE22G.

The cataloging of Eclipsing Binaries in the *Kepler* data set was funded in part by *Kepler* Participating Scientist Award NSR303065, NASA/Caltech subcontract 2-1085696, NASA/SETI subcontract 08-SC-1041, and NSF RUI AST-05-07542. Spectroscopic follow-up was possible through NOAO survey program 11A-0022. Without this database of binaries, detecting triple star candidates would not have been possible. Thanks to the approximately 80 members of the *Kepler* Eclipsing Binaries working group as well as everyone at NASA who made *Kepler* possible.

The development of PHOEBE 2, which was necessary in order to build the framework for modeling triple stars, was funded from the NSF AAG grant #1517474 and was a massive undertaking over many years and collaborators, including: Andrej Prša, Martin Horvat, Pieter Degroote, Steven Bloemen, Gal Matijević, Herbert Pablo, Angela Kochoska, Joseph Giammarco, and Kelly Hambleton.

This research has made use of NASA's Astrophysics Data System as well as the NASA Exoplanet Archive, which is operated by the California Institute of Technology, under contract with the National Aeronautics and Space Administration under the Exoplanet Exploration Program.

## TABLE OF CONTENTS

	Page
DEDICATION . . . . .	ii
ACKNOWLEDGMENTS . . . . .	iii
LIST OF TABLES . . . . .	vii
LIST OF FIGURES . . . . .	viii
LIST OF ABBREVIATIONS . . . . .	x
Chapter	
1 Introduction . . . . .	1
1.1 Precise Constraints on Physical Parameters . . . . .	2
1.2 Probing Formation and Evolution Theories . . . . .	3
2 Detection and Cataloging of <i>Kepler</i> and K2 Eclipsing Binaries . . . . .	6
2.1 Identification of Eclipsing Binary Signals . . . . .	7
2.2 Data Detrending . . . . .	9
2.3 Determining Ephemerides . . . . .	10
2.3.1 Sources with Multiple Ephemerides . . . . .	12
2.4 Fitting a Deconvolved Analytic Function . . . . .	12
2.5 Morphology Classification . . . . .	14
2.6 Spectroscopic Follow-Up . . . . .	17
2.7 Distributions . . . . .	18
3 Considerations for Modeling Eclipsing Binaries in the <i>Kepler</i> Era . . . . .	22
3.1 Dynamics and Light Time Effects . . . . .	23
3.2 Surface Discretization . . . . .	24
3.2.1 Surface Offsetting . . . . .	27
3.3 Volume Conservation in Eccentric Orbits . . . . .	27

3.4 Sampling Local Quantities . . . . .	29
3.5 Eclipse Detection . . . . .	30
4 Identification of Triple and Multiple Systems via Eclipse Timing Variations . . . . .	34
4.1 Measuring Eclipse Times . . . . .	35
4.1.1 Dealing with Sources of Spurious ETV Signals . . . . .	37
4.2 Identifying Candidate Triple and Higher-Order Systems . . . . .	40
4.2.1 Higher-Order Systems . . . . .	46
4.2.2 Systems Confirmed through Eclipse Events . . . . .	47
4.3 Statistics . . . . .	48
5 Astrophysical Contributions to Eclipse Timing Variations . . . . .	52
5.1 Apsidal Motion . . . . .	52
5.2 Mass Transfer . . . . .	54
5.3 Applegate Effect . . . . .	55
5.4 Dynamical Effects . . . . .	56
5.5 Parallax and Proper Motion Effects . . . . .	57
5.6 Rømer Delay . . . . .	58
5.7 Light Travel Time Effect . . . . .	59
5.8 Shklovskii Effect . . . . .	60
5.9 Barycentric and Asymmetric Transverse Velocities . . . . .	61
5.9.1 General Theory . . . . .	61
5.9.2 Application to Keplerian Orbits . . . . .	64
5.9.3 Expected Contribution from GAIA Proper Motions . . . . .	65
5.9.4 Constant Shift in Phase-Separation Between Eclipses . . . . .	67
5.9.5 Eccentric Systems with Apsidal Motion . . . . .	70
5.9.6 Binary System with Change in Inclination . . . . .	74
5.9.7 Hierarchical Triple Systems . . . . .	76
5.9.8 Comparison of Contributions of Effects . . . . .	78

<b>6 Robust Modeling of Stellar Triples</b>	<b>84</b>
6.1 Defining the System Hierarchy	85
6.2 Dynamics	86
6.3 Stellar Surface Distortion	88
6.4 Eclipse Detection	90
6.5 Modeling Eclipse Timing Variations	91
6.6 Justification of Assumptions	93
6.6.1 Point Masses	93
6.6.2 Distortion Between Pairs	94
6.6.3 Fixed Rotation Periods	95
6.6.4 Instantaneous Keplerian Orbits	96
6.7 Utilizing Multiple Backends	96
<b>7 Discussion and Conclusions</b>	<b>98</b>
<b>Appendix</b>	
<b>Appendix A Orbital Elements for BATV</b>	<b>100</b>
<b>REFERENCES</b>	<b>102</b>

## LIST OF TABLES

Table	Page
2.1 Properties of extraneous eclipse/transit events in the <i>Kepler</i> sample. . . . .	12
2.2 Systems exhibiting multiple ephemerides in the <i>Kepler</i> sample. . . . .	13
4.1 ETVs with Parabolic Signals . . . . .	42
4.2 ETVs with Potential Third-Body Signals . . . . .	43
4.3 ETVs crossmatched with Rappaport et al. (2013) . . . . .	44
5.1 Adopted values and computed amplitudes for known apsidal motion binaries	74

## LIST OF FIGURES

Figure	Page
2.1 Fitting a baseline to the <i>Kepler</i> light curve . . . . .	10
2.2 Detrended <i>Kepler</i> light curve . . . . .	11
2.3 Deconvolved analytic functions for phased <i>Kepler</i> light curves . . . . .	14
2.4 Spline fit to the LLE manifold . . . . .	15
2.5 Example light curves of different morphology classifications . . . . .	16
2.6 EB occurrence rate as a function of galactic latitude . . . . .	19
2.7 Distribution of orbital periods of <i>Kepler</i> EBs . . . . .	19
3.1 Trapezoidal vs triangulated meshes used within PHOEBE 2 . . . . .	25
3.2 Trapezoidal vs triangulated meshes for contact systems . . . . .	26
3.3 Horizon of a Roche star as determined by PHOEBE 2 . . . . .	28
3.4 Eclipse detection within PHOEBE 2 . . . . .	32
4.1 Determining eclipse bounds from polyfits . . . . .	35
4.2 Fitting eclipse times to light curve data . . . . .	36
4.3 Computing ETVs over an entire phase . . . . .	38
4.4 Anti-phase effect in ETVs . . . . .	39
4.5 Selection of ETV signals better fit by a quadratic ephemeris than an LTTE fit	41
4.6 Gallery of select ETV signals found in close binaries with LTTE fits . . . .	45
4.7 ETV signals for candidate higher-order systems . . . . .	46
4.8 KIC 2856960: triple system with both ETVs and extra eclipse events . . . .	47
4.9 KIC 2835289: triple system with both ETVs and a single extra eclipse event	48
4.10 Distribution of period of potential third body companions verses the inner-binary period and morphology . . . . .	49

5.1	Schematic representation of the effect BATV has on observed eclipse times	62
5.2	Distribution of expected transverse velocities from GAIA DR1 . . . . .	66
5.3	Schematic representation of BATV affecting phase-separation between primary and secondary eclipses . . . . .	67
5.4	Change in eclipse separation caused by BATV for a circular binary as a function of the total mass and mass-ratio . . . . .	69
5.5	Change in transit separation caused by BATV for KELT-9b . . . . .	71
5.6	BATV amplitude for the apsidal motion case . . . . .	72
5.7	BATV amplitude for several known apsidal motion systems . . . . .	72
5.8	BATV amplitude for apsidal motion in exoplanet systems . . . . .	73
5.9	BATV amplitude for the change in inclination case . . . . .	76
5.10	BATV amplitude for the hierarchical triple case compared to LTTE . . . . .	79
5.11	Contribution to ETVs by both classical LTTE and BATV . . . . .	81
5.12	BATV amplitude for the hierarchical triple case compared to dynamical effects . . . . .	83
6.1	Schematic representation of the nested hierarchical parameterization of a triple system . . . . .	86
6.2	Schematic representation of light travel time corrections . . . . .	88
6.3	Schematic representation of the “hybrid” Roche distortion scheme . . . . .	90
6.4	ETVs as computed in PHOEBE 2 . . . . .	92
6.5	ETVs computed in PHOEBE 2 compared to analytical LTTE . . . . .	93
6.6	Light curve of an example triple system . . . . .	97

## LIST OF ABBREVIATIONS

- BATV Barycentric and Asymmetric Transverse Velocities
- BJD Barycentric Julian Date
- EB Eclipsing Binary
- EBF Eclipsing Binary Factory
- EPIC Ecliptic Plane Input Catalog
- ETV Eclipse Timing Variation
- KCTF Kozai-Lidov Cycles and Tidal Friction
- KIC *Kepler* Input Catalog
- LC Light Curve
- LLE Locally Linear Embedding
- LSST Large Synoptic Survey Telescope
- LTTE Light Travel Time Effect
- MCMC Markov Chain Monte Carlo
- RV Radial Velocity
- TCE Threshold Crossing Event
- TESS Transiting Exoplanet Survey Satellite
- WD Wilson-Devinney

# Chapter 1

## Introduction

Eclipsing Binary stars (EBs) are systems in which two stars orbit their common center of mass, in a plane such that the observer sees one star passing in front of the other, resulting in eclipses. These systems serve a crucial role in stellar astrophysics — providing one of the only fundamental ways to measure absolute masses, radii, temperatures, and luminosities of stars. As luminosities can directly be determined by modeling the system, the distance to an EB can be derived, without any calibrations, from a measured apparent magnitude (Guinan et al., 1998). EBs therefore provide essential calibrations to both the astrophysical distance ladder and stellar population studies.

Approximately 46% of all systems contain more than one stellar component (Tokovinin, 2014b). However, not all of these systems are in the correct plane to result in eclipses and not all exhibit periods short enough to be easily observed and detected. Nevertheless, there are a large number of bright EBs with relatively short periods that can easily be observed from the ground with a modest telescope. For this reason, and because of all the scientific benefits, EBs have historically been very well studied.

Only about 25% of binaries (i.e. 13% of all systems) contain more than two components (Tokovinin, 2014b). In order to be dynamically stable, the additional component(s) must be at a significantly wider separation and therefore longer period than the inner binary they orbit. Due to their scarcity relative to EBs and the increased complications in modeling the physics of these systems, triple and higher order systems are not nearly as well studied as EBs.

However, Tokovinin (2014b) found that more than 60% of short-period binaries (with periods less than 3 days) have tertiary companions, and Law et al. (2010) found that more than 80% of apparently ultra-wide binaries (Dhital et al., 2010) are in fact also hierarchical

triples (see also Stassun, 2012). As a general rule, systems can be dynamically stable if the outer period is  $\gtrsim 10$  times the inner period. Therefore, as many of these triple systems include short-period inner binaries, many dynamically stable triple systems can still have outer-periods within an observable timescale. Furthermore, these types of systems—with a short-period inner binary and a wide companion—are particularly interesting in testing formation and evolution theories of binary star systems.

With modern surveys — *Kepler* (Batalha et al., 2010; Borucki et al., 2011), *MOST* (Walker et al., 2003), *CoRoT* (Baglin, 2003), *Pan-Starrs* (Kaiser et al., 2002), *Gaia* (de Bruijne, 2012), *TESS* (Ricker et al., 2015), and *LSST* (Tyson and LSST, 2002), for example — covering a large number of sources over a long time-baseline, observations for these systems are becoming increasingly available. With the great improvements in observational precision brought on by these same missions, we now must look towards methods to improve our models to reap the full benefits that these systems and data provide.

### 1.1 Precise Constraints on Physical Parameters

Through careful observation and modeling of the photometric light curves and radial velocities of EBs, it is possible to measure the masses, radii, surface gravities, densities, and luminosities of both stars with a precision better than a few percent. For example, in two recent reviews of available benchmark-grade EBs at main-sequence/subgiant ages (Torres et al., 2010) and at pre-main-sequence ages (Stassun et al., 2014), mass and radius determinations were better than 3% accuracy for  $\sim 100$  main-sequence and  $\sim 15$  pre-main-sequence EBs, and as good as  $\sim 1\%$  in a few cases.

These benchmark systems play a critical role in stellar astrophysics: calibrating the mass-radius relationship, testing stellar evolution models, providing fundamental parameter for stellar objects across the main sequence, and calibrating the distance ladder. However, the accuracy obtained for these systems is pushing the limits of our models and comes at significant overhead. High-precision photometric and spectroscopic (radial velocity) data

are necessary along with a considerable manual effort to model these systems. The largest limitation in reaching an even higher precision is the inherent degeneracies in the non-linear parameter space of the physical model. These degeneracies result in significant correlations in the resulting fitted values, limiting our ability to improve on the parameter uncertainties.

In the case of higher order systems, especially those in which all components share the same orbital plane and are mutually eclipsing, these orbital and stellar parameters can be constrained to a much higher precision because these degeneracies can be broken by the highly unique scenarios of these mutual eclipse events. In the case of KOI-126, for example, Carter et al. (2011) used a photodynamical model of a hierarchical triple system to measure the masses to a precision of  $\sim 1\%$  and the radii to a precision of  $\sim 0.5\%$ . Similarly, for the case of the circumbinary planet system *Kepler* 16, Doyle et al. (2011) constrained the masses of both stars in the inner binary to within 0.5% and the radii to within 0.2%.

## 1.2 Probing Formation and Evolution Theories

In addition to this increased precision, the presence of additional bodies enables us to study and test the effects of their mutual gravitational influence. For example, eclipsing binaries in large photometric surveys exhibit a peak in the orbital period distribution on the order of 1 day (Devor, 2005; Paczyński et al., 2006; Derekas et al., 2007). Binary formation theory, however, struggles to explain the creation of these close binaries *in situ*, and capture seems unlikely to produce the large number of observed close binaries (Bonnell, 2001). Kozai-Lidov Cycles and Tidal Friction (KCTF) has been proposed as a formation mechanism for short-period binaries through the interaction with a third star on an eccentric and inclined orbit with respect to the inner-binary (Kozai, 1962; Lidov, 1962; Fabrycky and Tremaine, 2007; Naoz et al., 2013a). Fabrycky and Tremaine (2007) use simulations of systems undergoing KCTF to provide testable distributions in the final mutual inclination between the resulting close inner-binaries and their companions. By modeling systems

with these configurations, we can build a sample of observed mutual inclinations to test against the theoretical values to then conclude to what extent KCTF plays a role in the formation of close binary systems.

Kozai-Lidov cycles can occur in hierarchical three-body systems with eccentric (i.e., non-circular) outer orbits. Inner binaries in systems with mutual inclinations between the critical values of  $39.2^\circ$  and  $180^\circ - 39.2^\circ$  cannot maintain circular orbits. In these systems, Kozai-Lidov cycles will occur, causing oscillations in both the inner eccentricity and the mutual inclination angle (Kozai, 1962; Lidov, 1962; Fabrycky and Tremaine, 2007; Naoz et al., 2013a). At some points during these oscillations, the inner binary will be in a state of higher eccentricity, and tidal forces between the inner stars will increase during their nearest approach (periastron passage). These tidal forces in turn act to dampen the orbital eccentricity-inclination oscillations and to tighten and circularize the orbit (Kiseleva et al., 1998). Eventually the inner binary tightens enough that tidal forces dominate, and the eccentricity-inclination oscillations cease, resulting in a close binary in a circular orbit with a tertiary companion settled into a wide, eccentric, and inclined orbit.

Observational studies of triple star systems have argued that KCTF is not the primary mechanism for initially creating these close inner-binaries, but may likely be responsible for further tightening them to periods within a few days (Tokovinin, 2008). Tokovinin (2014a,b) also uses a statistical study of nearby F and G dwarf multiples to suggest that KCTF may be able to explain both an overabundance of inner-systems at short periods due to tightening. Thus, observationally, there is support for the idea that KCTF may be an important ingredient for understanding the eventual tightening of close binaries, if not their formation.

Recently, others have approached this three-body dynamical problem with different types of numerical approximations, yielding different observable predictions involving the mutual angle of inclination between the inner and outer orbits. In simulations, using the “test particle quadrupole” approximation, in which one of the components of the inner-

binary is approximated to be massless, Fabrycky and Tremaine (2007) found that inner binaries with final orbital periods between 3 and 10 days show the final mutual inclination between the inner and outer orbits for these systems peak around 40 and 140 degrees (see Figure 7 in Fabrycky and Tremaine, 2007). Teyssandier et al. (2013) found similar results, but with another peak around 90 degrees, for the case of an initially circular inner orbit. Most recently, Naoz and Fabrycky (2014) using the “eccentric Kozai-Lidov” approximation, which relaxes these assumptions and uses the octupole approximation, finds no peak at 90 degrees and only modest peaks at 40 and 140 degrees (see their Figure 5 and also Naoz et al. (2013a,b)), and overall a broad nearly featureless distribution of mutual inclination angles. Ensemble statistics of the mutual inclination angles for large numbers of triple systems, together with accurate measurement of the mutual inclination angle for individual case studies of benchmark triple systems, are needed to distinguish between these different theoretical predictions.

By detecting, categorizing, and robustly modeling stellar multiple systems, we can slowly build the statistical sample necessary for testing these distributions. The work in this dissertation is the first step in that process. §2 discusses the detection and cataloging of EBs in the *Kepler* data set. The necessary improvements and considerations needed to model the ultra-precise data from *Kepler* is discussed in §3, specifically the redesign and complete rewrite of the eclipsing binary modeling software, PHOEBE. §4 then discusses the identification of candidate triple systems among *Kepler* EBs via eclipse timing variations. The various astrophysical contributions to eclipse timings, including the theoretical formalism of a new effect, are discussed in §5. Lastly, the incorporation of support for both higher-order systems as well as eclipse timing variations into PHOEBE is presented in §6 before concluding in §7.

## Chapter 2

### Detection and Cataloging of *Kepler* and K2 Eclipsing Binaries

*This chapter includes excerpts and figures adapted from Kirk et al. (2016) and Conroy et al. (2014a), used with permission from The Astronomical Journal and the Publications of the Astronomical Society of the Pacific.*

NASA’s *Kepler* Space Telescope, launched in March 2009, provided essentially uninterrupted, ultra-high precision photometric coverage of  $\sim$ 200,000 objects within a  $105\text{ deg}^2$  field of view in the constellations of Cygnus and Lyra for four consecutive years. The details and characteristics of the instrument and observing program can be found in Batalha et al. (2010); Borucki et al. (2011); Caldwell et al. (2010); Koch et al. (2010). The primary mission was to detect exoplanets, but *Kepler* observations were also useful for many other fields of astronomy, including EBs.

In 2014, *Kepler* lost the ability to maintain its precise orientation due to the loss of two reaction wheels, and was transitioned to its re-purposed mission, K2. The K2 mission provides 80 days of continuous high-precision photometry across each of 10 fields in the ecliptic plane. Although the photometric precision compared to the original *Kepler* mission was expected to be slightly lower due to a decrease in pointing accuracy, K2 is still able to obtain data an order of magnitude better than is possible from the ground. With the upcoming TESS mission, EBs identified in K2 will become prime targets for further follow-up allowing us to extend the time baseline and continue searching for triple systems (stellar and substellar) through eclipse timing variations and searching for transiting events.

As a member of the *Kepler* Eclipsing Binary Working Group, I helped identify, catalog, and characterize EBs within the *Kepler* and K2 data sets (Prša et al., 2011a; Slawson et al., 2011; Matijević et al., 2012; Kirk et al., 2016; Conroy et al., 2014a; LaCourse et al.,

2015). The *Kepler* Eclipsing Binary catalog lists stellar parameters from the *Kepler* Input Catalog (KIC) and Ecliptic Plane Input Catalog (EPIC) augmented by: primary and secondary eclipse depth, eclipse width, separation between primary and secondary eclipses, ephemeris, morphological classification parameter, and principal parameters determined by geometric analysis of the phased light curve.

The online catalog, available at <http://keplerEBs.villanova.edu> and <http://keplerEBs.villanova.edu/k2>, provides a searchable database of all eclipsing binaries found in the *Kepler* and K2 data sets, respectively. For individual EB entries, the online catalog provides a summary of the EB’s physical properties, analysis plots, and provides the time-series data for download in various formats. In addition to the raw data, the detrended processed light curves (§2.2), the analytical polyfit (§2.4), and the eclipse timing variation data (§4), along with the suite of diagnostic figures are available for download. A static version of the online catalog associated with this paper is maintained at MAST at <https://archive.stsci.edu/>.

## 2.1 Identification of Eclipsing Binary Signals

Candidate EBs were identified from the  $\sim$ 200,000 *Kepler* sources through a variety of approaches and sources. (1) As a first cut, all light curves were visually inspected, flagging all eclipse-like signatures for further inspection. (2) We also examined all *Kepler* Objects of Interest (Mullally et al., 2015) — a list of detected planets and planet candidates — for planet false positives which may actually be EBs. (3) The Eclipsing Binary Factory (EBF) (Parvizi et al., 2014), a fully automated computational pipeline used to classify EB light curves, was trained on one of the earlier releases of the catalog and then used to later identify 68 candidate systems, of which 13 were validated and added to the catalog. (4) Identified transit events from Planet Hunters, a citizen science project (Fischer et al., 2012) that makes use of the Zooniverse toolset (Lintott et al., 2008) to serve flux-corrected light curves from the *Kepler* public release data, were examined for addition to the catalog.

In the K2 engineering target list, 9 objects (60017809, 60017810, 60017812, 60017814,

60017815, 60017816, 60017818, 60017821, 60017822) were identified as previously known EBs. One of these (60017818) did not show a clear EB in the 12 days of data, so was excluded, but the remaining 8 were all recovered independently. Since there are no Threshold Crossing Events (TCEs), manual inspection was the primary source of identifying new EB systems and in order to test the feasibility of automated detection of eclipsing binary signals in K2 data. Planet Hunters (Fischer et al., 2012) had independently detected and identified several of these EBs as well.

The EBs identified in the K2 dataset provide an initial benchmark set for newly developed pipelines intended for automated discovery of EBs from large datasets such as those that will be provided by the ongoing K2 mission. We applied the Eclipsing Binary Factory (EBF) pipeline (Parvizi et al., 2014) to the K2 light curves to test its ability to correctly recover these EBs. The EBF correctly recovered 92% of the manually identified K2 EBs with at least 90% confidence in the classification. This recovery rate is similar to that obtained by the EBF from the original Kepler data set, suggesting that automated methods such as the EBF are capable of identifying a large sample of EBs in the upcoming K2 campaigns with good completeness.

All candidate EBs were then processed through a custom-built pipeline and vetted for being false positives (e.g. a true binary signal but from a source outside the pixel mask or target, see Kirk et al. (2016) for more details). Whenever possible, the original target of the signal was identified and a new mask was created from the raw pixel-level data to extract the correct light curve (Abdul-Masih et al., 2016). These re-extracted entries are available separately from the main catalog at <http://keplerEBs.villanova.edu/indirect>.

The resulting 2876 systems in the original *Kepler* mission, 31 in the K2 Engineering data set (Conroy et al., 2014a), 207 in K2 campaign 0 (LaCourse et al., 2015), and approximately 1000 in campaigns 1-10 are likely EBs — although we note that any individual case cannot be confirmed with absolute certainty without follow-up. These systems are all processed through the pipeline to remove any signal not from the EB, to phase-fold, and

to estimate geometric properties. By doing so, we can study the distribution of EBs across the field, provide false positive detection for planetary candidates, and identify interesting systems — including triple and higher order systems.

## 2.2 Data Detrending

The *Kepler* mission provides raw and corrected flux columns for each target. The corrected fluxes aim to remove as much of the instrumental trends (i.e., due to the response of the CCD or rolls of the spacecraft) while maintaining all of the astrophysical signal. The K2 mission only provides raw data products, so we utilize the extracted and de-correlated light curves provided by Vanderburg and Johnson (2014). However, this corrected signal can still come from a variety of astrophysical sources for the sample of EBs. In addition to the eclipsing signal itself, EBs often show variations in flux due to pulsations or spots on one or both stellar components. In order to estimate rough morphology and geometric parameters, we attempt to remove all signal except for the eclipsing signal at the determined ephemeris.

To accomplish this, we use a sigma-clipping technique to fit a series of polynomials to the upper-envelope of the raw data as provided by *Kepler* or Vanderburg and Johnson (2014). We then divide all fluxes by this “baseline” (see Figure 2.1), resulting in normalized and detrended light curves (Figure 2.2). We developed a custom graphical user interface, `kephem` (Prša et al., 2011a), to allow manual fine-tuning of the parameters of the polynomials: the breaks between each polynomial (often placed when the spacecraft rolled on its axes, resulting in a discontinuous break in the data), the order of each individual polynomial, and the upper and lower sigma limits for sigma clipping.

Although reasonable initial defaults were set for detrending all targets, most had to be manually adjusted to provide the best balance between removing extraneous signal without removing any of the EB signal.

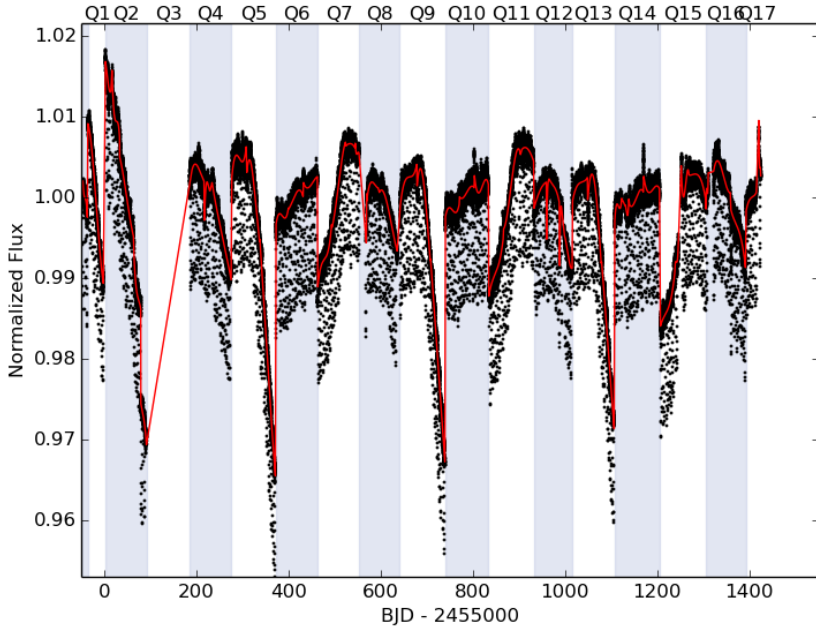


Figure 2.1 Raw Kepler data (black) and baseline (red) determined via sigma-clipping. The shaded regions represent the Kepler quarters — indicating when the spacecraft rolled resulting in discontinuities in the raw light curve.

### 2.3 Determining Ephemerides

Once the data are detrended, the period and  $\text{BJD}_0$  can be determined so that the light curve can be phase-folded. To accomplish this, all candidate EBs were phase-folded using a custom wrapper implementation of several periodogram methods from `vartools` (Hartman and Bakos, 2016) within `kephem`. By selecting the frequencies with the highest reported power, the user could quickly determine which peak corresponded to the correct period for the EB signal (i.e., to avoid harmonics and achieve one primary and one secondary eclipse, when applicable) and visually “scrub” over the periodogram to refine the value. By dragging on the phase light curve, the user could then set  $\text{BJD}_0$  so that the primary (i.e deeper) eclipse occurred at zero-phase.

Once ingested into the catalog, the pipeline automatically refined the ephemeris by determining the eclipse timing variations (see §4) by removing any linear trend by adjusting

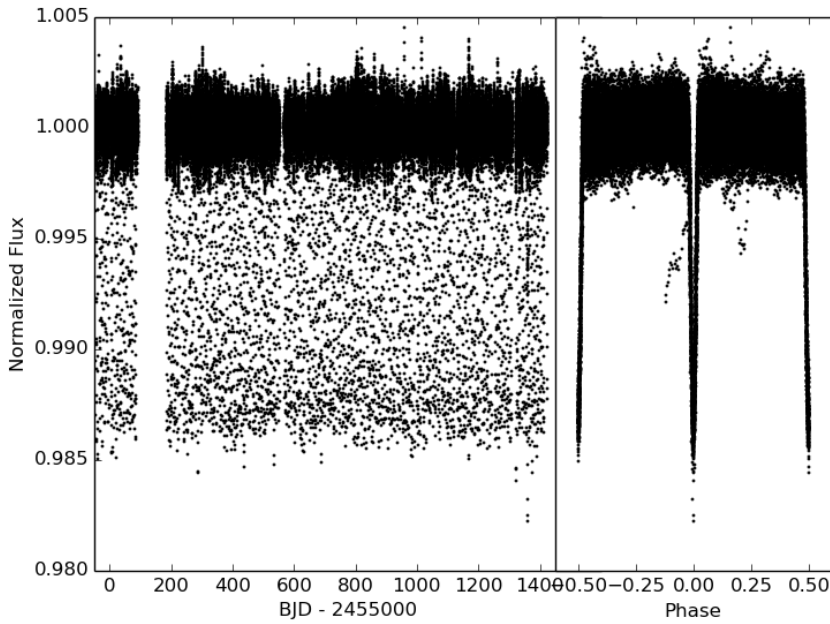


Figure 2.2 Detrended *Kepler* light curve in time-space (left) and phase-space (right) showing the eclipsing binary signal.

the ephemerides as necessary. We then provide error estimates on both the period and time of eclipse ( $\text{BJD}_0$ ) for every entry in the catalog. The period error is determined through an adaptation of the Period Error Calculator algorithm of Michell and Plavchan (2013). Using error propagation theory, the period error is calculated from the following parameters: timing uncertainty for a measured flux value, the total length of the time series, the period of the variable, and the maximum number of periods that can occur in the time series.

To revise a precise value and estimate the uncertainty on  $\text{BJD}_0$ , we use eclipse bisectors. These work by shifting the  $\text{BJD}_0$  until the left and right eclipse sides of the phased data overlap as much as possible. The overlap function is fitted by a gaussian, where the mean is the  $\text{BJD}_0$  estimate, and the width is the corresponding error. For case where this estimates an error larger than the measured width of the eclipse, generally due to extremely low signal to noise, we instead adopt the width of the eclipse as the error. Since there is not a well defined  $\text{BJD}_0$  for binary “heartbeat stars” or ellipsoidal variables — binary systems whose

variations are caused by the changing cross-section due to tidal distortions, but not actual eclipse signatures — we do not estimate or provide uncertainties for these objects.

### 2.3.1 Sources with Multiple Ephemerides

In some cases, a light curve can exhibit extra events that do not phase to the primary ephemeris. When there is only a single extraneous event, or the extraneous events cannot be phased themselves, we list each of those events in Table 2.1. These could be indicative of triple or higher-order systems with long periods (possibly even longer than the time baseline of the *Kepler* data set). In other cases, the extra events can be phased to a different ephemeris — these systems and their determined ephemerides are listed in Table 2.2.

For any of these systems, without confirmation from spectroscopy or eclipse timing variations (see §4), it is always possible that the observed signal is coming from an unrelated system bleeding light into the source aperture.

KIC	Event Depth (%)	Event Width (days)	Start Time (-240000)	End Time (240000)
6543674	0.96	2.	55023	55025
7222362	0.6	0.6	55280.9	55281.5
7222362	0.8	2	55307.5	55309.5
7222362	0.65	2	55975.5	55977.5
7668648	0.94	0.2	55501.1	55501.3
7668648	0.94	0.2	55905.5	55905.7
7668648	0.94	0.2	56104.4	56104.6
7668648	0.94	0.2	56303.7	56303.9
7670485	0.975	1.0	55663	55664

Table 2.1 Properties of extraneous eclipse/transit events in the *Kepler* sample.

## 2.4 Fitting a Deconvolved Analytic Function

In order to conveniently characterize the shape of the phase light curve, we fit each phased light curve with an analytic function. Due to the variety of “shapes” in EB light curves (from very sharp, V-shaped eclipses to sinusoidal ellipsoidal variables), we use a chain of four second-order polynomial functions. These polynomials are fitted to the data, with the “knots” that connect them also fitted simultaneously. This “polyfit” is then a piece-

KIC	Period (days)	Period Error (days)	BJD <sub>0</sub> (-2400000)	BJD <sub>0</sub> Error (days)
2856960	0.2585073	0.0000001	54964.658506	0.007310
2856960	204.256	0.002	54997.652563	0.369952
4150611	8.65309	0.00002	54961.005419	0.024746
4150611	1.522279	0.000002	54999.688801	0.003464
4150611	94.198	0.001	55029.333888	0.328165
5255552	32.4486	0.0002	54970.636491	0.116220
5897826	33.8042	0.0002	54967.628858	0.116761
5952403	0.905678	0.000001	54965.197892	0.014736
6665064	0.69837	0.00001	54964.697452	0.009707
6964043	5.36258	0.00002	55292.008176	0.308696
7289157	5.26581	0.00001	54969.976049	0.044130
7289157	242.713	0.002	54996.317389	0.055294
9007918	1.387207	0.000002	54954.746682	0.023254
11495766	8.34044	0.00002	55009.377729	0.0460252

Table 2.2 Systems exhibiting multiple ephemerides in the *Kepler* sample.

wise analytic function consisting of 15 parameters (4 polynomials each with 3 coefficients and 3 “knots”) that can be used as an approximate analytical representation of the entire phase-folded light curve (Prša et al., 2011a).

Due to *Kepler*’s long-cadence 30 minute exposure, the phased light curves suffer from a convolution effect. For short-period binaries this phase-dependent smoothing can have a significant impact on the overall shape of the polyfit representation, which would then propagate through the remaining steps of the pipeline. To mitigate this effect, we deconvolve the original polyfit that was determined from the phased long-cadence data. Since there are an infinite number of functions that would convolve to the original polyfit, we impose that the deconvolved representation must also be described by a polyfit. This does not necessarily guarantee a unique solution, but does add the constraint that the deconvolved curve resembles the signal from a binary. We start with the original polyfit and use a downhill simplex algorithm to adjust the various coefficients and knots, minimizing the residuals between the original polyfit and the convolved candidate-polyfit. This process results in another polyfit that, when convolved with a 30 minute boxcar, most closely resembles the original polyfit and, therefore, the phased long-cadence data (Fig. 2.3). This results in a better representation of the actual light curve of the binary which can then be used to estimate geometrical properties of the binary.

*Kepler*'s short-cadence photometry (1 min exposures) is short enough that the convolution effect is negligible. However, short cadence data are not available for all systems. Thus, to stay internally consistent, we use only long-cadence data to determine physical parameters and eclipse timing variations. Nevertheless, short-cadence data allow us to confirm the effect of convolution and test the performance of our deconvolution process. Comparing the deconvolved polyfit with the short-cadence data from the same EB shows that deconvolution is essential for more accurate approximations but can also result in a representation that does not make physical sense (see the right panel in 2.3).

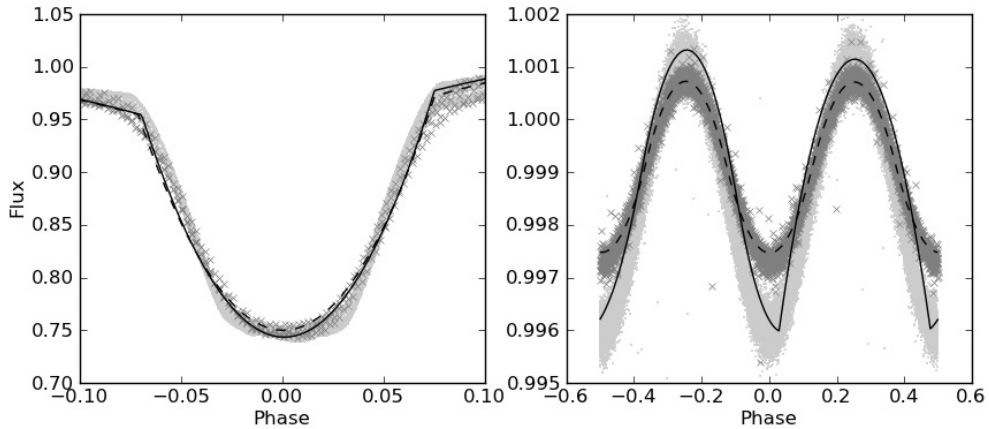


Figure 2.3 Original polyfit (dashed line) and deconvolved polyfit (solid line) plotted on top of short-cadence (light dots) and long-cadence (darker x) Q2 data of KIC 11560447 and 6947064. In both cases, the deconvolution was successful in finding a polyfit which when convolved best fits the long-cadence data, but this does not necessarily fit the short-cadence data or make physical sense.

## 2.5 Morphology Classification

In order to overcome the drawbacks of manual classification, we performed an automated classification of all identified EB light curves with a general dimensionality reduction numerical tool, Locally Linear Embedding (LLE; Roweis and Saul 2000). This method projects a high-dimensional data-set onto a much lower-dimensional manifold in a way that retains the local properties of the original data-set, so all light curves that are placed close

together in the original space are also nearby each other in the projected space. In our implementation, we downproject 1000 equidistant phase points (representing the phase-folded light curve) onto a 2-dimensional manifold. We then fit a spline to this manifold – assigning a single morphological classification parameter to each entry in the catalog representing the “detachedness” of the system (see Figure 2.4 and 2.5). Values of the parameter range from 0 to 0.1 for well-detached systems, values below 0.5 predominantly belong to detached systems and between 0.5 and 0.7 to semi-detached systems. Contact systems usually have values between 0.7 and 0.8, while even higher values up to 1.0 usually belong to ellipsoidal variables. This process is discussed in detail in Matijević et al. (2012).

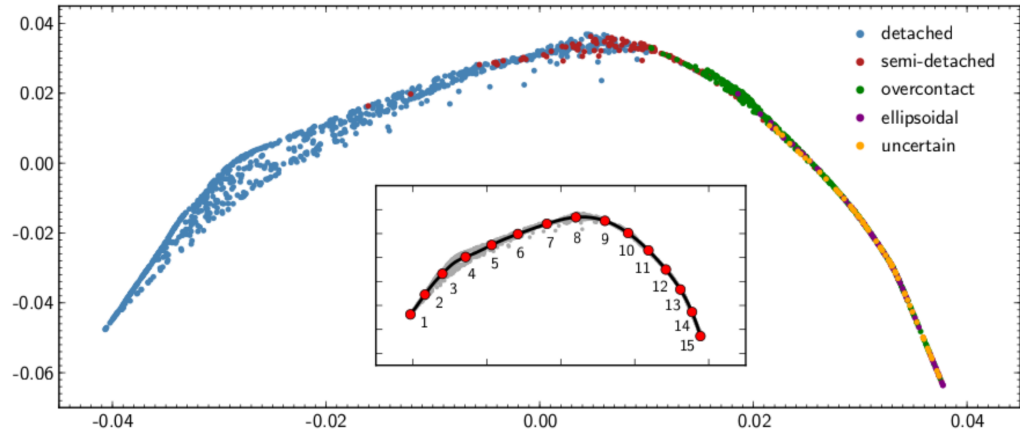


Figure 2.4 LLE projection for light curves. Note that the x and y axes represent arbitrary values and have no direct physical interpretation. The colors represent manual classifications through visual inspection , with the numbers representing a selection of objects along the curve that are represented in Figure 2.5. This Figure appears in Matijević et al. (2012) as Figure 2.

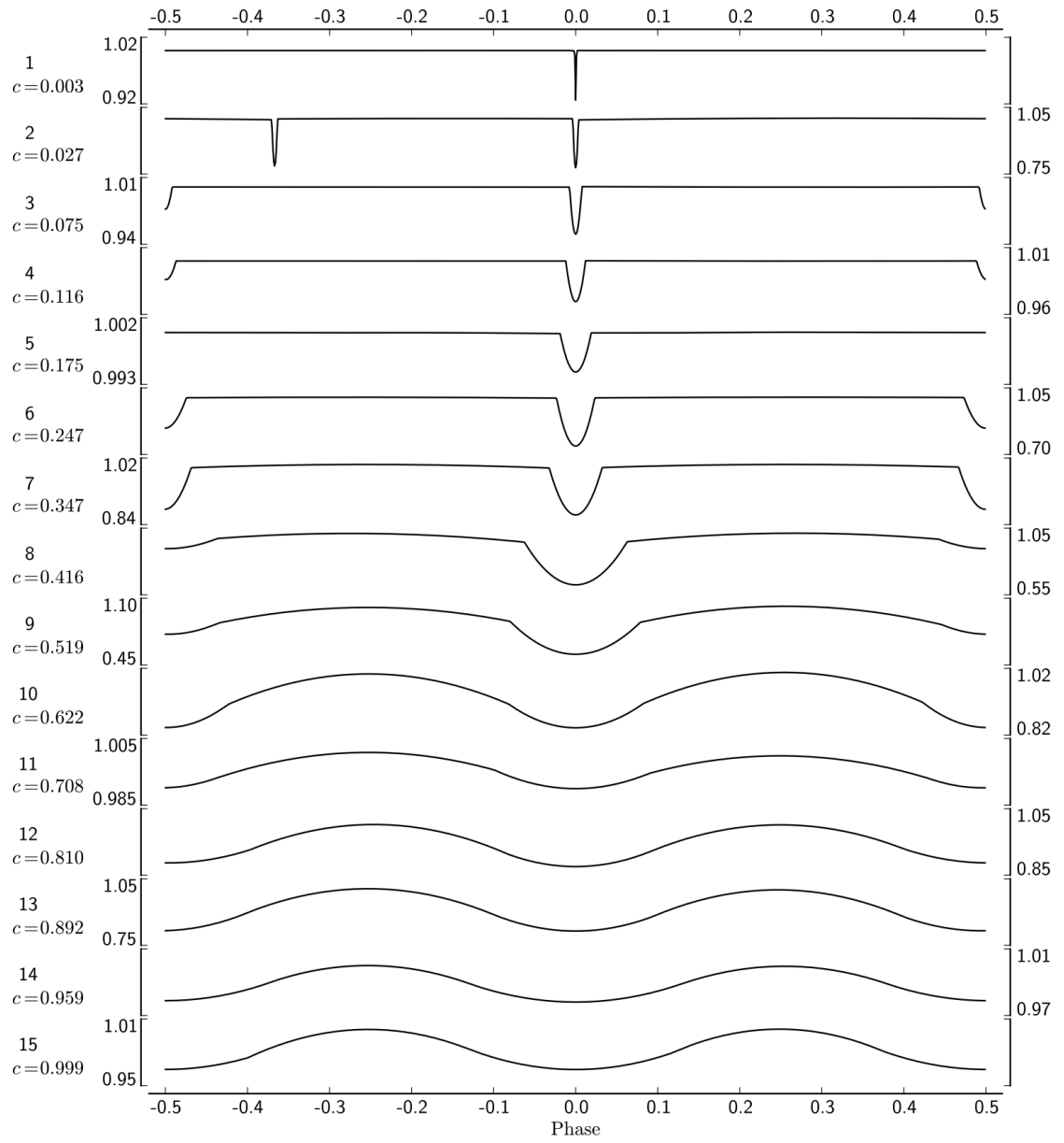


Figure 2.5 Polyfit representations of light curves across the range of the morphology classification. These examples are numbered according to their positions noted in Figure 2.4. This Figure appears in Matijević et al. (2012) as Figure 3.

## 2.6 Spectroscopic Follow-Up

Modeling EBs with only photometric data can only constrain the relative sizes of the stars and can not robustly determine the masses or mass-ratio. In combination with radial velocity obtained from double-lined spectral observations, however, these degeneracies can be broken, and the absolute values for masses and radii of both stars can be determined. For these reasons, it makes sense to obtain spectra observations for *Kepler* EB targets, whenever possible.

We successfully proposed for 30 nights at the Kitt Peak National Observatory’s 4-m Mayall telescope to acquire high resolution ( $R \geq 20,000$ ), moderate signal-to-noise ( $S/N \geq 15$ ), spectra using the echelle spectrograph. As it is impractical to observe all EBs in the catalog, we prioritized targets that fell into the following categories:

- **Well-detached EBs in near-circular orbits.** Since the stars in these systems are well-separated and exhibit little disotrtion, they can safely be assumed to be coeval and have evolved independently. These are therefore prime sources for calibrating the  $M-L-R-T$  (mass-luminosity-radius-temperature) relationships across the main sequence.
- **Low-mass main sequence EBs.** Carefully modelling these systems allows us to test the discrepancy between the theoretical and observational mass-radius relations at the bottom of the main-sequence, namely that the observed radii of low-mass stars are up to 15% larger than predicted by structure models.
- **EBs featuring total eclipses.** EBs exhibiting total eclipses (i.e., a flat bottomed eclipse caused by a significant difference in radius between the two components) allow us to determine the inclination and the radii to an even higher accuracy, typically a fraction of a percent. Coupled with RVs, we can obtain the absolute scale of the system and parameters of those systems with unprecedented accuracy.

- **Candidate triple and multiple systems.** Systems that are determined as potential triple or higher order systems due to their ETVs (see §4) could show triple lined spectra or an RV signature, confirming the number of stars in the system, and ultimately allowing to model all components in the system to great precision (see §6).

During the observing runs, we attempted to maximize phase-sampling across the prioritized targets. To do so, we scheduled observations for each target such that radial velocities were obtained at quadrature (quarter phases) according to the ephemeris in the catalog. This would result in approximately four radial velocity measurements per EB and would adequately characterize the amplitude and shape (i.e., eccentricity) of the signal.

We acquired and reduced multi-epoch spectra for 611 systems within this program. The spectra are available for download from the catalog website at <http://keplerEBs.villanova.edu>.

## 2.7 Distributions

The distribution of area-corrected EB occurrence rate as a function of galactic latitude is shown in Figure 2.6, showing a non-uniform distribution with an increased rate of EB occurrence at low latitudes. This is likely due to the fact that lower latitudes (thin disk) contain younger stars on average than higher latitudes (thick disk and halo). This younger population is therefore larger on average – due to more giants in the magnitude-limited sample (Prša et al., 2015). Due to the larger radii, any given binary has a larger geometrical probability of eclipse (i.e., a wider range of inclinations will still result in a grazing eclipse).

Figure 2.7 shows the distribution of orbital periods across the catalog. With the primary *Kepler* mission having ended after  $\sim$ 4 years, the longest orbital periods in the catalog are at  $\sim$ 1000 days. Catalog completeness at those periods is challenged by our ability to detect every single eclipse event, which can be made difficult by the small eclipse amplitudes, data gaps and other intrinsic and extrinsic contributions to background and noise. Adding to this is the increasingly low probability of eclipses at the larger orbital separations that accom-

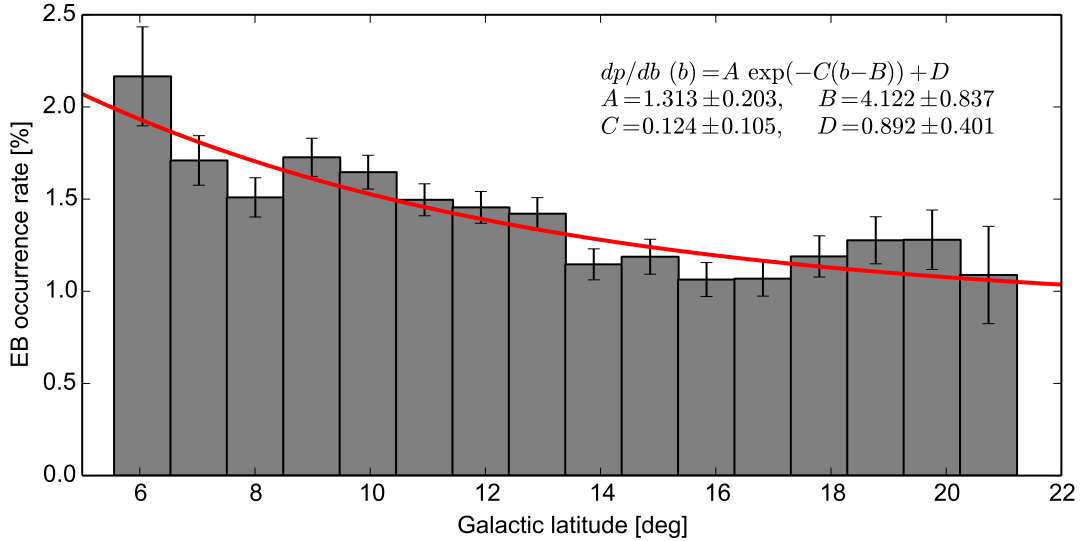


Figure 2.6 EB occurrence rate ( $dp/db$ ) as a function of galactic latitude ( $b$ ). Each latitude bin is area-corrected to give true occurrence rates. Uncertainties are estimated as  $\sqrt{N_j}/N_{\text{tot},j}$ , where  $N_j$  is the number of detected EBs and  $N_{\text{tot},j}$  is the total number of targets observed by *Kepler* in the  $j$ -th bin. The solid line represents the exponential fit to the data, with parameters annotated in the Figure. The parameters  $A$  and  $D$  are occurrence rates,  $C$  is the thin-to-thick disk transition value, and  $B$  is degrees of galactic latitude. The results of this toy model indicate that the occurrence rate span of EBs ranges between 0.9% and 2.2%.

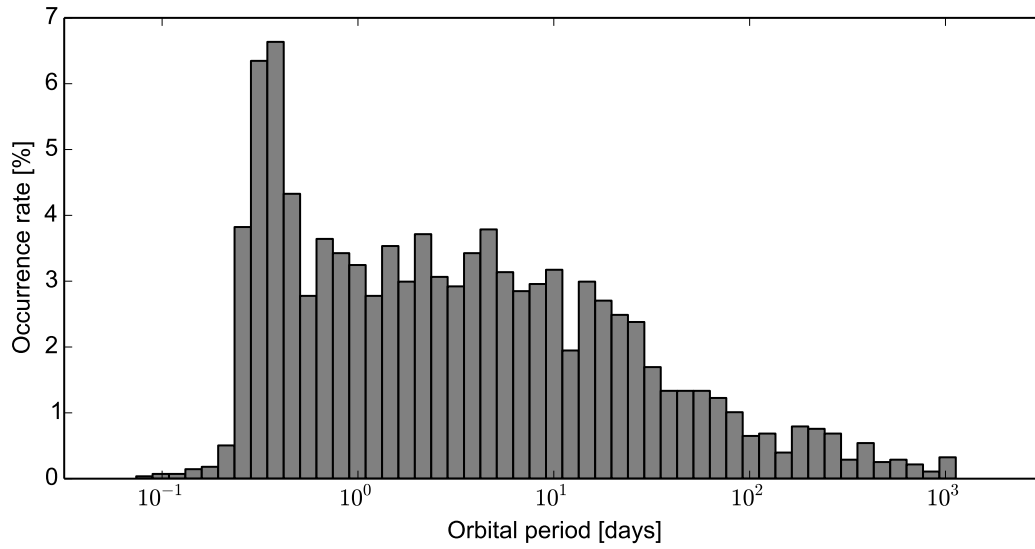


Figure 2.7 Distribution of orbital periods of all *Kepler* EBs.

pany longer periods, and of course the increasing probability of entirely missed eclipses for orbital periods longer than the observing window. On the other hand, completeness should be  $\sim 100\%$  for short period EBs ( $P \sim 1$  day) because of the high geometrical probability of eclipses and because even non-eclipsing systems manifest as ellipsoidal variables. Two features are particularly interesting: the excess of short period binaries ( $P \sim 0.3$  day) and the gradual drop-off of longer period binaries.

The short-period excess is a well-known feature of eclipsing binaries: at short periods, proximity effects become pronounced, most notably ellipsoidal variations, which enable us to detect binary stars even in the absence of eclipses. This also drives the overall probability of detection sharply upwards at shorter periods. However, the period plateau at  $\sim 2\text{-}3$  days cannot be accounted with detection biases or binary formation theory. This is instead often explained by forming a binary at a wider separation (and longer period) and tightening the binary over time to the  $\sim 2\text{-}3$  day orbit we observe today. Many of these mechanisms, including Kozai-Lidov Cycles and Tidal Friction (KCTF; Fabrycky and Tremaine 2007) require the presence of a third body. In the case of KCTF, interaction between the inner binary and companion on a wide eccentric orbit, result in an exchange in angular momentum between the inner binary eccentricity and outer orbit inclination. When the components of the inner binary are sufficiently close, tidal friction dissipates energy and tightens the pair. The high occurrence rate of stellar triples through ETVs (Conroy et al., 2014b; Gies et al., 2012; Rappaport et al., 2013) gives further credibility to this model (see §4).

The gradual drop-off at the long period end is due to two main contributions. The dominant contribution is the geometrical probability of eclipses. The second contribution is due to *Kepler*'s duty cycle. The satellite observed a single patch of the sky, but observations were interrupted by regular quarterly rolls and data downlink, and by unexpected events that put the telescope into safe mode. As a result, the actual duty cycle of observations was  $\sim 92\%$ . These effects and their corresponding corrections are discussed in detail in Kirk et al. (2016).

By identifying and cataloging these systems, we can easily make use of the *Kepler* data in conjunction with follow-up data and archival data (both from space and the ground) to robustly model these systems as well as to search for triple and multiple systems. However, existing codes to model these systems are no longer adequate to reach the full potential in precision and accuracy theoretically available due to the ultra-precise photometry delivered by *Kepler*.

## Chapter 3

### Considerations for Modeling Eclipsing Binaries in the *Kepler* Era

*This chapter includes excerpts and figures adapted from Prša et al. (2016), used with permission from The Astrophysical Journal Supplement Series.*

In addition to *Kepler* (Borucki et al., 2010), there is a wide range of recent missions surveying the sky and collecting high-precision photometric data. These missions cover a vast population of EBs (Prša et al. (2011b) estimates a yield of  $\sim 7$  million from *LSST* alone) to an unprecedented precision (down to  $\sim 20$  ppm for *Kepler*).

There are several publicly available codes that model EB systems and allow for fitting an underlying physical model to observational data. For example, the Wilson-Devinney code (Wilson and Devinney, 1971; Wilson, 1979, 2008; Wilson and Van Hamme, 2014, hereafter WD), and the original version of PHOEBE (Prša and Zwitter, 2005, hereafter PHOEBE Legacy) which extended WD and included a scripting language and graphical user interface, have widely been used in the literature. However, the underlying approximations and assumptions used in these codes begin to breakdown when attempting to achieve the precision necessary to model modern observational data from missions such as *Kepler*.

Fixing these limitations required extensive changes to the underlying framework, and so, as part of the PHOEBE development team, I helped redesign and rewrite the entire PHOEBE code from scratch with increased precision and flexibility to add new physics, system hierarchies, and physics into the model. We have released a new version of the open-source modeling code PHOEBE 2, under the General Public License, written in C (backend) and python (frontend). PHOEBE 2 is available for download from <http://phoebe-project.org> and <http://github.com/phoebe-project>, along with extensive documentation and tutorials.

PHOEBE 2, like many other numerical EB models, computes synthetic models of observables (i.e., light curves and radial velocity curves) by creating a discretized surface of the stars and determining which surface elements are visible at any given time. Below is a brief summary of the general logic and order of operations as implemented within PHOEBE 2:

1. Dynamics (§3.1): the positions of each star are determined for each requested time for the given Keplerian orbital elements.
2. Discretization (§3.2): a triangulated mesh is created for each star in the system for the given Roche equipotential, as defined at  $t_0$ .
3. Place in orbit (§3.3): the meshes are placed in orbit at each requested time, adapting to changes to the gravitational equipotential (i.e., for an eccentric orbit where the distance between the stars changes in time).
4. Local quantities (§3.4): at each time, each surface element must compute its local quantities (effective temperature, surface gravity, intensity in a given passband, etc).
5. Eclipse detection (§3.5): the portion of each surface element visible to the observer must be determined.
6. Integration: local quantities need to be integrated over the visible portion of the star to obtain the observed quantity (i.e., flux or radial velocity).

Here we discuss the specific considerations required for high-precision observations. For a full overview of PHOEBE 2, see Prša et al. (2016).

### 3.1 Dynamics and Light Time Effects

In the case of binaries (see §6.2 for considerations in the case of triple and higher-order systems), PHOEBE 2 computes the positions of each object at a given time via Keplerian

orbits (Goldstein, 1980). The orbits depend on the semi-major axis  $a$ , orbital period  $P_0$ , mass ratio  $q$ , eccentricity  $e$ , and systemic velocity  $v_\gamma$ ; their orientation is given by an inclination  $i$ , argument of periastron  $\omega$ , and longitude of the ascending node  $\Omega$ . While this formalism describes dynamical positions of the bodies in their orbits, it does not describe the position where the observer *sees* the bodies due to the finite speed of light.

To address this, PHOEBE iteratively determines the point in each object’s orbit such that a photon leaving that star, traveling towards the observer, will cross the origin of the coordinate system (defined such that the barycenter of the system is at the origin at time  $t_0$ ) at the time of the observation. By doing so, any bodies closer to the observer, with respect to the barycenter, appear at an advanced point in the orbit, while bodies farther away appear at an earlier point. This effect is often called the “Rømer delay”, with its influence on eclipse times discussed in further detail in §5.6.

By defining the reference time with respect to the origin, PHOEBE 2 allows the barycenter to move at a constant velocity. Any radial (along the line-of-sight) barycentric velocity will result in a measured period (i.e., between successive primary eclipses) different than the Keplerian orbital period. Any barycentric velocity on the plane-of-sky will result in an asymmetry in the Rømer corrections, as discussed in detail in §5.9.

### 3.2 Surface Discretization

PHOEBE 2 determines the shape of a distorted star using one of two supported types of surface potentials: the Roche model and the rotating single star model. The generalized Roche lobe (Wilson, 1979) potential,  $\Omega$ , is defined by:

$$\Omega_{\text{Roche}}(\mathbf{r}; q, F, \delta) = \frac{1}{\|\mathbf{r}\|} + q \left( \frac{1}{\sqrt{(x-\delta)^2 + y^2 + z^2}} - \frac{x}{\delta^2} \right) + \frac{1}{2}(1+q)F^2(x^2 + y^2), \quad (3.1)$$

expressed in Cartesian coordinates  $x$ ,  $y$ , and  $z$ , with the radius vector denoted by  $\mathbf{r} = (x, y, z)/a$ ;  $q \equiv M_2/M_1$  is the mass ratio,  $F \equiv P_{\text{rot}}/P_{\text{orb}}$  is the synchronicity parameter, and

$\delta \equiv d/a$  is the instantaneous separation between the stars relative to the semi-major axis  $a$ .

The potential of an isolated star rotating around the  $z$ -axis is given by:

$$\Omega_{\text{rot}}(\mathbf{r}; \omega) = \frac{1}{\|\mathbf{r}\|} + \frac{1}{2}\omega^2(x^2 + y^2), \quad (3.2)$$

where  $\omega$  is the angular velocity of rotation.

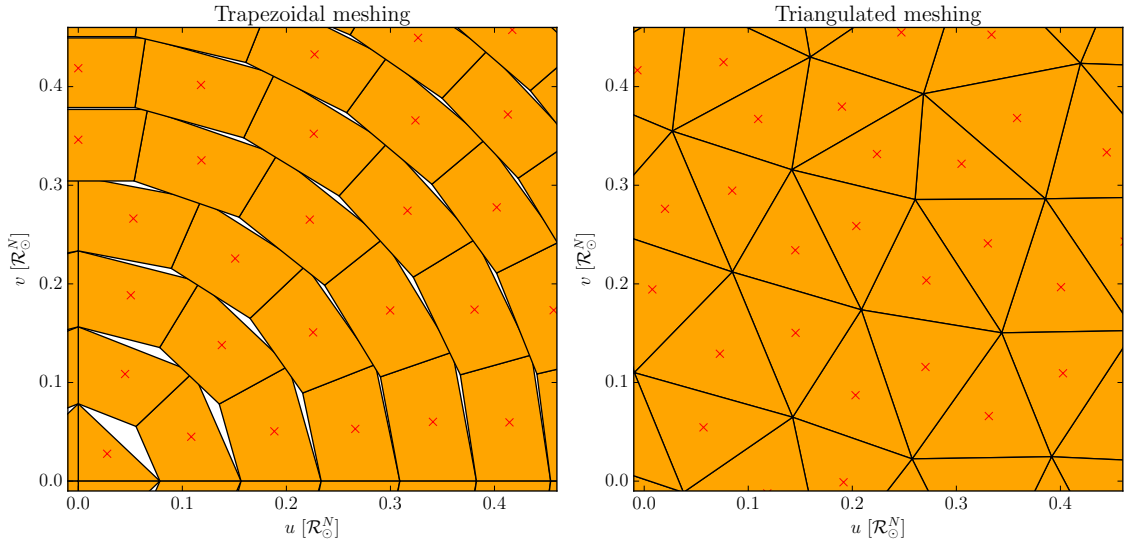


Figure 3.1 Mesh comparison between the trapezoidal discretization using trapezoidal elements (left) and triangulation (right). The crosses denote surface element centers. Both parts correspond to the same region on the star. The issues with trapezoidal discretization are disconnected, overlapping meshes with holes, and obvious “seams” across the surface. All these cause systematic effects in computed fluxes.

This distorted shape then dictates a wide range of effects: surface brightness variation due to gravity darkening, limb darkening and reflection, ellipsoidal variations due to the changing cross-section size that faces the observer, etc. Traditionally, particularly in PHOEBE Legacy and WD, these surfaces were discretized uniformly along co-latitude and longitude into planar, trapezoidal elements for which local conditions were assumed to be uniform. Unfortunately, this results in *disconnected* and *self-overlapping* surface elements that do not cover the surface completely. The left panel in Figure 3.1 displays a part of the star near a pole, a region where these problems are particularly exacerbated.

This method also causes significant issues for contact binary systems. Here the trapezoidal method diverges near the neck of these contact envelopes, requiring discretizing each “half” of the contact system separately and joining them together (Wilson, 1979). Unfortunately, this often leads to gaps in the mesh near the neck (see the left panel in Figure 3.2), particularly for systems with a small mass ratio and large fillout factor.

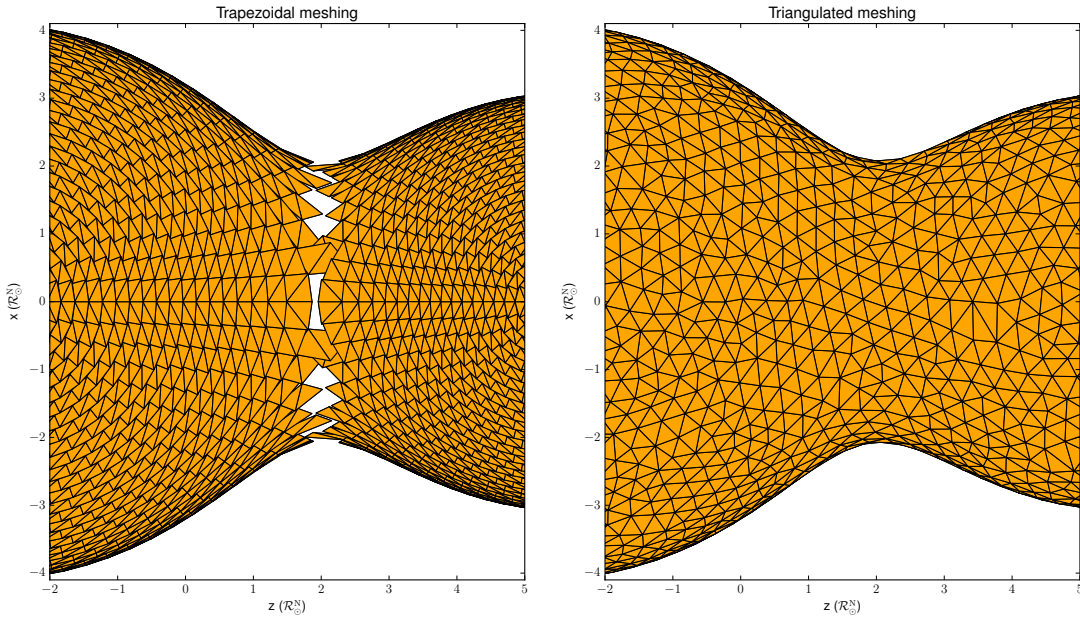


Figure 3.2 Comparison of the neck region coverage in a trapezoidal (left) and triangulated mesh (right) of a contact system with mass ratio  $q = 0.5$  and fillout factor  $FF = 0.9$ . The trapezoidal mesh is represented by its current implementation in PHOEBE 2, in which each trapezoid is split into two triangles for plotting, but retains its center, where all local quantities are computed.

To overcome these problems, PHOEBE 2 replaces trapezoidal surface elements with triangles. The triangulation of implicit surfaces is a long standing problem in computational physics. Hartmann (1998) presents a *marching method*: an algorithm that can discretize any implicit surface into a set of near-equilateral triangles, so that every element on the surface has approximately the same area, irrespective of the position or the amount of surface distortion. The right panel in Figure 3.1 demonstrates this: the polar region of the star has no inherent symmetry that would impose “seams” across the surface, or surface elements of notably different sizes. In effect, any systematics that may arise from surface discretization will be minimized. A mesh generated this way is computationally tractable and alleviates

the problems with holes or overlaps between trapezoidal elements. Figure 3.2 shows the improvements in the contact case, where the triangulated mesh successfully covers the entire mesh region in one, continuous, mesh.

### 3.2.1 Surface Offsetting

The classical trapezoidal meshes were constructed such that the center of the elements were on the surface defined by the equipotential. By triangulating, we instead place the vertices of the triangles on the surface. In the trapezoidal case, this results in an overestimate of the surface area and volume of the star, whereas the triangulation case results in an underestimate. To correct for this, we offset all vertices from the surface such that (1) the total surface area of the mesh is exactly equal to the analytical surface area of the equipotential surface, and (2) each triangular element is offset according to the local curvature. Figure 3.3 shows the benefits of this approach - comparing the Fourier fit to the horizon used within WD to the numerical horizon caused by the offset triangular mesh in PHOEBE 2.

By using a triangulated mesh that maintains the correct surface area and volume, PHOEBE 2 avoids many of the precision issues associated with trapezoidal meshes. As an added benefit, the marching scheme is flexible enough to handle any implicit surface — making the future implementation of spherical planets or rings possible within the existing framework.

## 3.3 Volume Conservation in Eccentric Orbits

For eccentric orbits, the Roche potential (Equation 3.1) changes in time as the instantaneous separation ( $\delta$ ) between the two stars changes throughout the orbit. We must account for the affect of this change on the distortion of the stellar surface. If we were to keep the equipotential fixed throughout the orbit, the stars would change in volume throughout, resulting in generated heat during compression that would be irradiated away and not recovered during expansion. This loss of energy would likely result in rapid circularization

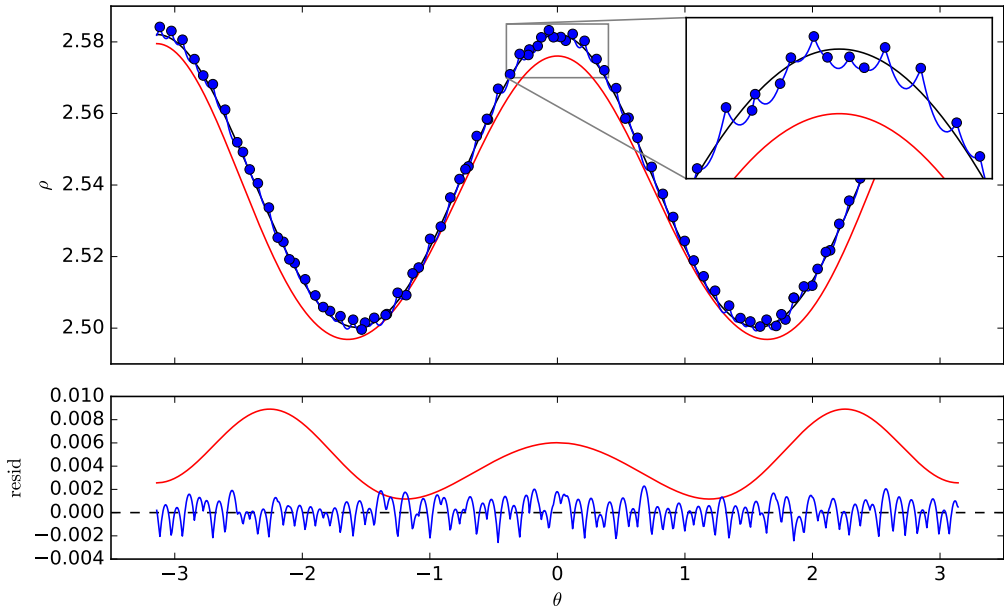


Figure 3.3 Horizon of a Roche star as determined by PHOEBE 2 and WD in polar coordinates. The black curve represents the analytic horizon, the red curve represents the Fourier fit to the horizon used in WD, the blue points represent surface elements of the offset PHOEBE 2 mesh that are on the horizon, and the blue line represents the polygonal shadow that these points span. The lower panel shows the residuals between the Fourier-based (red) and offset triangulation-based (blue) horizons with respect to the analytical horizon.

leading to a very small expected number of eccentric short period binaries.

Instead, in PHOEBE Legacy and WD, the simplest assumption has been made — that the volume of each star is conserved throughout its orbit. Although this assumption seems reasonable, it has never been directly tested. Within PHOEBE 2, we compute the analytical volume of the star as defined by the given equipotential at  $t_0$  and compute the instantaneous equipotential that results in a surface of the same volume at any given time.

We also implemented a framework within PHOEBE 2 that allows for the parameterization of a small deviation from volume conservation. Highly eccentric ellipsoidal variables (also known as *heartbeat* stars; Thompson et al. 2012) can include red giants that are separated by only a few stellar radii at periastron. This results in significant tidal forces and extreme changes in stellar distortion throughout the orbit. A total of 28 giants in heartbeat

stars have been reported to date (Nicholls and Wood, 2012; Gaulme et al., 2013, 2014; Beck et al., 2014; Richardson et al., 2016); of these, there are 9 for which the authors developed a full model (Nicholls and Wood, 2012; Beck et al., 2014; Richardson et al., 2016), all of them under the constant volume assumption. These are prime candidates for testing the assumption of volume conservation by allowing for a small deviation in the physical model and is the topic of a future paper by Hambleton et al.

### 3.4 Sampling Local Quantities

As expected from any discretization scheme, the resulting precision of the synthetic model correlates directly with the number of surface elements. The most obvious way to increase the precision would then be to increase the number of surface elements. Unfortunately, meshing and storing all the surface elements can quickly become computationally expensive, and the larger the number of surface elements, the more computational noise begins to contribute to the limits of the final precision. Even worse, when using the trapezoidal scheme, the gaps and overlaps mentioned above can accumulate and cause a limit to the achievable precision. As these models need to be computed numerous times in order to fit observations, it is important to optimize a scheme in which the necessary precision can be reached while minimizing computation cost and noise. PHOEBE 2 attempts to accomplish this goal by “sampling” the local quantities at the vertices of the triangles — essentially mimicking a grid with three times the number of elements as the mesh itself.

As discussed in §3.2.1, PHOEBE 2 initially places all vertices on the equipotential surface and then offsets them to obtain the correct surface area and volume. However, we also maintain a copy of the positions of the vertices on the surface prior to offsetting and use these positions to assign local quantities (i.e., surface gravities, effective temperatures, passband intensities, etc) to each vertex. This results in two meshes stored in memory — the first in which the vertices are positioned directly on the surface of the star is used to compute the local quantities, and the second in which the resulting surface area and

volume match the expected value is used for geometrical quantities (i.e., surface area of each element) and eclipse detection (see §3.5). The local physical quantity assigned to each triangle (in the case of a fully visible triangle, partially visible triangles are discussed in §3.5) is then the arithmetic mean of the values at each of the vertices corresponding to that triangle. This is a linear approximation; we assume that the variation of each physical quantity across each discretized surface element is linear. It is still therefore necessary to sample the surface with a sufficiently fine grid so that this approximation is accurate.

### 3.5 Eclipse Detection

In order to determine the total flux received from the system, intensities must be integrated over the visible surface elements at any given time. PHOEBE determines the visibility of each triangle element through horizon and eclipse computation, which is performed once the meshes of all bodies are placed in orbit and their physical quantities are computed for each vertex.

Eclipse computation is done on the offset triangulated mesh. Figure 3.3 depicts the projected shadow of a marching mesh compared to the theoretical horizon and demonstrates that the determined horizon of each star agrees well with the theoretical expectation. In contrast, the Fourier-based eclipse detection implemented in PHOEBE 1 (and WD) determines the horizon of each star by fitting a Fourier series to the coordinates of surface elements closest to the horizon (Wilson, 1993). In consequence, this approach will always underestimate the size of the shadow with respect to the analytic horizon. This underestimation converges with an increase in the number of surface elements, but very slowly. Due to the offsetting of surface elements to obtain the correct numerical surface area, PHOEBE 2 does not underestimate the horizon even for a very coarse mesh and increasing the number of elements in PHOEBE 2 only makes the horizon smoother.

PHOEBE 2 determines the ratio of each element that is visible to the observer. First, all elements in which the surface normal is pointed away from the observer, are excluded with

a ratio of exactly 0. Next, we utilize Painter’s algorithm (Hughes et al., 2013), whereby the remaining triangles are ordered with respect to distance from the observer and projected onto the plane-of-sky. We then calculate the visible part of the projected triangles using the clipping algorithm adapted from the Clipper 2D polygon algebra library<sup>1</sup>, which is based on Vatti’s method (Vatti, 1992). From the visible parts of the projected triangles we deduce the ratio of each triangle that is visible as well as the revised centroid of the visible portion by adapting the implementation by Paul Bourke<sup>2</sup>.

This revised centroid is then used to compute a *weighted* arithmetic mean of any observable local quantity stored in the vertices, under the assumption that these properties vary linearly across the local surface element (see Figure 3.4). The observable surface area is then determined based on the determined ratio of the element that is visible. By computing the observable quantities in this way, we effectively allow for an accurate approximation of ingress/egress without the requirement of a fine mesh that is more computationally expensive.

---

<sup>1</sup><http://www.angusj.com/delphi/clipper.php>

<sup>2</sup><http://paulbourke.net/geometry/polygonmesh/>

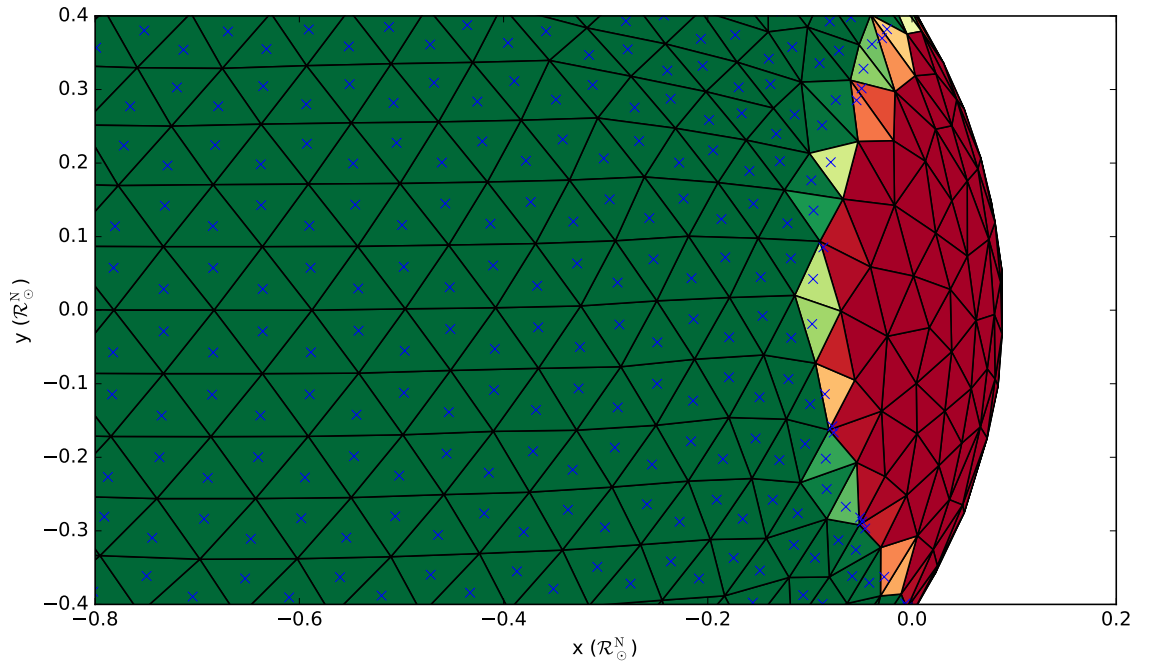


**Figure 3.4** A segment of a partially-eclipsed mesh. The colors of each triangle represent the ratio of the triangle area that is currently visible, with green being fully visible and red being fully eclipsed. The blue crosses represent the centroid of the visible portion of the triangle. For fully visible (green) triangles, the centroids appear at geometric centers of the triangles whereas the partially visible (orange and yellow) triangles show the centroid moving away from the eclipsed region. These centroids and ratios are used to integrate over the visible surface of the star(s).

By completely redesigning and rewriting this modeling code from scratch, PHOEBE 2 is now capable of reaching the precision of modern observational surveys. In modeling these systems, it is now possible to push the limits of the resulting model parameter uncertainties for benchmark EB systems.

However, these updates come with computation cost. The computational infrastructure of PHOEBE 2 is implemented in the low-level C language for speed, and the interface part is written in the high-level python language that is inherently slow. A number of causal computations are still linked through python, which causes slowdown of the execution time. However, the dominant source of slowdown is increased model fidelity. Shortcuts taken before are no longer in effect and, even though effects can be turned off by the user, the impact on the overall runtime is significant. That is why the preferred mode of deployment of PHOEBE 2 is on HPC clusters.

PHOEBE 2 is released as an open-source project under the GNU General Public License v3.0 and available at <http://github.com/phoebe-project/phoebe2>. Additional feature releases are planned and will be accompanied by minor releases.

## Chapter 4

### Identification of Triple and Multiple Systems via Eclipse Timing Variations

*This chapter includes excerpts and figures adapted from Conroy et al. (2014b), used with permission from The Astronomical Journal.*

Kirk et al. (2016) determined the ephemerides for the entire *Kepler* Eclipsing Binary Catalog (also see discussion in §2). If there are no external effects, a linear ephemeris will correctly predict all eclipse times of an EB. By measuring the exact time of each eclipse for a particular binary and comparing it to the calculated time from the linear ephemeris, we can create an ETV curve ('eclipse timing variations'; sometimes also referred to as an O-C diagram). Any trend in these timing residuals may be the result of one or more physical effects occurring in the system.

Rappaport et al. (2013) previously published a list of 39 candidate third-body *Kepler* systems using eclipse times and Gies et al. (2012) published a preliminary study on timing variations in 41 *Kepler* Eclipsing Binaries. Orosz (2015) provided eclipse times for detached binaries, while Conroy et al. (2014b) (discussed here) provided eclipse times for close binaries. Together, these two papers comprehensively cover all 2605 binaries in the *Kepler* EB catalog.

*Kepler*'s essentially uninterrupted observing over a long time baseline presents the opportunity to precisely time the eclipses and detect any underlying signals due to third bodies, apsidal motion, dynamical interaction, etc. Due to the large number of EBs in the entire catalog, it is necessary to create an automated method for timing eclipses across the catalog. Short period and contact systems present a particular challenge due to spot activity and data convolution, due to a relatively long integration time.

#### 4.1 Measuring Eclipse Times

Orosz (2015) provides eclipse times for binaries with flat out-of-eclipse regions, covering most of the detached binaries with periods greater than 1 day. There we locally detrend each eclipse and use a piecewise Hermite spline template to determine the time of mid-eclipse. This technique performs well on the set of detached systems but is not optimal for contact systems, systems with strong reflection effects or tidal distortion, or short-period binaries with only a few points in each eclipse due to *Kepler*'s 30 minute cadence. For this reason, we divide the catalog based on the morphology parameter as described in Matijević et al. (2012). This parameter is a value between 0 and 1 which describes the “detachedness” of an eclipsing binary, with 0 being completely detached and 1 being contact or ellipsoidal. Orosz (2015) report timings for binaries with a morphology parameter less than 0.5. The method discussed here addresses and determines eclipse times for the remainder of the *Kepler* Eclipsing Binary Catalog.

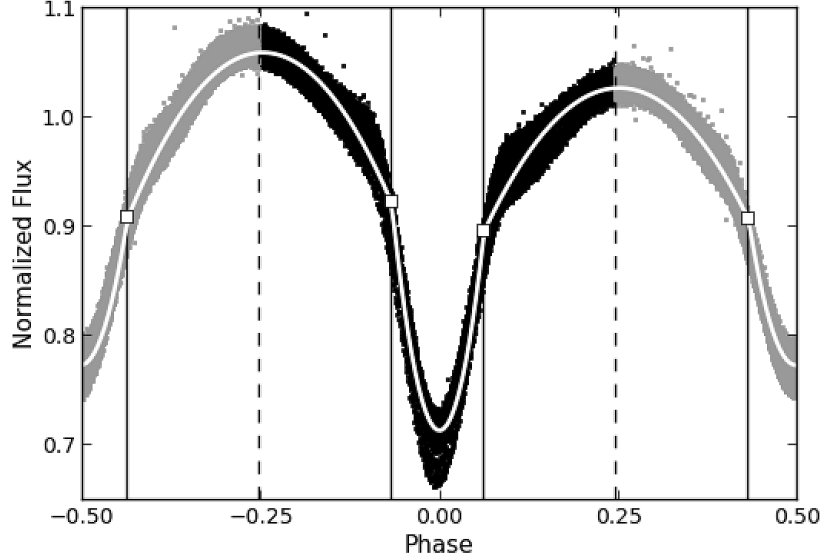


Figure 4.1 Typical polyfit and eclipse bounds for a semi-detached binary. The polyfit knots are indicated with the squares and solid vertical lines, with the polyfit drawn in white over the data. Data considered as part of the primary eclipse are shown in black while those belonging to the secondary eclipse are shown in gray. The eclipse bounds are set at the arithmetic bisector of the adjacent knots and are shown with dashed vertical lines.

We fit a polynomial chain to the phased, detrended, light curve data as described in §2.4 and Prša et al. (2008). This analytic function is a chain of four polynomials that is continuous, but not necessarily differentiable, at knots which were optimized to find the best overall solution. This function does not represent a physical model, but rather analytically describes the mean phased shape of the binary light curve, an example of which can be seen in Figure 4.1.

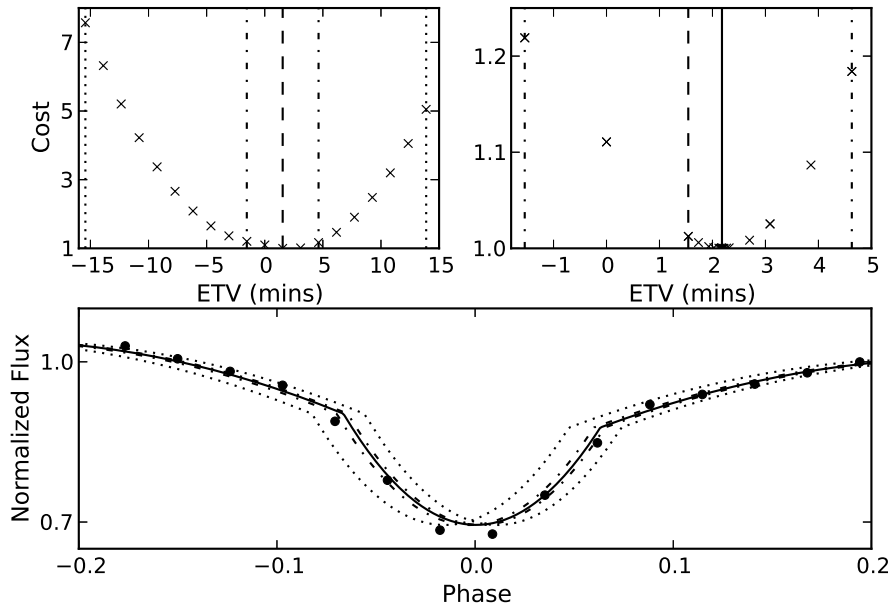


Figure 4.2 Reduced cost function ( $\chi^2$ ) values, shown as x's, are computed heuristically (top-left) for 20 evenly spaced phase-shifts within 0.05 phase, shown by the dotted lines in all panels. The best fit of these is shown with the dashed line in the top-left panel. A bisection approach (top-right) is then applied in the area surrounding this estimate, as shown by the dot-dashed lines. This results in a final minimum at the phase shift denoted by the solid line. The bottom plot shows the data for a single eclipse along with the polyfits for the respective shifts noted above.

We then take this analytical representation and, using a combination of heuristic and bisection approaches, determine the horizontal shift required to minimize the  $\chi^2$  (cost function) for each individual eclipse as shown in Figure 4.2. In order to minimize the effect due to spots or imperfect detrending, a vertical shift is first determined using linear least squares for each eclipse and is applied before computing cost functions for horizontal shifts. The cost function is initially sampled at 20 evenly-spaced phase shifts between -0.05 and 0.05

phase. The minimum of this sampling is then used as the center of the bisection algorithm to quickly find the local minimum of the cost function. The resulting  $\chi^2$  values are unusually large because the errors on the *Kepler* data are only formal and do not include any absolute calibration (Jenkins et al., 2010). Therefore, for each eclipse, we normalize the entire cost function such that the minimum cost is set to  $N - p - 1$ , where  $N$  is the number of data points used for that eclipse and  $p$  is the number of degrees of freedom, which we take to be 1. This reduced cost function is then used to compute 1-sigma errors on each timing to correspond to the  $\Delta\chi^2 = 1$  contour.

For the shortest binaries in the catalog, however, the long-cadence data result in significant phase-smearing and limits our method to a very minimal number of points per cycle to determine a fit. If there were to be a third-body, the signal would likely be buried in the noise induced by these factors. For this reason, we include as many data points as possible in each eclipse timing. Each data point is considered to belong to an eclipse if its phase as determined by the initial linear ephemeris is within bounds. We initially set these bounds to be the mid-point between polyfit knots in the out-of-eclipse region as shown in Figure 4.1. To improve results for particular objects being studied individually, changing these bounds to use the knots (instead of the mid-points) can sometimes lower the systematics in the signal. For any given eclipse, if the region between these bounds is not fully sampled or does not have at least three data points, then timings are not computed for that eclipse. Eclipse timings are then compared to the values expected from the linear ephemeris as reported by Kirk et al. (2016) to compute the residuals and test for the presence of an ETV signal.

#### 4.1.1 Dealing with Sources of Spurious ETV Signals

Due to a typically small number of points per eclipse, our timings are sensitive to various imperfections in the data processing, affecting the measured eclipse time and potentially introducing noise and/or fictitious signals in the ETV signal. Instrumental or astrophysical pulsations on top of the binary signal can change the shape of a single eclipse

which can mimic a timing variation. The detrending process attempts to remove these additional signals, but is not perfect, struggles at removing signals that happen during eclipse, and can also introduce spurious signals.

Also, all polyfits in the current version of the catalog use chains of four second-order polynomials, which does not always result in the ideal fit and can leave slight phase-dependent residuals. For the purpose of pipeline processing, we limit ourselves to second-order polynomials, but note that, for special cases and in-depth studies, higher precision timings can be obtained by increasing the order of the fit. In the cases when a binary has a period that is near-commensurate to *Kepler*'s 29.44 minute cadence, the period and cadence may beat, which results in a separate spurious signal. Any combination of these effects can cause issues in determining true and precise eclipse times when dealing with only a few data points.

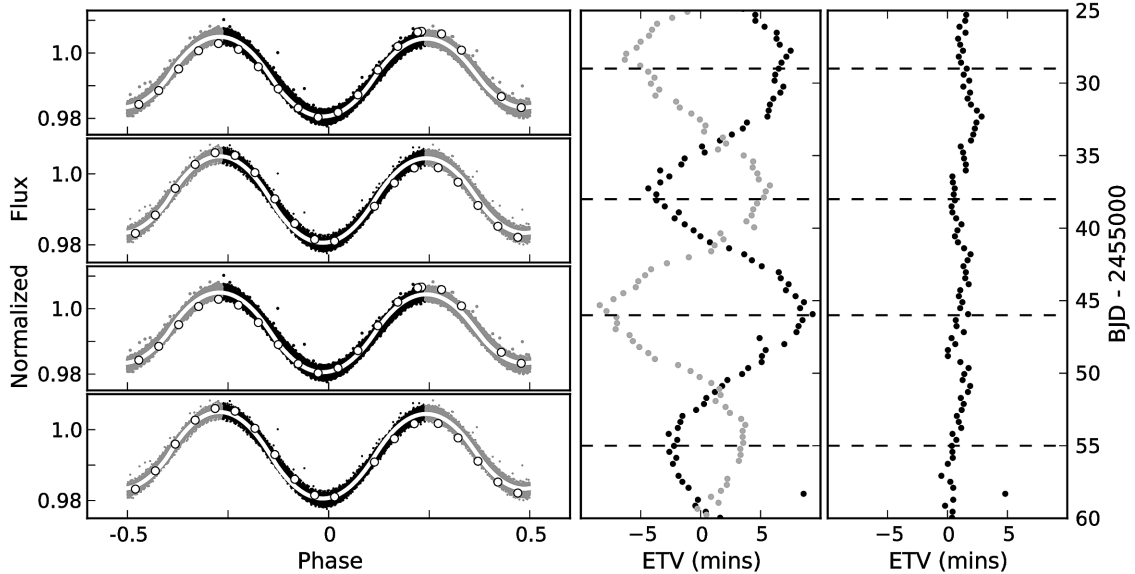


Figure 4.3 Determining eclipse timings using both eclipses will cancel the anti-phase effect and reveal any underlying signal. The plots on the left show a phased light curve with primary eclipse data in black and secondary in gray with the analytic ‘polyfit’ in white. These four plots highlight the data during individual cycles (shown in white on the left) at four different times noted in the ETV plots with the dashed line, showing the presence of spots. The plots on the right show the ETV as measured at for primary and secondary eclipses separately (middle) and full phase (right).

Figure 4.3 demonstrates how the cost function for the phase shift is affected by the

vertical discrepancy in the out-of-eclipse region, creating a fictitious signal in which the ETVs of the primary and secondary eclipse are in anti-phase. The left of Figure 4.3 plots four different eclipses, showing that over time the data in the out-of-eclipse region can be higher on either the right or the left. When measuring timings for the primary and secondary eclipses separately, the cost function will artificially be minimized by “pulling” the analytic function towards the region with lower flux. Since this will affect the primary and secondary in the opposite direction, we can mitigate for this effect by also running the fit over the entire phase. This effectively averages out the anti-phase effect in the primary and secondary eclipses, projecting the real ETV signal of the entire system. Figure 4.4 shows two cases where the anti-phase signal was removed, clearly showing whether there is a presence of any underlying ETV signal. These signals that show a “random walk” nature, often attributed to the presence of spots, are discussed by Tran et al. (2013).

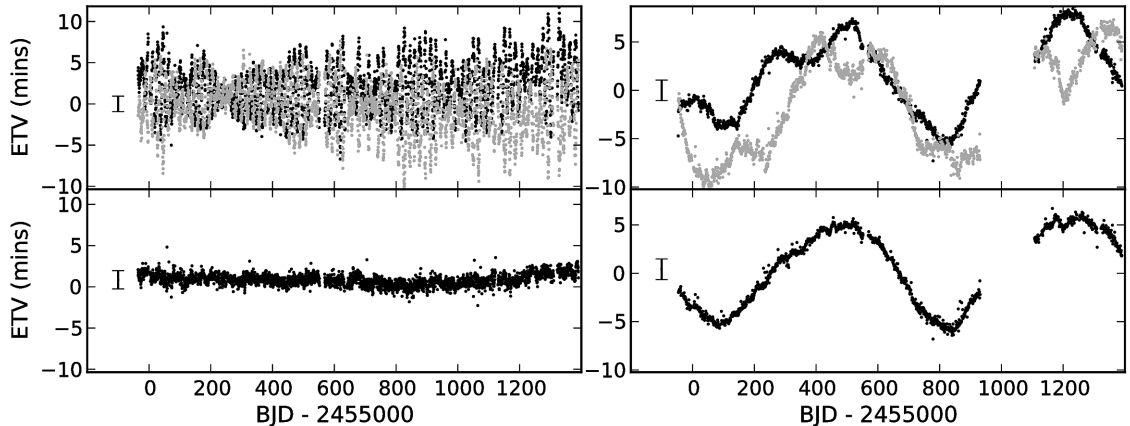


Figure 4.4 ETVs for KIC 6880727 (left) and 4451148 (right) determined for primary and secondary eclipses separately (top) and together (bottom). KIC 6880727 (left) shows an example with no underlying signal under the antiphase “noise”, while KIC 4451148 (right) shows a possible underlying third-body signal. Typical errors for ETV measurements are shown to the left of the data.

Unfortunately, as there is no rigorous way to discriminate between true and fictitious anti-phase signals, this process would also hide a physical ETV signal such as apsidal motion. As we are dealing with short-period binaries, most of these orbits will be quite circular so we do not expect to be able to detect any systems with apsidal motion anyway.

## 4.2 Identifying Candidate Triple and Higher-Order Systems

Our method requires at least three data points per timing, which allows us to get primary and secondary eclipse timings individually for long cadence data of binaries with periods as short as 3 hours and full phase timings for binaries as short as 1.5 hours. Plots and data for detrended light curves and eclipse times for the entire sample are available as a part of the *Kepler* Eclipsing Binary online catalog at <http://keplerEBs.villanova.edu>.

As ETVs are computed, the ephemerides in the catalog are refined by fitting a linear trend through the entire-phase timings and adjusting the values as necessary to get a “flat” trend. For any ETV with a long-term sinusoidal trend, this could introduce systematics depending on the part of the sine curve observed and used to fit the linear trend. In particular, for very long ETV signals (on the order of 1000 days and more), the measured orbital period of the binary will be anomalous because the variation cannot be accounted for from available data.

All ETV measurements were examined by eye for the presence of any interesting signal, discarding any that seem to be spurious based on their individual primary and secondary eclipse timings. We do not expect to see evidence of apsidal motion in many of our targets due to their short periods and, consequently, circular orbits. We also do not expect to be able to detect any signals due to gravitational quadrupole coupling (the Applegate Effect, see §5.3 and Applegate 1992). This mechanism is able to create period changes with amplitudes on the order of  $10^{-5}$  times the period of the binary, meaning a maximum of 3.5 seconds for a binary with a period of 4 days, falling well below our noise limits.

ETV signals that are sinusoidal in nature or show any sign of curvature are flagged and fit for both a third-body signal (see §5.7) and a parabolic mass transfer model (see §5.2). For the cases where we only see a sign of curvature and not a full cycle, we could either be seeing a section in a long period third body signal or mass transfer. To determine whether we consider the signal as a candidate third body or mass transfer, we compare the two

models using the Bayesian Information Criterion (Schwarz, 1978):

$$BIC = n \ln \left( \frac{1}{n} \sum (x_i - \hat{x}_i)^2 \right) + k \ln n \quad (4.1)$$

where  $x_i$  are the data,  $\hat{x}_i$  the model,  $n$  the number of data points, and  $k$  is the number of parameters used in the fit. For example,  $k = 6$  for the case of the eccentric LTTE model,  $k = 4$  for the circular LTTE model, and  $k = 3$  for the mass transfer model. The fit with the lower BIC value then determines whether we consider the signal as a candidate third body or mass transfer.

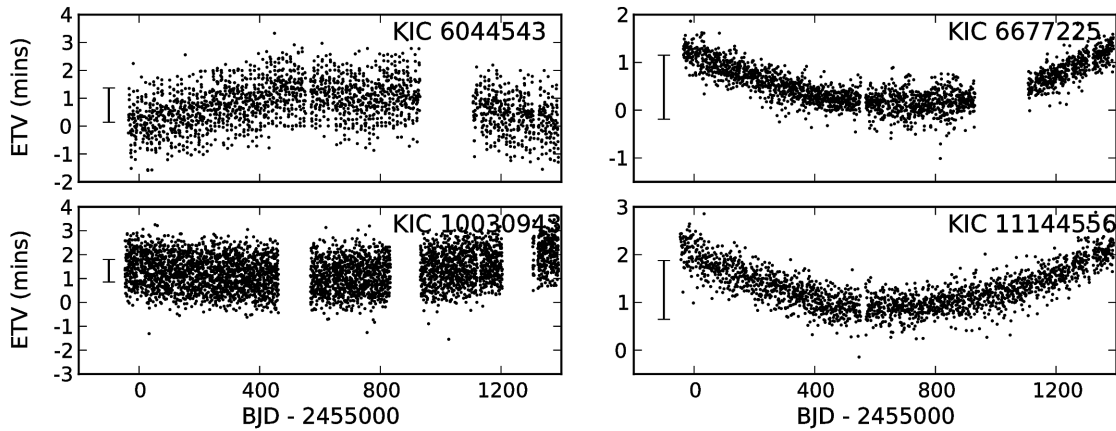


Figure 4.5 A selection of ETV signals that are better fit by a quadratic ephemeris than an LTTE fit.

Thirty-one ETV signals were better fit by a parabola than an LTTE orbit, and are possibly caused by mass transfer or the Applegate effect instead of the presence of a third body (Hilditch, 2001). These are listed in Table 4.1 with a selection shown in Figure 4.5.

236 binaries ( $\sim 20\%$  of the sample) were flagged as candidate third bodies. The results of the model fits are reported in Table 4.2 with a selection plotted in Figure 4.6. Based on the fitted period, we then divided these third body candidates into three groups. The first group contains third body signals with periods less than 700 days, such that there are at least two full cycles of the signal present in data through Q16. These systems have the highest confidence and are most likely due to the presence of a tertiary component. The

Table 4.1. ETVs with Parabolic Signals

KIC	KIC	KIC
2305372	3104113	3765708
4074532	4851217	4853067
5020034	5471619	5770860
5792093	6044064	6044543
6066379	6213131	6314173
6464285	6677225	7696778
7938468	7938870	8758161
9087918	9402652	9840412
9934052	10030943	10292413
10736223	11097678	11144556
11924311	...	...

second group contains signals with periods between 700 and 1400 days, such that there is at least one full cycle present. The last group contains signals with periods longer than 1400 days. Often these detections merely show some sign of curvature in the ETV signal and so a full sinusoidal signal cannot yet be confirmed. For this reason the fits generally have large errors and many of these may not even be true triple systems, particularly the signals on the closest binaries which are more likely to be due to mass transfer.

Gies et al. (2012) presented an initial study of eclipse timings in 41 *Kepler* binaries. Of their entire sample of 41 binaries, 40 are still in the *Kepler* EB Catalog (KIC 4678873 has since been removed from the catalog as a false positive), 32 fall under the scope of this paper (have a morphology less detached than 0.5), and 9 appear in our list of third-body signals. They identified 14 out of their original 41 as candidate third-body systems, with others being identified as likely caused by starspots, pulsations, and apsidal motion. Of their 14 candidate third-body systems, all 14 are still in the *Kepler* EB Catalog, 12 fall under the scope of this paper, and 9 appear in our list of third-body signals. Binaries that they list as candidate third-body systems, but we do not, either show significant noise or would be very long period LTTE orbits.

Table 4.2. ETVs with Potential Third-Body Signals

KIC	$\text{morph}_{bin}$	$P_{bin}$ (d)	$P_3$ (d)	$e_3$	$ALTTE$ (s)
2856960	0.60	0.259	$204.5 \pm 0.1$	$0.447 \pm 0.001$	$202 \pm 1$
3228863 <sup>†</sup>	0.65	0.731	$644.1 \pm 15.7$	$0.000 \pm 0.003$	$195 \pm 3$
3245776	0.96	1.492	$636.3 \pm 70.6$	$0.587 \pm 0.021$	$136 \pm 10$
3641446	0.95	2.100	$228.6 \pm 1.0$	$0.000 \pm 0.010$	$85 \pm 1$
4037163	0.58	0.635	$267.0 \pm 8.1$	$0.349 \pm 0.009$	$77 \pm 1$
4909707 <sup>†</sup>	0.72	2.302	$516.1 \pm 16.1$	$0.686 \pm 0.006$	$707 \pm 14$
5128972 <sup>†</sup>	0.74	0.505	$438.7 \pm 1.9$	$0.323 \pm 0.002$	$256 \pm 1$
5264818 <sup>†</sup>	0.91	1.905	$299.7 \pm 107.5$	$0.421 \pm 0.306$	$178 \pm 42$
5310387 <sup>†</sup>	0.96	0.442	$214.3 \pm 0.3$	$0.250 \pm 0.004$	$31 \pm 1$
5376552 <sup>†</sup>	0.82	0.504	$331.1 \pm 0.8$	$0.000 \pm 0.002$	$87 \pm 1$
5459373	0.97	0.287	$411.5 \pm 1.2$	$0.372 \pm 0.002$	$228 \pm 1$
5560831	0.60	0.868	$609.0 \pm 149.2$	$0.093 \pm 0.010$	$58 \pm 9$
6302592	0.93	1.578	$623.6 \pm 42.9$	$0.211 \pm 0.009$	$671 \pm 30$
6370665 <sup>†</sup>	0.94	0.932	$283.2 \pm 20.9$	$0.136 \pm 0.085$	$66 \pm 3$
7362751	0.73	0.338	$540.3 \pm 3.4$	$0.162 \pm 0.001$	$250 \pm 1$
7657914	0.72	0.475	$689.9 \pm 295.1$	$0.405 \pm 0.025$	$30 \pm 8$
7685689	0.77	0.325	$507.3 \pm 6.2$	$0.176 \pm 0.002$	$183 \pm 1$
7690843 <sup>†</sup>	0.64	0.786	$74.1 \pm 0.1$	$0.233 \pm 0.021$	$81 \pm 1$
8043961 <sup>†</sup>	0.63	1.559	$478.0 \pm 10.4$	$0.000 \pm 0.005$	$184 \pm 2$
8145477	0.88	0.566	$353.7 \pm 46.7$	$0.418 \pm 0.007$	$136 \pm 12$
8190491	0.95	0.778	$594.7 \pm 11.7$	$0.000 \pm 0.003$	$130 \pm 1$
8211618	0.73	0.337	$127.3 \pm 66.7$	$0.319 \pm 0.137$	$31 \pm 10$
8330092	0.80	0.322	$595.5 \pm 5.4$	$0.201 \pm 0.001$	$127 \pm 1$
8386865 <sup>†</sup>	0.99	1.258	$293.9 \pm 2.8$	$0.493 \pm 0.013$	$197 \pm 1$
8394040 <sup>†</sup>	0.77	0.302	$392.6 \pm 0.8$	$0.467 \pm 0.001$	$278 \pm 1$
8904448 <sup>†</sup>	0.74	0.866	$538.8 \pm 59.9$	$0.577 \pm 0.016$	$166 \pm 12$
9075704	0.68	0.513	$396.3 \pm 7.5$	$0.101 \pm 0.003$	$138 \pm 1$
9451096 <sup>†</sup>	0.54	1.250	$106.8 \pm 0.1$	$0.091 \pm 0.033$	$93 \pm 1$
9706078	0.55	0.614	$639.2 \pm 27.6$	$0.550 \pm 0.004$	$237 \pm 6$
9722737 <sup>†</sup>	0.78	0.419	$451.3 \pm 3.7$	$0.152 \pm 0.003$	$225 \pm 1$
9994475	0.76	0.318	$610.9 \pm 6.8$	$0.375 \pm 0.001$	$196 \pm 1$

Note. — An excerpt of the table listing identified third-body signals. The full table appears in Conroy et al. (2014b).

<sup>†</sup>Appears in Rappaport et al. (2013)

Table 4.3. ETVs crossmatched with Rappaport et al. (2013)

KIC	$P_{3,R}$ (d)	$P_3$ (d)	$A_{LTTE,R}(s)$	$A_{LTTE}(s)$
3228863	668.4	$644.1 \pm 15.7$	189{187,194}	$195 \pm 3$
4647652	753.5	$755.2 \pm 44.3$	228{183,274}	$239 \pm 9$
4909707	505.3	$516.1 \pm 16.1$	493{378,627}	$707 \pm 14$
5128972	447.8	$438.7 \pm 1.9$	259{244,271}	$256 \pm 1$
5264818	296.3	$299.7 \pm 107.5$	145{107,196}	$178 \pm 42$
5310387	214.2	$214.3 \pm 0.3$	31{ 27, 37}	$31 \pm 1$
5376552	334.5	$331.1 \pm 0.8$	94{ 91, 98}	$87 \pm 1$
6370665	285.9	$283.2 \pm 20.9$	67{ 61, 74}	$66 \pm 3$
6531485	48.3	...	72{ 31,109}	...
7690843	74.3	$74.1 \pm 0.1$	71{ 51, 91}	$81 \pm 1$
8043961	476.7	$478.0 \pm 10.4$	194{179,213}	$184 \pm 2$
8192840	803.9	$1045.9 \pm 185.0$	208{187,223}	$260 \pm 30$
8386865	293	$293.9 \pm 2.8$	171{156,210}	$197 \pm 1$
8394040	394.8	$392.6 \pm 0.8$	369{345,391}	$278 \pm 1$
8904448	548.1	$538.8 \pm 59.9$	171{158,192}	$166 \pm 12$
9451096	106.7	$106.8 \pm 0.1$	90{ 59,144}	$93 \pm 1$
9722737	443.9	$451.3 \pm 3.7$	230{225,236}	$225 \pm 1$
9912977	753.7	$780.4 \pm 95.2$	105{ 94,117}	$96 \pm 7$
10226388	934.9	$965.3 \pm 183.8$	465{434,493}	$457 \pm 58$
10991989	554.2	$554.8 \pm 64.1$	256{239,274}	$232 \pm 17$
11042923	839	$984.4 \pm 63.9$	223{213,230}	$276 \pm 11$

Note. —  $P_{3,R}$  and  $A_{LTTE,R}$  are the period and amplitude as reported by Rappaport et al. (2013)

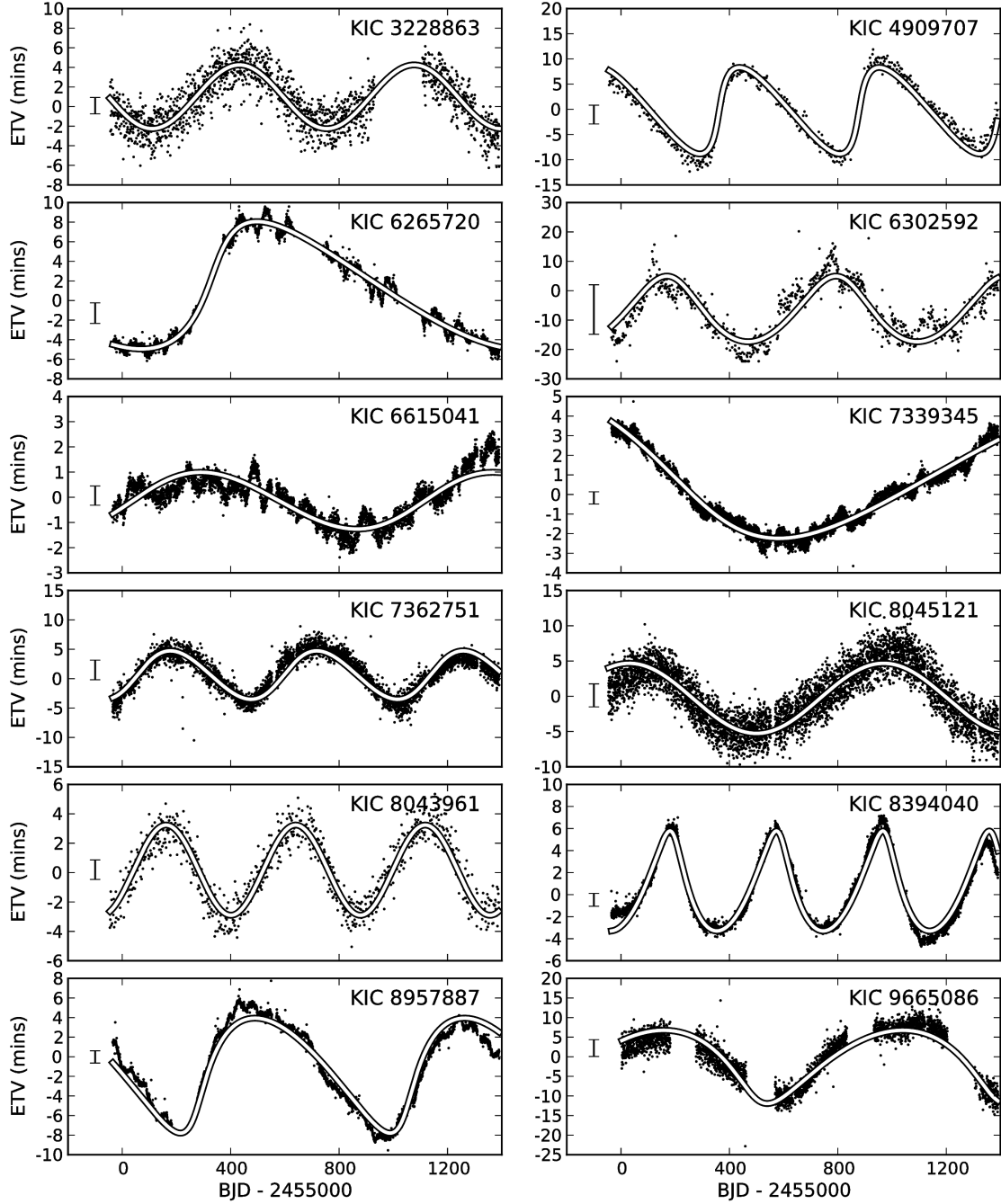


Figure 4.6 Gallery of select ETV signals found in close binaries with LTTE fits. These are KIC 3228863, 4909707, 6265720, 6302592, 6615041, 7339345, 7362751, 8045121, 8043961, 8394040, 8957887, and 9665086. Typical errors for ETV measurements are shown to the left of the data.

Rappaport et al. (2013) also reported 39 triple-star *Kepler* binaries due to ETV signatures. Of these 39, 21 fall under the scope of this paper, 19 of which also appear in our list

of third-body signals, with the other two determined to be unlikely caused by a third-body due to their very short periods and notable spot activity. The detections that overlap both of these studies are noted in Table 4.3. In most cases, the model fits from both studies are consistent. In general, due to our treatment of the full *Kepler* dataset, tertiary parameters should now be more precise and longer period third body signals are now more apparent. Any disagreement is likely due to a slightly differ inner-binary ephemeris or the addition of the physical delay in their models (see also §5.4 for a discussion of these dynamical contributions).

#### 4.2.1 Higher-Order Systems

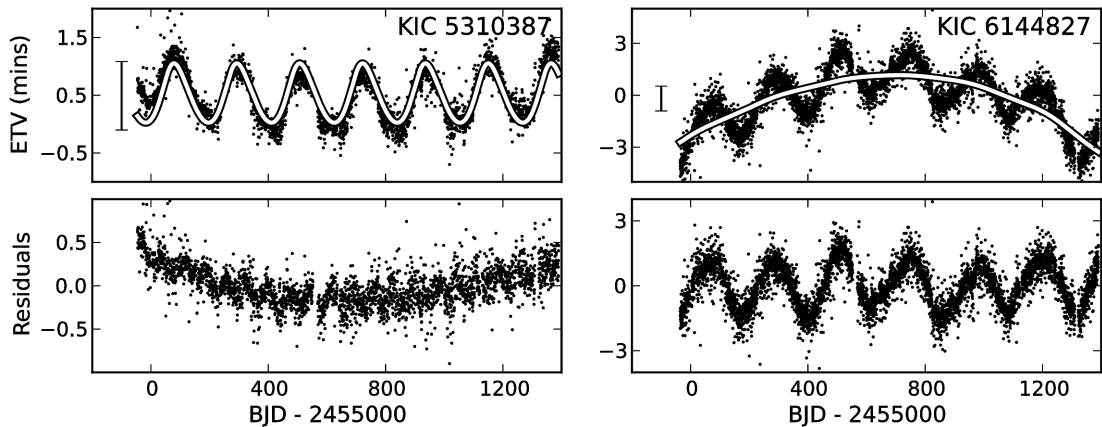


Figure 4.7 KIC 5310387 and 6144827 are among several ETV signals with residuals that suggest another parabolic or LTTE signal, possibly indicating the presence of a fourth body.

It is also possible that some of these ETVs could be composed of multiple signals. KIC 5310387, 6144827, 8145477, 11612091, and 11825204, for example, may have both an LTTE and quadratic component or two LTTE signals as shown in the residuals in Figure 4.7. In general, the stronger signal is fitted and noted.

#### 4.2.2 Systems Confirmed through Eclipse Events

Some of these systems also exhibit extra eclipse events (see §2.3.1). When these eclipses can be phased to the same period as the LTTE signal in the ETVs, this can provide strong evidence that the system is indeed a higher-order system. Figure 4.8 shows one of these systems, KIC 2856960, in which eclipse events and the ETV signal can easily be seen to be caused by the presence of a third component in the system.

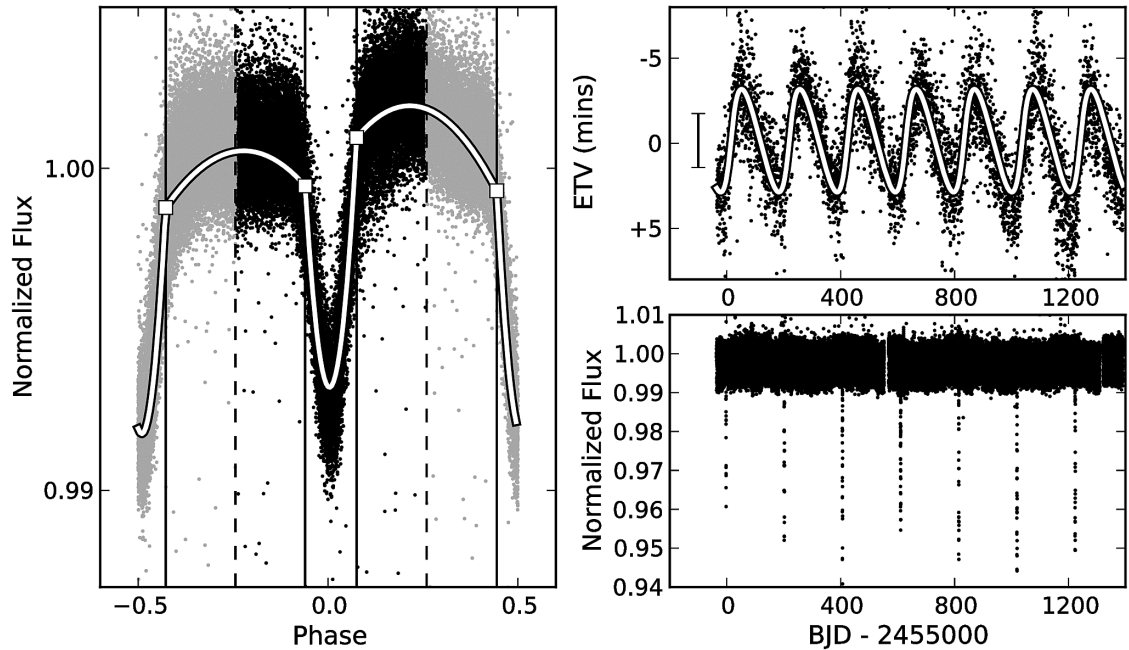


Figure 4.8 A triple eclipsing star KIC 2856960. Left: the detrended light curve phased at the inner period of 0.26-d. The white line is the polyfit function, and white rectangles are the knots. Dashed lines delimit the phase space of the primary and secondary eclipse; these are used separately to obtain primary and secondary ETVs. Upper right: the measured ETVs (black points) and the best light-time travel fit (white line), yielding the outer period of 205.5 days. Lower right: the detrended light curve, with the tertiary eclipses clearly visible.

KIC 2835289, shown in Figure 4.9, is particularly interesting because the inner binary is an ellipsoidal variable with a short period below one day. As the ellipsoidal variable does not eclipse but the third body does, we know that the system cannot be coplanar and can model the mutual inclination between the two orbits. Furthermore, the shape of the LTTE signal tells us that the third component is on a fairly eccentric orbit. Initial models (Conroy et al., 2015) suggest that the mutual inclination may be consistent with the distributions expected from KCTF (see §1.2), and since the inner binary is near the period peak of close binaries, may be a prime example of a post-KCTF system. This system is the target of a future study (Conroy et al, in prep).

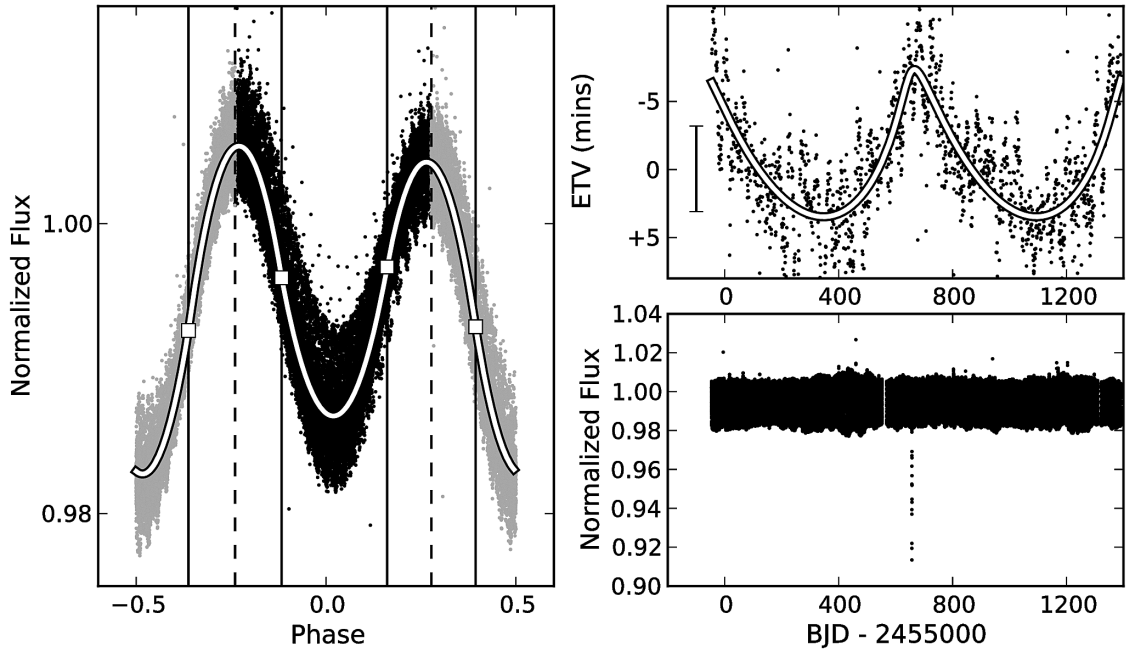


Figure 4.9 KIC 2835289 is an ellipsoidal variable with a period of 0.857 days. We can see one tertiary eclipse in the light curve and the ETV signal can put an additional constraint on the expected period of a potential third-body.

### 4.3 Statistics

We found a third body rate of  $\sim 20\%$  in our sample of close binaries, nearly all of which have inner binary periods shorter than 3 days (Figure 4.10). This is much lower

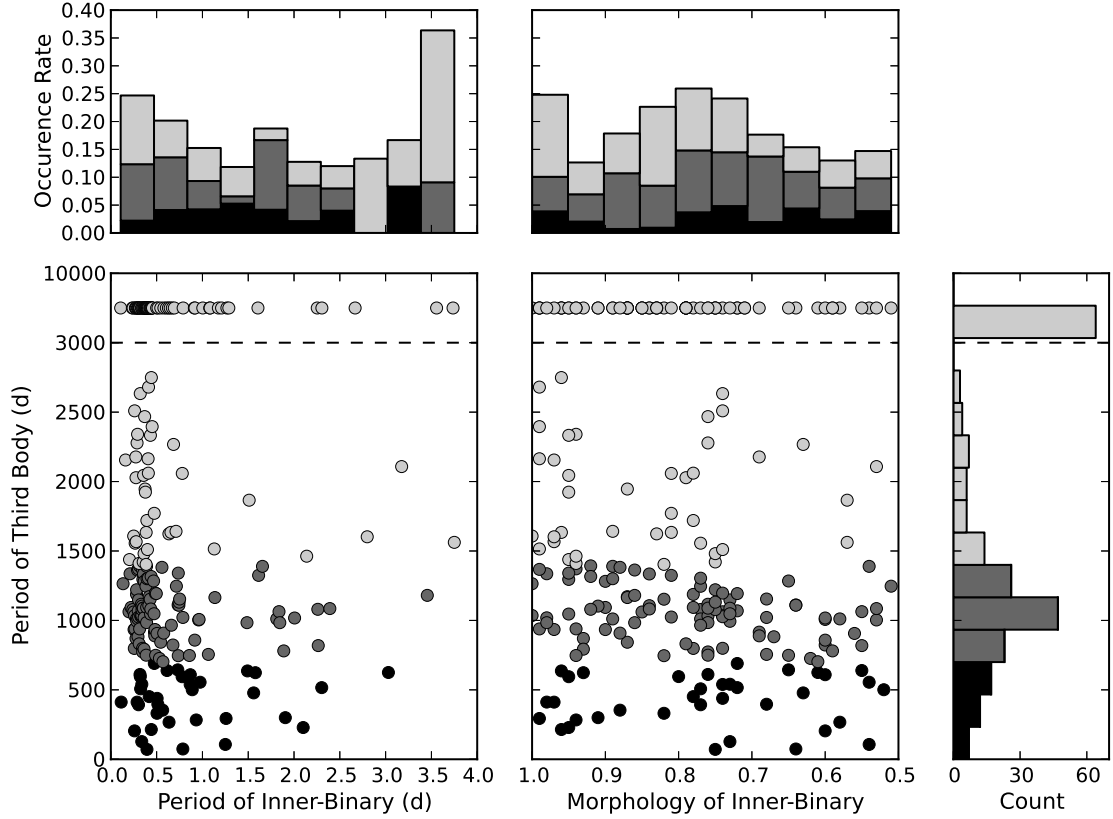


Figure 4.10 Distribution of period of potential third body companions versus the inner-binary period (left) and morphology (right). Third body periods greater than 3000 days are all placed in the final bin despite their modeled periods. The different colors represent the three different samples of binaries represented in Table 4.2, determined by the period of the potential third body. The top histograms show the occurrence rate of candidate third bodies for each bin in period or morphology, and the histogram on the right shows the number of third body candidates at each period.

than the third body rate of 96% found by the previous studies mentioned. However, our identification of tertiary companions is certainly a lower limit for several reasons.

First, our ability to detect a third body is very sensitive to both inclination and mass of the third body, such that low-mass tertiaries and/or tertiaries whose orbital planes are highly inclined relative to the inner binary orbital plane do not present detectable LTTE effects. Of our total sample of 1279 binaries, 3 ( $< 1\%$ ) show an LTTE orbit and visible tertiary eclipses. 111 ( $\sim 10\%$ ) have LTTE orbits with periods shorter than the span of our photometric data but do not show tertiary eclipses, suggesting that the orbits are not well

enough aligned to show eclipses or the eclipses fell in a gap in the data. Thus, there is evidence from these examples that, in a few percent of cases, we are indeed missing true third bodies because of inclination non-alignment. 94 ( $\sim 7\%$ ) have LTTE orbits with periods longer than the photometric baseline. In these cases we do not have well constrained periods and our chances of detecting a tertiary eclipse are poor.

A second reason that our determination of the third-body occurrence is likely a lower limit is that the very close binaries that comprise our sample here generally present more noise in the ETV signal, which could easily bury a weak LTTE signal. We have employed a method that minimizes false positives due to spurious ETV signals, and thus necessarily have eliminated some potentially true LTTE signals.

Third, and perhaps most important, the limited timespan of the *Kepler* data at the time of this study ( $\sim 1400$  days) significantly restricts us to detect third bodies with orbital periods comparable to or shorter than 1400 days. Relative to the full span of tertiary separations found in previous works (Tokovinin, 1997; Tokovinin et al.; Dhital et al., 2010; Law et al., 2010), with separations as large as  $\sim 1$  pc, we are at present sampling only the relatively closest tertiary companions. Indeed, Tokovinin et al. found among tight binaries that the rate of third bodies with orbital periods less than  $\sim 3$  years (comparable to our limit based on the duration of the available *Kepler* data) is  $15\% \pm 3\%$ . Thus our finding of a third-body occurrence rate with a period less than 1400 days of  $\sim 10\%$  is compatible with the expected rate, though it appears we are likely still missing a fraction of some systems for the reasons already mentioned.

The distribution of periods of potential third body orbits is also shown in Figure 4.10. We can clearly see a falloff in detection past the current length of the *Kepler* mission of  $\sim 1400$  days, as expected. However, for third-body periods shorter than  $\sim 1400$  days, for which our detectability is relatively good, the occurrence rate does appear to increase toward longer third-body periods, consistent with the period distribution of third bodies among tight binaries found by Tokovinin et al.. Furthermore, we find that the triples on

the widest orbits are found around the shortest period binaries, which is consistent with models that tighten the inner binary orbit through the presence, and gradual widening, of a companion.

By identifying these candidate triple systems through ETVs, we can continue to follow-up these systems to obtain additional observations — extending the time baseline on the ETVs and therefore the precision of the fitted third body orbits, obtaining high-precision photometry at times of expected triple eclipses, and obtaining spectroscopy so that radial velocities can be extracted. With the combination of these various types of observations, we can then precisely fit a physical model to an individual system. In order to do so, we must account for all astrophysical contributions to the ETVs and create a physical model capable of handling the dynamics of triple and higher-order systems in addition to the necessary considerations for modeling high-precision data already discussed in §3.

## Chapter 5

### Astrophysical Contributions to Eclipse Timing Variations

*This chapter includes excerpts and figures adapted from Conroy et al. (2018), used with permission from The Astrophysical Journal.*

Eclipse Timing Variations (ETVs) occur whenever an eclipse *appears* at a time other than that predicted by the linear ephemeris. These contributions can be split into two main categories: time-dependent changes to the orbit itself that influence the *true* time of the eclipse and *apparent* effects caused by the finite speed of light. Examples of the former include apsidal motion (§5.1), mass transfer (§5.2), the Applegate Effect (§5.3), and dynamical effects in triple systems (§5.4). Examples of the latter include parallax and proper motion effects (§5.5), Rømer delay (§5.6), light travel time effect in triple systems or systems with radial barycentric velocity (§5.7), the Shklovskii Effect (§5.8), as well as a previously overlooked effect called Barycentric and Asymmetric Transverse Velocities (BATV, discussed in detail in §5.9 and Conroy et al. 2018).

Depending on the circumstances of any given binary system, some or several of these effects may be negligible while others dominate. Many of these effects are particularly prevalent in close binary or triple systems and so are especially important to consider when attempting to robustly model any of these systems. Most of these effects (all light time and dynamical effects) are implemented into the physical model within PHOEBE and are discussed in §6.

#### 5.1 Apsidal Motion

Eccentric binaries can undergo apsidal motion or precession resulting in variations to the eclipse times. This precession can be caused both by the non-point-mass nature of the

stars as well as general relativistic effects. Together, these result in a time-dependence to the argument of periastron,  $\omega$ :

$$\omega = \omega_0 + \dot{\omega}E \quad (5.1)$$

where  $E$  is the epoch number (number of orbital cycles since  $t_0$ ) and  $\omega_0$  is defined as the argument of periastron at  $E = 0$ .

This changing argument of periastron, in turn, affects the projected separation between the primary and secondary eclipses,  $e \cos \omega$ , as well as the widths of the eclipses,  $e \sin \omega$ . The eclipses will be separated by exactly half-phase when the line of periapsis lies along the line of sight (i.e., eclipses occur at periastron and apastron) and most extremely separated when the line of periapsis lies along the plane of sky. The precession of the argument of periastron,  $\dot{\omega}$ , then results in the primary eclipses and secondary eclipses exhibiting sinusoidal-like ETVs in antiphase to each other.

Gimenez and Garcia-Pelayo (1983) (see also Todoran 1972 for a similar expression with terms up to the third order in  $e$ ) provide the following expression for the time of eclipse:

$$T = T_0 + P_s E + (j - 1) \frac{P}{2} - \frac{P}{\pi} \sum_{n=1}^5 \left( \frac{e}{2} (3 - 2j) \right)^2 \left\{ \sum_{m=1}^3 \left( \frac{e}{2} \right)^{2m-2} f_{mn}(i) \right\} \sin n\bar{\omega} \quad (5.2)$$

where  $T$  is the time of a given eclipse at epoch  $E$ ,  $T_0$  is the time of eclipse at  $E = 0$ ,  $P_s$  is the sidereal orbital period,  $e$  is the eccentricity,  $\bar{\omega}$  is the argument of periastron at epoch  $E$  plus  $\pi/2$  (i.e.,  $\bar{\omega} = \omega_0 + \dot{\omega}E + \pi/2$ ),  $j = 1, 2$  for primary and secondary eclipses, respectively, and

$$\begin{aligned} f_{1n}(i) &= \left( 1 + \frac{1}{n} \right) + \cot^2 i \sum_{k=1} n(n-k+1)(\csc^2 i)^{(j-1)} \\ f_{2n}(i) &= \frac{2}{n+2} \{ (6-n)(n+2) - (-1)^n \} + n f_{1(n+2)} - 6 f_{1n} \\ f_{3n} &= 2 \{ f_{15} - 3(f_{13} - f_{11}) \} - 6.4 \end{aligned} \quad (5.3)$$

given that  $f_{2n} = 0$  for  $n > 3$  and  $f_{3n} = 0$  for  $n > 1$ . The period of the apsidal motion is then:

$$U = \frac{2\pi}{\dot{\omega}} P_a \quad (5.4)$$

where  $P_a$  is the anomalistic period (the time between two periastron passages). The relation between the sidereal and anomalistic periods is:

$$P_s = P_a \left(1 - \frac{\dot{\omega}}{2\pi}\right) \quad (5.5)$$

## 5.2 Mass Transfer

For a close binary system in which one component is overflowing the Roche lobe at L1, mass transfer can occur between the two components, resulting in a change in the semi-major axis and orbital period of the system (e.g. Pettini 2013). By defining the mass transfer from  $M_2$  to  $M_1$  and under the assumption of zero mass-loss from the system (i.e., conservative mass transfer),  $\dot{M}_1 = -\dot{M}_2$ . The total angular momentum of the system must then be conserved throughout this process. Here we ignore the rotational angular momenta of the individual stars and write the total orbital angular momentum of the system, assuming a circular orbit:

$$L = \mu \sqrt{GM_{\text{tot}}a}, \quad (5.6)$$

where  $\mu \equiv \frac{M_1 M_2}{M_{\text{tot}}}$  and  $M_{\text{tot}} \equiv M_1 + M_2$ . By forcing the time-derivative of  $L$  to be zero, the orbit must shrink when  $M_1 < M_2$  (mass transfer from the more massive star to the less massive) and expand when  $M_1 > M_2$  (mass transfer from the less massive star to the more massive):

$$\frac{1}{a_0} \dot{a} = 2\dot{M}_1 \frac{M_1 - M_2}{M_1 M_2}. \quad (5.7)$$

According to Kepler's third law,  $P \propto a^{3/2}$ , the orbital period of the system must also

change:

$$\frac{1}{P_0} \dot{P} = \frac{3}{2} \frac{1}{a} \dot{a} = 3\dot{M}_1 \frac{M_1 - M_2}{M_1 M_2} \quad (5.8)$$

Any linear change in the orbital period will show itself in the ETVs as a quadratic term:

$$T = T_0 + P_0 E + \frac{1}{2} P_0 \dot{P} E^2. \quad (5.9)$$

Stępień and Kiraga (2013) caution against using measured ETVs in single systems to argue for the presence of mass transfer, noting that the Applegate Effect (§5.3) or presence of third bodies (§5.7) are generally more likely scenarios that can exhibit a similar shape in the ETV curve.

### 5.3 Applegate Effect

The Applegate Effect (Applegate, 1992) describes period modulations in binary systems on the order of  $\Delta P/P \sim 10^{-5}$  over timescales of decades caused by gravitational coupling between the orbit and oblateness of one or both stars. As an active star goes through its activity cycle, the magnetic torque causes changes in the distortion of the outer layers of the star, resulting in a change in the distribution of the rotational angular momentum. This change in the rotational angular momentum can then be exchanged with the system's orbital angular momentum, ultimately affecting the orbital period of the binary.

As the Applegate Effect is driven by magnetic fields, the period of the ETVs must correspond to the observed photometric variation due to the underlying activity cycle with an expected amplitude in the luminosity of  $\Delta L/L \sim 0.1$  (Applegate, 1992).

The relation between the amplitude of the ETV signal and the orbital period modulation is (see Applegate 1992, Equation 38):

$$A_{\text{Applegate}} = \frac{\Delta P}{P} \frac{P_{\text{Applegate}}}{2\pi}. \quad (5.10)$$

Note that, as  $P_{\text{Applegate}}$  (the length of the orbital period modulation) depends on the activity cycle, it may not be strictly periodic.

The time of an eclipse, corrected from the linear ephemeris, is given by (see Applegate 1992, Equation 37):

$$T = T_0 + P_0 E + \frac{1}{2} P_0 \dot{P} E^2 + \frac{A_{\text{Applegate}} P_0}{2\pi v} \cos(P_0 v E), \quad (5.11)$$

where  $E$  is the cycle number,  $P_0$  is the orbital period provided in the linear ephemeris, and  $v = P_{\text{Applegate}}/2\pi$ .

#### 5.4 Dynamical Effects

Masses in a triple or higher-order system can interact with each other, exchanging angular momentum between the various orbits and spins of the components. These orbital perturbations can then affect the orbital periods, resulting in ETVs from the linear ephemeris assuming a fixed period.

In the case of a hierarchical triple system, the amplitude of this dynamical perturbation on the orbital period of the inner binary is approximated by Rappaport et al. (2013), Equation 10, as:

$$\begin{aligned} A_{\text{dyn}} &= \frac{3}{8\pi} \frac{M_3}{M_{123}} \frac{P_{\text{in}}^2}{P_{\text{out}}} (1 - e^2)^{-3/2} \\ &= \frac{3}{4} G^{-1/2} q_{\text{out}} a_{\text{in}}^3 a_{\text{out}}^{-3/2} M_{123}^{-1/2} (1 - e^2)^{-3/2}. \end{aligned} \quad (5.12)$$

Multiple formulations and analytical expressions for the full ETV signal can be found in many sources, including Harrington (1968, 1969); Soderhjelm (1975, 1982); Mayer (1990); Borkovits et al. (2003, 2011); Rappaport et al. (2013).

Generally, the contribution to ETVs from these interactions increases as the system becomes more tightly packed and as the mass of the third object increases. However, there is a limit to how tightly a system can be packed and still be dynamically stable (see,

for example, Harrington 1972; Bailyn 1987; Eggleton and Kiseleva 1995; Mardling and Aarseth 2001; Mikkola 2008). Although the stability limit varies with eccentricity and mass ratio, systems generally become unstable if  $a_{\text{in}}/a_{\text{out}} > 0.1$ . For systems that are near the stability limit, the dynamical effects can change the orbital period, and therefore contribute to the ETVs, quite significantly.

## 5.5 Parallax and Proper Motion Effects

Scharf (2007) and Rafikov (2009) discuss the effects of parallax and proper motion on transit (and eclipse) times due to the apparent precession of the orbit as the system moves on the plane of sky throughout Earth’s orbit around the Sun. This is most pronounced when the binary orbit and Earth-Sun orbit are coplanar. Scharf (2007) estimates the magnitude of this effect to be:

$$\Delta t = \frac{RP}{\pi d} \quad (5.13)$$

where  $R$  is the orbital radius of Earth about the Sun (1 AU),  $P$  is the orbital period of the eclipsing system, and  $d$  is the distance to the object. For most cases this effect will contribute, at most, an amplitude of  $\Delta t \sim 10^{-1} - 10^{-2}$  s to ETVs, which is well below our current timing precision abilities.

In the case where the orbits are orthogonal, Scharf (2007) also discusses the resulting change in transit duration,  $\tau$ , due to an apparent change in inclination throughout Earth’s orbit. For systems within 100 pc of Earth,  $\Delta\tau/\tau$  can be estimated to vary between 0.001% (for a 10 day period) and 10% (for a 1000 day period).

Scharf (2007) also notes that the same principle applies to barycentric motion of the system relative to Earth. If a system exhibits large space velocities, an apparent precession or change in inclination, strictly due to the change in observing angle, could appear in the ETVs or duration variations. In §5.9 we present the formalism of a new effect, called BATV, that describes the light time effects caused by transverse motion on the sky, which

acts in addition to these geometric observing-angle effects.

## 5.6 Rømer Delay

The so-called *Rømer delay*, named after Ole Rømer who computed the speed of light from the eclipses of Io by Jupiter in 1676, has long been applied to eclipsing binary star systems and transiting planets to account for the effect of the finite speed of light on the observed timings of eclipses.

By definition, the eclipsed component is always behind, and therefore further away from the observer, than the eclipsing component. Due to the different distances the photon must travel from each component to the observer, the observer “sees” each component at different phases along their respective orbits — resulting in a shift in the timing of an observed eclipse.

Interestingly, this affects the primary and secondary eclipses in opposite directions, resulting in a shift in the phase separation between eclipses. Kaplan (2010) provides the following expression, adapted from Fabrycky (2010), for this phase-shift (Kaplan 2010, Equation 4, adapted to be translated from time- to phase-space):

$$\Delta\Phi_{\text{sep}}(i \rightarrow 90^\circ) = \frac{1}{P} \left( \frac{2GM_1 P^2}{\pi^2 c^3} \right)^{1/3} \frac{(1-q)}{(1+q)^{2/3}}. \quad (5.14)$$

As this is a function of the size of the orbit, the eccentricity, and the mass-ratio, this separation of eclipses can be used to constrain the mass-ratio if the other values can be constrained independently through, for example, radial velocities. This has been successfully applied to observable systems, including a *Kepler* eclipsing sdB+dM binary (Barlow et al., 2012). §5.9.4 discusses this approach in more detail, introducing the contribution of barycentric motion (BATV).

## 5.7 Light Travel Time Effect

Although often interchangeable with the Rømer delay discussed in §5.6, we make the distinction here that Rømer delay accounts for the light time delay between the two eclipsing components whereas the Light Travel Time Effect (LTTE) accounts for the light time delay between an eclipsing binary and some reference frame, often the barycenter of a higher-order system.

In the case of single binary systems with a systemic radial velocity, the entire system is either receding or approaching the observer at some (usually) constant projected velocity. The path the photon has to travel between one eclipse and the next is therefore changing at a linear rate — resulting in an anomalous orbital period. For this reason, from photometry alone, it is (nearly) impossible to decouple the orbital period from a reasonable range of systemic velocities. However, with observed radial velocities, the systemic velocity can easily be measured and used to correct the observed period (i.e., time between two successive primary eclipses in the absence of other ETV sources) from the true orbital period of the system.

In the case of a higher-order system, this systemic radial velocity is caused by the motion of the binary about the common center of mass of the entire system, and is therefore time-dependent. Borkovits et al. (2003, 2007, 2011); Rappaport et al. (2013); Conroy et al. (2014b) provide analytical expressions for the contribution of LTTE to ETVs in a hierarchical triple system:

$$ETV_{LTTE} = A_{LTTE} \left[ (1 - e_3^2)^{1/2} \sin E_3(t) \cos \omega_3 + (\cos E_3(t) - e_3) \sin \omega_3 \right], \quad (5.15)$$

where:

$$\begin{aligned} E_3(t) &= M_3(t) + e_3 \sin E_3(t), \\ M_3(t) &= (t - t_0) \frac{2\pi}{P_3}, \\ A_{LTTE} &= \frac{G^{1/3}}{c(2\pi)^{2/3}} \left[ \frac{m_3}{m_{123}^{2/3}} \sin i_3 \right] P_3^{2/3}, \end{aligned} \quad (5.16)$$

and  $t_0$  is a time offset,  $m_3$  is the mass of the third body,  $m_{123}$  is the mass of the entire system, and  $P_3$ ,  $i_3$ ,  $e_3$ ,  $\omega_3$ ,  $E_3(t)$ , and  $M_3(t)$  are the period, inclination, eccentricity, argument of periastron, eccentric anomaly, and mean anomaly of the third body orbit, respectively.

## 5.8 Shklovskii Effect

Shklovskii (1970) accounted for the transverse velocity of pulsars resulting in a positive time-derivative to the observed rotation period. Rafikov (2009) applied this to transit timing and Kaplan et al. (2014) used the effect in the case of a double white-dwarf binary.

As described in §5.7, a system with a radial systemic velocity results in an anomalous orbital period due to the increasing or decreasing distance between the source and observer. Here the Shklovskii effect occurs due to transverse motion of a system, resulting in a time-dependent contribution to the radial systemic velocity (i.e., due to a linear transverse velocity on the spherical plane-of-sky). This will always result in the system receding from the observer, and therefore a positive  $\dot{P}$ .

Rafikov (2009) writes the expression for eclipse/transit times as follows:

$$\dot{P}_{\text{Shk}} = 9.6 \left( \frac{v_t}{30 \text{ km s}^{-1}} \right) \frac{100}{D} \left( \frac{a}{10 R_\odot} \right) \mu\text{s yr}^{-1} \quad (5.17)$$

where  $v_t$  is the transverse systemic velocity,  $D$  is the distance to the system, and  $a$  is the semi-major axis.

Rafikov (2009) also notes that even for nearby systems with large proper-motion, this is

unlikely to be observed on a timescale of 10 years, even with *Kepler* photometric precision.

## 5.9 Barycentric and Asymmetric Transverse Velocities

Here we present a non-relativistic contribution to the observed timings of eclipses (hereafter, our use of the word “eclipse” can also be applied to occultations and transits) caused by any asymmetry in the transverse velocities of the two objects relative to the observer. This can be the result of internal (i.e., non-unity mass-ratio) or external (i.e., barycentric motion, additional components) causes. GAIA Data Release 1 (DR1) has recently released proper motions for 2 million sources brighter than 20.7 magnitude (Gaia Collaboration et al., 2016a,b; Lindegren et al., 2016), making it possible to obtain this information for any source in the very near future.

### 5.9.1 General Theory

In order to define the observed time of eclipse, the positions of both bodies must be individually corrected according to the light travel time between their respective instantaneous positions and some fixed reference frame. Any asymmetry in the transverse velocities of these two bodies relative to the observer, therefore, results in an unequal correction in their positions. This asymmetry can result from two root causes. A non-unity mass-ratio in the system will result in the lower-mass object having a higher velocity than the higher-mass object at any given time throughout the orbit. Additionally, any barycentric transverse (i.e., on the plane of the sky rather than along the line of sight) motion will affect the absolute transverse velocities of both components, relative to the observer. Here we provide a derivation of the effect that BATV has on the observed time of eclipse.

If we assume that all orbital motion is in the  $xz$  plane with  $z$  pointing towards the observer (therefore guaranteeing an eclipse), then we can define the condition for an observed eclipse as:

$$x_b(t_b) = x_f(t_f), \quad (5.18)$$

where the subscripts “b” and “f” refer to the back (eclipsed) and front (eclipsing) star, respectively. This condition states that the stars must appear aligned w.r.t. a photon traveling towards the observer. The photon that is emitted by the back star at  $x_b(t_b)$  at time  $t_b$  will be intercepted by the front star at  $x_f(t_f)$  at time  $t_f$  (see Figure 5.1 for a schematic). By expressing the x-positions of both stars in terms of their x-velocities, our condition for an observed eclipse becomes:

$$-\int_{t_b}^{t_{\text{align}}} v_{x,b}(t) dt = \int_{t_{\text{align}}}^{t_f} v_{x,f}(t) dt, \quad (5.19)$$

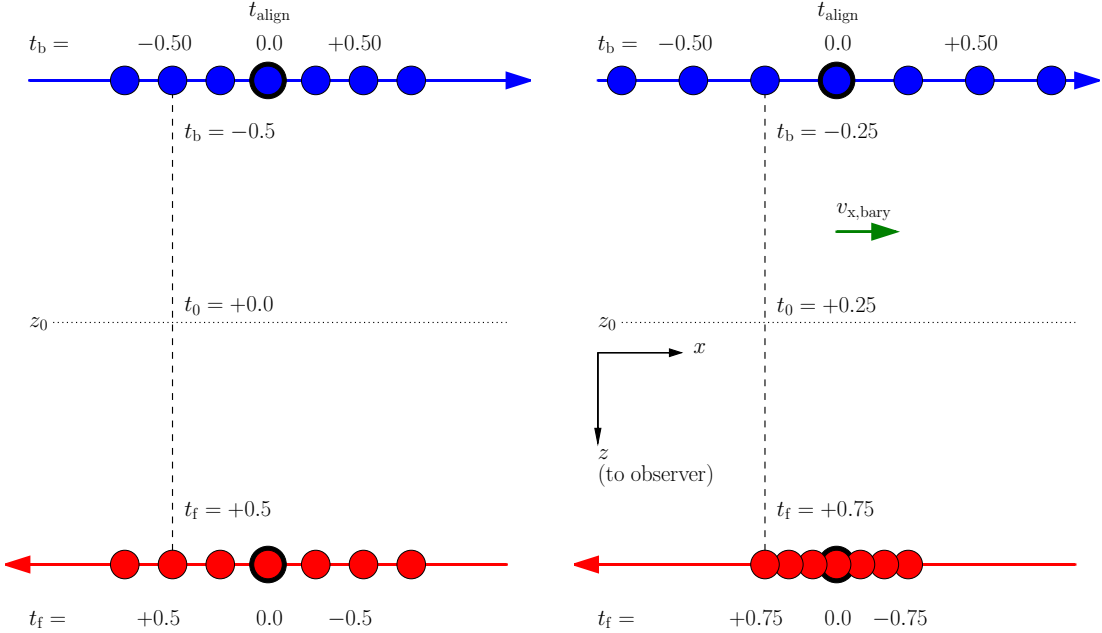


Figure 5.1 2D schematic representation of the effect BATV has on observed eclipse times for an equal-mass binary system. On the left is a system with no barycentric motion, such that both components have equal—but opposite—velocities. On the right is a representation of the same system, but with the addition of transverse barycentric motion, such that the speed of the star in front is  $1/3$  the speed of the star in back, relative to the observer. The separation between the two stars in both cases is equivalent to one light-time unit. At time  $t = t_{\text{align}} = 0.0$ , the stars are in geometric alignment (i.e., the time of eclipse as provided by the ephemeris as  $c \rightarrow \infty$ ). An eclipse is observed when a photon that was emitted by the back (blue) star travels the distance to the front (red) star and is intercepted. In other words, the x-position of the stars must align while being separated by exactly the time it takes the photon to cross the distance between them. We define the time of eclipse as the time at which the photon passes the plane containing the system barycenter,  $z_0$ . For the case with no barycentric motion (left), the eclipse is observed at  $t=0$  (although shifted to the left in space), whereas the case with positive barycentric motion (right) has a shift in the observed eclipse time by 0.25 light-time units.

where  $t_{\text{align}}$  is the time at which the stars are in geometric alignment, i.e. when  $c \rightarrow \infty$ .

For any photon traveling in the positive z-direction towards the observer between the two stars, the times must satisfy the following condition, accounting for the light travel time:

$$t_f - t_b = \frac{z_f(t_f) - z_b(t_b)}{c}. \quad (5.20)$$

The time of observed eclipse can be given w.r.t. the photon crossing any plane of choice along  $z$ ; a convenient choice which also allows using this time shift in conjunction with LTTE is the plane that contains the barycenter of the system,  $z_0$ . By making this choice, the resulting expression can be used in conjunction with classical LTTE which accounts for the shift due to the travel time between the barycenter and the observer. We can express the time,  $t_0$ , at which the photon crosses this  $z_0$  plane as follows:

$$t_0 = t_f - \frac{z_f(t_f) - z_0(t_0)}{c}. \quad (5.21)$$

To find the time of observed eclipse, we need to solve Equations (5.19-5.21) for  $t_0$ . If the functional dependence of  $v_{x,b}(t)$  and  $v_{x,f}(t)$  is known, this can be computed either analytically or numerically. For the purposes of deriving an approximate general analytic solution, let us examine the case where the x-velocities can be assumed constant throughout the travel time of the photon,  $[t_b, t_f]$ , thereby allowing us to simplify Equation (5.19) as follows:

$$(t_b - t_{\text{align}}) v_{x,b} = (t_f - t_{\text{align}}) v_{x,f}. \quad (5.22)$$

We can now use Equations (5.20-5.22) to solve for  $\Delta t_{\text{BATV}} \equiv t_0 - t_{\text{align}}$ , i.e. the time *shift*, relative to the time of geometric alignment, at which the photon emitted by one star, traveling along the line of sight, and then intercepted by another star, will pass the  $z_0$  plane:

$$\Delta t_{\text{BATV}} = \frac{z_f(t_f) - z_b(t_b)}{c} \frac{v_{x,b}}{v_{x,b} - v_{x,f}} - \frac{z_f(t_f) - z_0(t_0)}{c}. \quad (5.23)$$

If the z-positions of both stars and the barycenter are constant over the photon path time interval,  $[t_b, t_f]$ , such that  $z_f(t_f) = z_f(t_0)$  and  $z_b(t_b) = z_b(t_0)$ , then we can simplify Equation (5.23) by dropping all dependencies on time as follows:

$$\Delta t_{\text{BATV}} = \frac{\Delta z_{\text{bf}}}{c} \frac{v_{x,b}}{v_{x,b} - v_{x,f}} - \frac{\Delta z_{0f}}{c}, \quad (5.24)$$

where  $\Delta z_{\text{bf}} \equiv z_f - z_b$  and  $\Delta z_{0f} \equiv z_f - z_0$ . Note again that all values of  $\Delta z_{ij}$  and  $v_{x,i}$  may change between successive eclipses, but are assumed constant over the light travel time between the two stars at eclipse.

In order to determine the observed time of any individual eclipse, this effect, as well as any delay caused by a change in the distance between the observer and the barycenter (i.e. classical LTTE) must be taken into account:

$$t_{\text{obs}} = t_{\text{align}} + \Delta t_{\text{LTTE}} + \Delta t_{\text{BATV}}, \quad (5.25)$$

where  $t_{\text{align}}$  itself may need a dynamical correction for any perturbations to the orbital period or other elements (e.g. due to interactions with additional bodies in the system) from the value provided by a linear ephemeris:

$$t_{\text{align}} = t_{\text{ephem}} + \Delta t_{\text{dyn}}. \quad (5.26)$$

### 5.9.2 Application to Keplerian Orbits

In the case of a Keplerian binary system, we can further simplify by expressing the z-position of the barycenter,  $z_0$ , in terms of the mass-ratio of the binary. From the definition of the center of mass, we know that  $\Delta z_{0f} = \Delta z_{\text{bf}} / (\xi + 1)$  where  $\xi \equiv M_f/M_b$  is the mass-ratio,  $q$ , for a primary eclipse, or the inverse of the mass-ratio,  $1/q$ , for a secondary eclipse, giving:

$$\Delta t_{\text{BATV}} = \frac{\Delta z_{\text{bf}}}{c} \left( \frac{v_{x,b}}{v_{x,b} - v_{x,f}} - \frac{1}{\xi + 1} \right). \quad (5.27)$$

We can separate the external barycentric velocity (denoted with the ‘bary’ subscript) and orbital velocities relative to that same barycenter (denoted with the ‘orb’ subscript), and take advantage of the relationship that, for a Keplerian orbit,  $\xi = M_f/M_b = |\mathbf{v}_{b,\text{orb}}|/|\mathbf{v}_{f,\text{orb}}|$ . So, by substituting  $v_{x,f} = v_{x,f,\text{orb}} + v_{x,\text{bary}}$  and  $v_{x,b} = -\xi v_{x,f,\text{orb}} + v_{x,\text{bary}}$ , we get the following final expression for the time shift of an eclipse caused by BATV:

$$\Delta t_{\text{BATV}} = \frac{\Delta z_{\text{bf}}}{c} \left( \frac{\xi - 1}{\xi + 1} - \frac{1}{\xi + 1} \frac{v_{x,\text{bary}}}{v_{x,f,\text{orb}}} \right). \quad (5.28)$$

The orbital velocity ( $v_{x,f,\text{orb}}$ ) and separation ( $\Delta z_{\text{bf}}$ ) terms are provided as orbital elements in Appendix A.

In many cases, the shift in observed eclipse times is constant and can simply be absorbed by a time-offset in the entire light curve. However, if any of the above quantities vary with time, then this shift,  $\Delta t_{\text{BATV}}$ , also varies in time, resulting in a contribution to the ETVs.

### 5.9.3 Expected Contribution from GAIA Proper Motions

GAIA DR1 (Gaia Collaboration et al., 2016a,b; Lindegren et al., 2016) includes measured parallaxes and proper motions for  $\sim 2$  million sources also found in the Hipparcos and Tycho-2 catalogs. With approximately 1 billion total targets in GAIA, the number of sources with precisely determined proper motions can be expected to increase drastically in the near future. As BATV depends strongly on the transverse velocity of a system, GAIA will enable us to estimate the magnitude of BATV for most observed systems.

Unfortunately, proper motions alone are not enough, as BATV depends on these transverse velocities projected along the direction of motion of the eclipsed object on the sky. In some rare cases, this orientation of a given system on the sky may be constrained,

e.g. through direct imaging or astrometric solutions, but in most cases it will likely remain unknown.

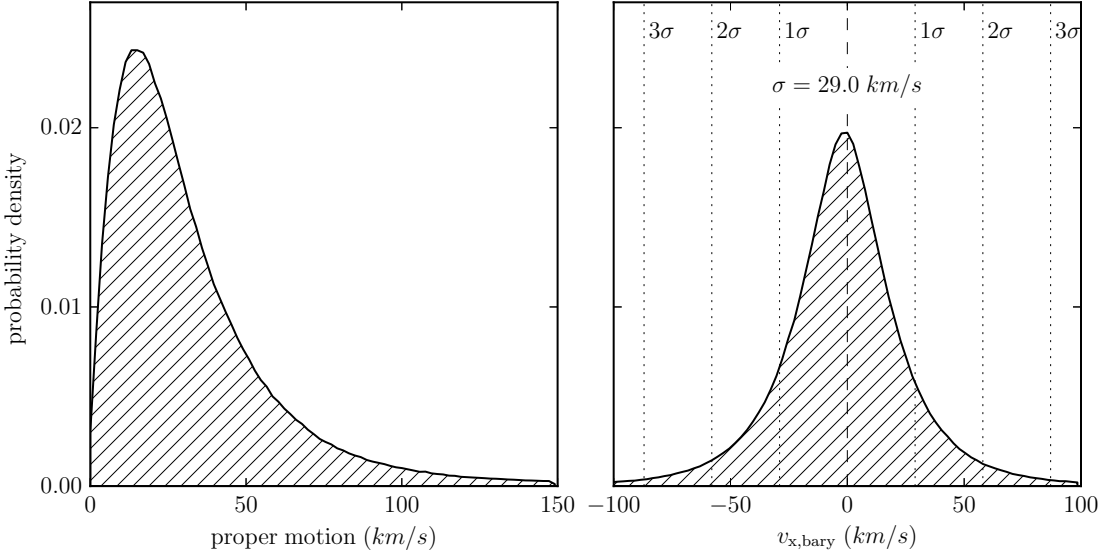


Figure 5.2 Left: the distribution of proper motions (in velocity units) computed from the GAIA DR1 (excluding the 3% of targets with proper motions above  $150 \text{ km s}^{-1}$ ). Right: the derived distribution in  $v_{x,\text{bary}}$ , where the velocity is determined from a randomized orientation of the binary on the sky relative to the proper motion. The standard deviation ( $29 \text{ km s}^{-1}$ ) and the corresponding confidence levels are shown with vertical dotted lines.

The existing proper motions from GAIA DR1, however, provide the expected distributions of the projected transverse velocity,  $v_{x,\text{bary}}$ . Figure 5.2 depicts the distribution of proper motions (in velocity units) computed directly from the GAIA parallaxes and proper motions as well as the distribution of projected transverse velocities, assuming a random distribution in orientations of binary systems on the sky. Excluding the 3% of sources with proper motions above  $150 \text{ km s}^{-1}$ , the expected projected transverse velocity is up to  $100 \text{ km s}^{-1}$ , with 68% ( $1\sigma$ ) falling between  $-29$  and  $+29 \text{ km s}^{-1}$ , 95% ( $2\sigma$ ) falling between  $-58$  and  $+58 \text{ km s}^{-1}$ , and 99.7% ( $3\sigma$ ) falling between  $-87$  and  $+87 \text{ km s}^{-1}$ . Although these proper motions alone will not allow for estimating the exact value of  $v_{x,\text{bary}}$  for a particular system, it does allow an estimate for a statistical range of values.

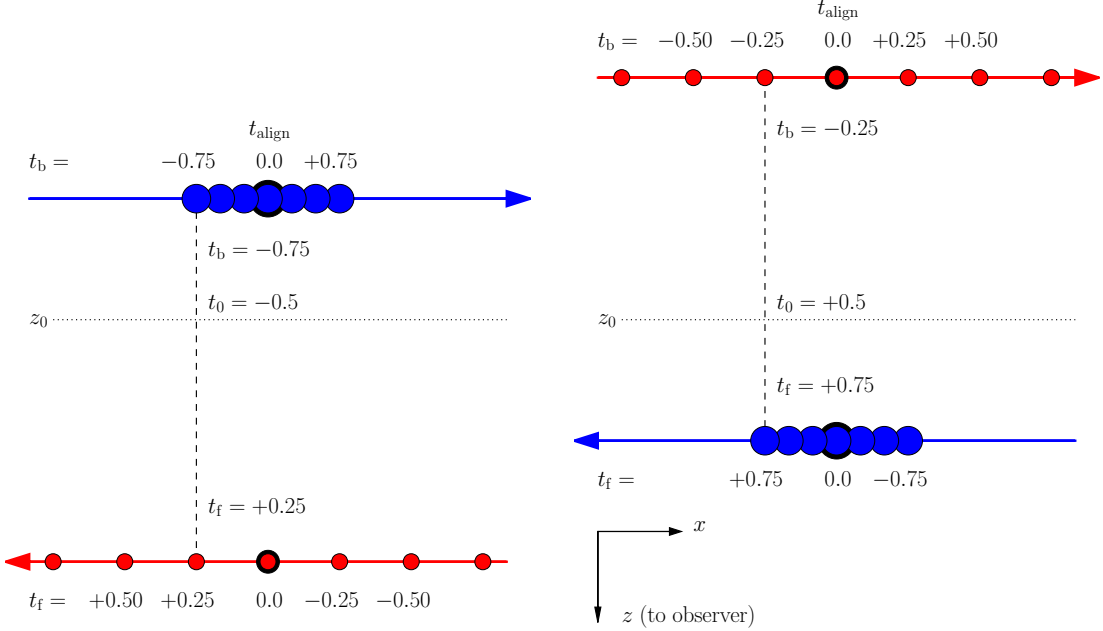


Figure 5.3 2D schematic representation showing how BATV with non-unity mass-ratio ( $q = 1/3$  in the case shown) affects the phase-separation between primary and secondary eclipses. Left: a primary eclipse ( $\xi \equiv q = 1/3$ ), with the more massive object (with a slower velocity and closer to the barycenter) being eclipsed. Right: a secondary eclipse ( $\xi \equiv 1/q = 3$ ) with the roles reversed. Since the observed time is measured with respect to the (fixed) barycenter, the primary and secondary eclipses are observed to be shifted with respect to each other.

#### 5.9.4 Constant Shift in Phase-Separation Between Eclipses

For a binary system with time-independent (or zero) barycentric transverse velocity, the observed times of the primary and secondary eclipses, relative to each other, can still be altered for a non-equal mass system due to both the asymmetric velocities and the distance from the barycenter during eclipse, as depicted schematically in Figure 5.3. This same effect, for the case without barycentric velocity, was discussed in §5.6 (see also Kaplan 2010 and Fabrycky 2010).

We can express the magnitude of this effect as the difference between the time shifts for the primary and secondary eclipses,  $t_{\text{pri}}$  and  $t_{\text{sec}}$ , divided by the orbital period,  $P$ , used for phasing. This resulting  $\Delta\Phi_{\text{sep}, \text{BATV}}$  will be the observed change in phase-separation between the primary and secondary eclipses as compared to the expected value (i.e. 0.5 for

a circular system, assuming  $c \rightarrow \infty$ ).

Here we make the assumption that  $\Delta z_{\text{bf}}$  (provided in terms of orbital elements in Appendix A) is constant between successive eclipses of the same type, but not between primary and secondary eclipses for non-zero eccentricity. For simplicity, we will allow  $v_{x,\text{bary}}$  to be non-zero, but assume it to be constant in time (including between primary and secondary eclipses).

We will use Equation (5.28) and alternate the roles of the eclipsed and eclipsing stars, as necessary, using indices 1 and 2 to represent the primary and secondary stars, respectively.

$$\begin{aligned} \Delta\Phi_{\text{sep, BATV}} = & \frac{1}{Pc} \left[ \Delta z_{12}(t_{\text{sec}}) \left( \frac{1/q - 1}{1/q + 1} - \frac{1}{1/q + 1} \frac{v_{x,\text{bary}}}{v_{x,1,\text{orb}}(t_{\text{sec}})} \right) \right. \\ & \left. - \Delta z_{21}(t_{\text{pri}}) \left( \frac{q - 1}{q + 1} - \frac{1}{q + 1} \frac{v_{x,\text{bary}}}{v_{x,2,\text{orb}}(t_{\text{pri}})} \right) \right], \end{aligned} \quad (5.29)$$

where  $\Delta z_{12}$  and  $v_{x,*,\text{orb}}$  can be found in terms of orbital elements in Appendix A.

We can make a few additional simplifications by examining the circular case. Here, the separation between the two stars remains constant throughout the orbit, so  $\Delta z_{12}(t_{\text{sec}}) = \Delta z_{21}(t_{\text{pri}}) = a \sin i$ . Additionally, the velocity of a given star is constant throughout the orbit, so the velocities in the x-direction are the same at primary and secondary eclipses, and therefore  $v_{x,2,\text{orb}} \equiv v_{x,2,\text{orb}}(t_{\text{pri}}) = v_{x,2,\text{orb}}(t_{\text{sec}})$  and  $v_{x,1,\text{orb}} \equiv v_{x,1,\text{orb}}(t_{\text{pri}}) = v_{x,1,\text{orb}}(t_{\text{sec}})$ . This then also allows us to use the mass-ratio to relate velocities via  $v_{x,1,\text{orb}} = -qv_{x,2,\text{orb}}$ :

$$\Delta\Phi_{\text{sep, BATV}} = \frac{2a \sin i}{Pc} \left( \frac{1-q}{1+q} + \frac{1}{1+q} \frac{v_{x,\text{bary}}}{v_{x,2,\text{orb}}} \right). \quad (5.30)$$

We then represent  $v_{x,2,\text{orb}}$  in terms of orbital elements (again, assuming the circular case, see Appendix A for  $v_{x,2,\text{orb}}$  in the general, eccentric, case):

$$v_{x,2,\text{orb}}(e=0) = \sqrt{\frac{GM_{\text{tot}}}{a}} \frac{1}{1+q}. \quad (5.31)$$

Then by using Kepler's third law, we can write the entire expression for the offset in

phase-separation for the circular case in terms of  $v_{x,\text{bary}}$ ,  $q$ ,  $i$ ,  $M_{\text{tot}}$ , and  $a$ :

$$\Delta\Phi_{\text{sep, BATV}} = \left( \frac{GM_{\text{tot}}}{\pi^2 a} \right)^{1/2} \frac{\sin i}{c} \left[ \frac{1-q}{1+q} + v_{x,\text{bary}} \left( \frac{a}{GM_{\text{tot}}} \right)^{1/2} \right], \quad (5.32)$$

or in terms of  $v_{x,\text{bary}}$ ,  $q$ ,  $i$ ,  $M_{\text{tot}}$ , and  $P$ :

$$\Delta\Phi_{\text{sep, BATV}} = \left( \frac{2GM_{\text{tot}}}{\pi^2 P} \right)^{1/3} \frac{\sin i}{c} \left[ \frac{1-q}{1+q} + v_{x,\text{bary}} \left( \frac{P}{2\pi GM_{\text{tot}}} \right)^{1/3} \right]. \quad (5.33)$$

Figure 5.4 shows the magnitude of this shift from 0.5-phase separation for a circular binary with a period of 1.0 days converted to time units. The magnitude increases as the mass-ratio becomes more extreme and as the total mass of the system increases. For equal mass binaries with a period of 1 day, the shift caused by BATV is  $\sim 1$  s. However, for smaller mass ratios, the shift can reach  $\sim 30$  s, which is easily observable with precision photometry.

For hot-Jupiters around fairly high-mass stars, for example, if an occultation can be observed and used to constrain the eccentricity, it is important to account for BATV in

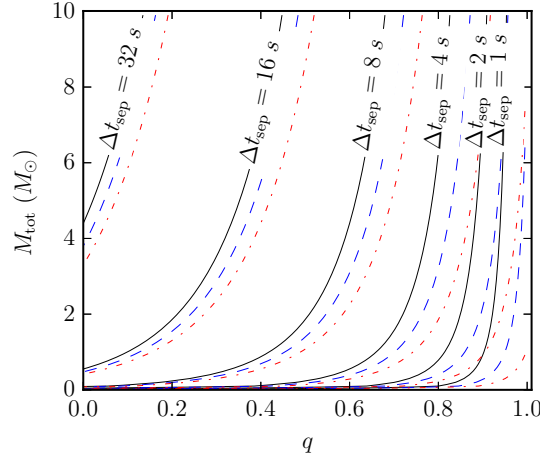


Figure 5.4 Change in eclipse separation (from the expected 0.5-phase) caused by BATV for a circular  $i = 90^\circ$  binary with a period of 1.0 d as a function of the total mass and mass-ratio shown in solid black for  $v_{x,\text{bary}}/v_{x,\text{f,orb,peri}} = 0\%$ , dashed blue for 5%, and dash-dotted red for 10%.

order to avoid misconstruing a phase-separation as non-zero eccentricity. It can also be important to account for a conservative uncertainty in the value of  $v_{x,\text{bary}}$  and its influence on the phase-separation when determining measured uncertainties on the eccentricity or  $e \cos \omega$ . KELT-9b (Gaudi et al., 2017, Collins et al., in preparation), for instance, is a detected planet system which is particularly susceptible to BATV as it has a small mass-ratio of  $q = 0.0011$  and a fairly large total mass of  $M_{\text{tot}} = 2.5 M_{\odot}$ . Although the system is not known to be exactly circular, it is expected to have been significantly circularized due to its short orbital period of  $P = 1.48$  d. Figure 5.5 shows the expected time-shift of the secondary eclipse relative to the expected value as a function of  $v_{x,\text{bary}}$ . For a reasonable range of transverse velocities adopted from the  $3\sigma$  distribution from GAIA (see Figure 5.2), this shift could be anywhere from  $\sim 20$  to  $\sim 45$  seconds. As the eccentricity of this system is not well-constrained, there will be a degeneracy in the contribution to this shift between BATV and a small, but non-zero, eccentricity. With individual eclipses timed to a precision of  $\sim 10$  s (Collins et al., in preparation, private communication), the effect of BATV on the resulting uncertainties on  $e \cos \omega$  could be to the same order as the effect of these timing uncertainties.

The above equations (5.29 for the general, eccentric, case and 5.32 or 5.33 when known to be circular) provide a more robust estimate of the phase-separation and therefore could be used in a similar matter to that of Kaplan (2010) (discussed in §5.6) to provide constraints on the mass-ratio. In practice, unless within a higher-order system,  $v_{x,\text{bary}}$  will likely be unknown, in which case reasonable limits, or constraints adopted from GAIA proper motions, could be applied to estimate the resulting uncertainty on the mass ratio.

### 5.9.5 Eccentric Systems with Apsidal Motion

In the case of apsidal motion, the distance between the two components,  $\Delta z_{\text{bf}}$ , at a given eclipse (i.e. primary or secondary) ranges throughout the entire precession cycle from  $a(1 - e) \sin i$  when the eclipse occurs at periastron to  $a(1 + e) \sin i$  at apastron. In addition,

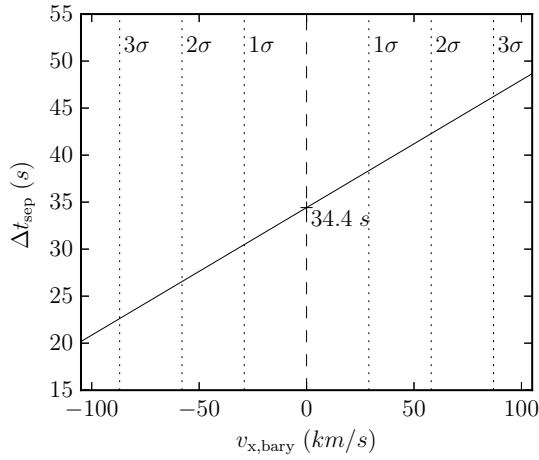


Figure 5.5 Change in transit separation (from the expected 0.5-phase, assuming a circular orbit), caused by BATV for KELT-9b as a function of  $v_{x,\text{bary}}$ . With no barycentric transverse motion, the secondary event can still be expected to show a shift of 34.4 s due to its small mass ratio. Black dotted vertical lines show the estimates for the distribution of  $v_{x,\text{bary}}$  from GAIA for different confidence levels (see Figure 5.2). At  $3\sigma$ , 99.7 % of objects will be influenced by the barycentric term of BATV by up to  $\pm 12$  s.

the velocity of the front star varies from  $v_{f,\text{orb},\text{peri}}$  at periastron to  $v_{f,\text{orb},\text{peri}}(1-e)/(1+e)$  at apastron. As both the separation and velocities are time-dependent, the effect caused by the asymmetric velocities will also vary in time. We can therefore determine the maximum peak-to-peak amplitude of this effect,  $A_{\text{BATV}}$ , over the whole apsidal motion cycle as the difference between Equation (5.28) expressed at periastron and apastron:

$$A_{\text{BATV}} = \left| \frac{2ea \sin i}{c} \left( \frac{\xi - 1}{\xi + 1} - \frac{2}{\xi + 1} \frac{v_{x,\text{bary}}}{v_{x,f,\text{orb},\text{peri}}} \right) \right|. \quad (5.34)$$

Equation (5.34) is plotted in Figure 5.6 for several values of  $v_{x,\text{bary}}/v_{x,f,\text{orb},\text{peri}}$  along with several known apsidal motion cases, whose adopted parameters are listed in Table 5.1. The parameter space in which this effect is maximized (i.e. small mass-ratio, large eccentricity, large semi-major axis) also minimizes the chance of observing and detecting the eclipses. Largely because of this, most known apsidal motion binaries have fairly small contributions when assuming no barycentric transverse velocity. However, it is not implausible to imagine a system being observed in which it is necessary to account for BATV

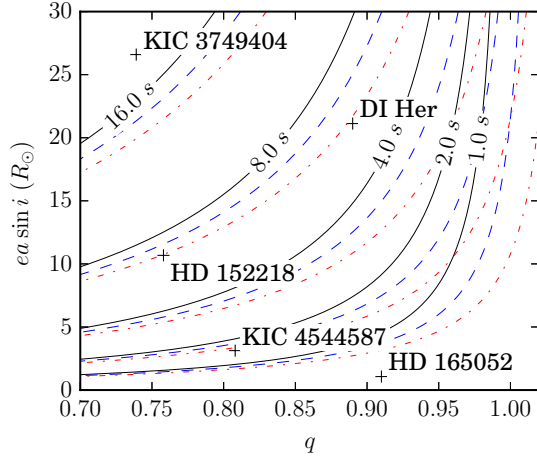


Figure 5.6 Peak-to-peak BATV amplitude (for primary eclipses,  $\xi \equiv q$ ) over an entire apsidal motion cycle as a function of eccentricity ( $e$ ) times projected semi-major axis ( $a \sin i$ ) and mass ratio ( $q$ ) shown in solid black for  $v_{x,\text{bary}}/v_{x,\text{f,orb,peri}} = 0\%$ , dashed blue for 1%, and dot-dashed red for 2%. Also included are several known apsidal motion systems, whose adopted values and citations are provided in Table 5.1.

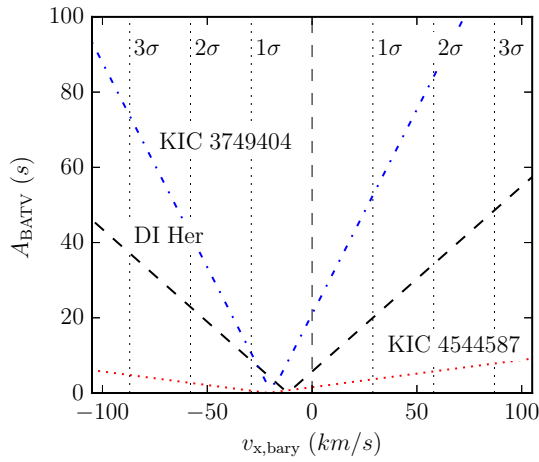


Figure 5.7 Peak-to-peak BATV amplitude (for primary eclipses,  $\xi \equiv q$ ) over an entire apsidal motion cycle for several known apsidal motion systems as a function of the bulk transverse velocity,  $v_{x,\text{bary}}$ . DI Her is shown in dashed black, KIC 3749404 in dot-dashed blue, and KIC 4544587 in dotted red. Black dotted vertical lines show the estimates for the distribution of  $v_{x,\text{bary}}$  from GAIA for different confidence levels (see Figure 5.2).

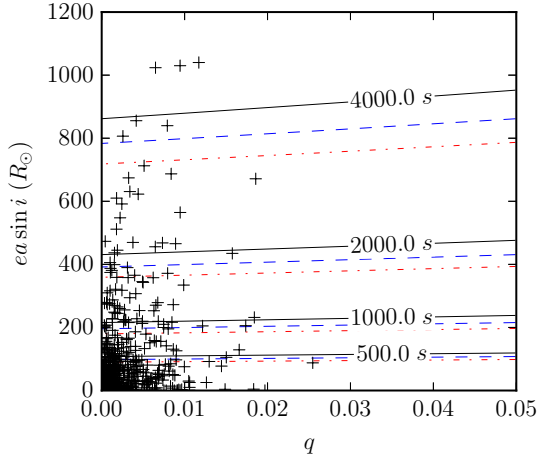


Figure 5.8 Same as Figure 5.6 but extended to low mass-ratios for planets. Shown are the peak-to-peak BATV amplitudes (for transits) over an entire apsidal motion cycle as a function of eccentricity ( $e$ ) times projected semi-major axis ( $a \sin i$ ) and mass ratio ( $q$ ) for all confirmed *Kepler* exoplanets. The contours are shown in solid black for  $v_{x,\text{bary}}/v_{x,f,\text{orb},\text{peri}} = 0\%$ , dashed blue for 5%, and dot-dashed red for 10%. Note that these are not necessarily known to exhibit apsidal motion, but do represent the parameter space of known exoplanets.

in order to accurately determine the true precession rate, particularly as missions such as GAIA begin to give us constraints on the barycentric transverse velocities of these systems. This will require a fairly long baseline, as all cases listed in Table 5.1 have contributions from BATV below 0.1 seconds per day (even with conservative estimates on  $v_{x,\text{bary}}$ , see Figure 5.7).

Figure 5.7 shows this same amplitude for these apsidal motion binaries as a function of  $v_{x,\text{bary}}$  by computing  $v_{x,f,\text{orb},\text{peri}}$  for each binary using the total mass,  $M_{\text{tot}}$ , adopted from the literature as listed in Table 5.1. Note that even for no barycentric transverse velocity, the finite speed of light still requires a corrective term to apsidal motion for non equal-mass systems. Barycentric transverse motion does, however, contribute significantly even at relatively low velocities. Also note that since  $\xi < 1$  for all of these cases (see footnote in Table 5.1), the two terms in Equation (5.34) are opposite in sign for small negative barycentric velocities, therefore decreasing the amplitude of the effect until the second term eventually dominates (see Figure 5.7). Once these transverse velocities are known,

Table 5.1. Adopted values and computed amplitudes for known apsidal motion binaries

System	$e$	$a \sin i$ ( $R_\odot$ )	$q$	$M_{\text{tot}}$ ( $M_\odot$ )	$P_{\text{apsidal}}$ ( $d$ )	$A_{\text{BATV}}$ ( $s$ )
DI Herculis	0.489	43.2	0.89	9.7	55400	5.7
HD 152218*	0.269	39.7	0.76 <sup>†</sup>	... <sup>‡</sup>	176	6.8
HD 165052*	0.090	11.9	0.91	... <sup>‡</sup>	30	0.2
KIC 3749404	0.659	40.4	0.74	3.1	309	18.5
KIC 4544587	0.288	10.8	0.81	3.6	182	1.5

\*spectroscopic binary - may not eclipse.

<sup>†</sup>reported as  $q = 1.32$  in Rauw et al. (2016).

<sup>‡</sup>not included as only  $M_{\text{tot}} \sin^3 i$  is known.

Note. — All values except BATV amplitudes are either directly or computed from values in the literature (Guinan and Maloney (1985) for DI Herculis, Rauw et al. (2016) for HD 152218, Ferrero et al. (2013) for HD 165052, Hambleton et al. (2016) for KIC 3749404, and Hambleton et al. (2013) for KIC 4544587). All reported transverse amplitudes are computed for  $v_{x,\text{bary}} = 0$ . See Figures 5.6 and 5.7 to see the dependence of these values on the barycentric transverse velocity.

BATV may then become a significant contribution for some systems.

In the case of exoplanets, the mass-ratio will be small, resulting in a large contribution even when the size of the orbit is small. Figure 5.8 shows the same as Figure 5.6, but for the parameter space of known *Kepler* exoplanets. Note that these are not necessarily known apsidal motion cases, but the figure does exhibit that BATV can be quite significant for any exoplanet exhibiting precession.

### 5.9.6 Binary System with Change in Inclination

There are several known cases in which the inclination of an eclipsing system changes quickly enough to cause an observable change in the depth of the eclipse, including AY Mus

(Soderhjelm, 1974), V907 Sco (Lacy et al., 1999), SS Lac (Torres, 2001), and a number of systems in the Magellanic Clouds (Juryšek et al., 2017). In some of these cases, this change in inclination is so extreme that eclipse can be seen to begin or cease entirely. A change in inclination can be due to any external forces on the system, including the presence of any additional bodies in the system causing dynamical effects, including Kozai cycles (Kozai, 1962; Mazeh and Shaham, 1979). Note that these dynamical effects may also cause perturbations to other orbital elements which could result in additional contributions to the shape and timing of eclipses.

Similar to the apsidal motion case, a change in inclination also results in a change in the projected separation of the two stars between successive eclipses, but the velocities at eclipse remain fixed. In this case, the separation at eclipse will vary from  $s_{\text{ecl}} \equiv \Delta z_{\text{bf}}(i = 90^\circ)$  to  $\Delta z_{\text{bf}}(i = 0^\circ) = 0$ . However, as eclipse times are only measurable when eclipses are still present, the maximum observed amplitude will only occur between some critical inclination,  $i_{\text{crit}}$ , and  $90^\circ$ .

This critical inclination can be approximated geometrically as follows:

$$i_{\text{crit}} = \cos^{-1} \left( \frac{R_f + R_b}{s_{\text{ecl}}} \right), \quad (5.35)$$

where  $R_f$  and  $R_b$  are the radii of the front and back stars, respectively, and  $s_{\text{ecl}}$  is the (non-projected) distance between the two components at eclipse (i.e.  $a$  for circular binaries).

Therefore the observable effect can be approximated by:

$$A_{\text{BATV}} = \left| \left[ 1 - \sqrt{1 - \left( \frac{R_f + R_b}{s_{\text{ecl}}} \right)^2} \right] \frac{s_{\text{ecl}}}{c} \left( \frac{\xi - 1}{\xi + 1} - \frac{1}{\xi + 1} \frac{v_{x,\text{bary}}}{v_{x,f,\text{orb}}} \right) \right|. \quad (5.36)$$

The expression above is plotted in Figure 5.9 for the case where  $R_f + R_b = 2R_\odot$ , showing that, for a binary with a change in inclination, BATV can have a measurable contribution to the ETVs on the order of seconds, with any barycentric transverse velocity potentially

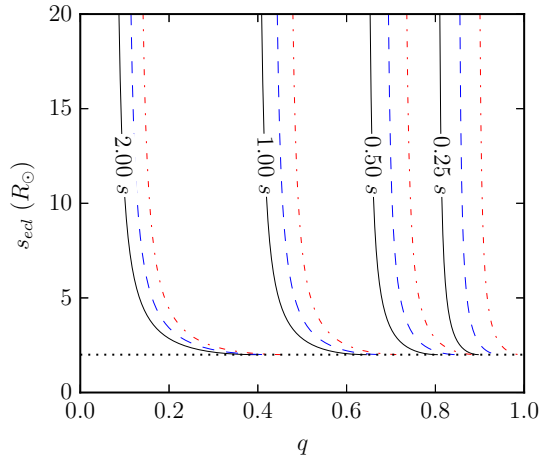


Figure 5.9 BATV amplitude (for primary eclipses,  $\xi \equiv q$ ) over a change in inclination from  $i_{\text{crit}}$  to  $90^\circ$  as a function of the mass-ratio ( $q$ ) and the separation between two components at eclipse ( $s_{\text{ecl}}$ ) for a system in which the sum of radii is  $R_f + R_b = 2R_\odot$ . The contours are in solid black for  $v_{x,\text{bary}}/v_{x,\text{orb}} = 0\%$ , dashed blue for 5%, and dot-dashed red for 10%. The dashed black line at  $s_{\text{ecl}} = 2R_\odot$  represents the limit at which the two stars will be in contact.

increasing the magnitude of the effect. As was the case for apsidal motion,  $\xi < 1$  will result in opposing signs for the two terms on the right in Equation (5.36), and therefore a small negative  $v_{x,\text{bary}}$  will actually decrease the overall amplitude before eventually dominating.

### 5.9.7 Hierarchical Triple Systems

For a hierarchical triple system in which a third star is in orbit with an inner-binary system, the barycentric transverse velocity of the inner-binary system varies in time throughout the period of the outer-orbit, resulting in a cyclical contribution to the ETVs of the inner-binary caused by BATV.

Here  $v_{x,\text{bary}}$  in Equation (5.28) becomes the transverse velocity of the barycenter of the inner-binary caused by its orbit about the barycenter of the entire triple system and  $v_{x,f,\text{orb}}$  is the velocity of the eclipsing star caused by the inner-orbit alone, projected along the instantaneous direction of  $v_{x,\text{bary}}$  (by definition of the x-direction). As we know the barycenter of the inner-binary is moving in the z-direction throughout the outer-orbit, the

assumptions in Equation (5.28) can no longer be assumed. Note though that the z-velocity of the inner-binary is minimized as the contribution from BATV is maximized, and vice versa. Nevertheless, these assumptions should be dropped and a numerical method or the should be used to determine precise times of observed eclipse as a function of time. These equations, along with the orbital elements provided in Appendix A, can still be particularly useful in conjunction with classical LTTE and dynamical equations to fit orbital elements of the outer-orbit to observed ETVs of an inner eclipsing binary prior to completing a full dynamical model with light time delay.

For simplicity, to compare the contribution to the ETVs of BATV to both LTTE and dynamical effects, we'll examine the case of a hierarchical triple system in which both orbits are circular and share the same plane (i.e.  $i_{\text{in}} = i_{\text{out}}$  and  $\Omega_{\text{in}} = \Omega_{\text{out}}$ ). Coplanar orbits maximize the contribution of BATV as the barycentric transverse velocity caused by the motion around the center-of-mass of the entire system is most aligned with the velocity of the stars in the inner-binary at eclipse. We derive the circular case using the following conditions:

$$\begin{aligned}\Delta z_{\text{bf}}(e_{\text{in}} = 0) &= a_{\text{in}} \sin i_{\text{in}}, \\ v_{x,\text{f,orb}}(e_{\text{in}} = 0, \text{eclipse}) &= \sqrt{\frac{GM_{12}}{a_{\text{in}}}} \frac{1}{1 + \xi_{\text{in}}}, \text{ and} \\ v_{x,\text{bary}}(e_{\text{out}} = 0) &= \cos(v_{12}) \sqrt{\frac{GM_{123}}{a_{\text{out}}}} \frac{q_{\text{out}}}{1 + q_{\text{out}}},\end{aligned}\quad (5.37)$$

where the subscript “in” represents the inner-orbit and “out” the outer-orbit in which the inner-binary is the primary component ( $q_{\text{out}} \equiv M_3/M_{12}$ ) and is treated as a point mass at its own barycenter.  $v_{12}$  is then the true anomaly of the inner binary within the outer-orbit.

Substituting these into Equation (5.28), we can get the contribution of BATV through-

out the outer-orbit as a function of the mass-ratios and semi-major axes:

$$\Delta t_{\text{BATV}}(e = 0, \text{coplanar}) = \frac{a_{\text{in}} \sin i_{\text{in}}}{c} \left[ \frac{\xi_{\text{in}} - 1}{\xi_{\text{in}} + 1} \pm \cos(v_{12}) \left( \frac{a_{\text{in}}}{a_{\text{out}}} \right)^{1/2} \frac{q_{\text{out}}}{(1 + q_{\text{out}})^{1/2}} \right], \quad (5.38)$$

where the sign on the second term is positive for a prograde orbit and negative for a retrograde orbit.

The cosine term above varies in sign as  $v_{x,\text{bary}}$  flips direction throughout the outer-orbit. The peak-to-peak amplitude is therefore the difference between this expression taken while the inner binary is in the front and back of the outer-orbit, i.e.  $\Delta t_{\text{BATV}}(v_{12} = 0) - \Delta t_{\text{BATV}}(v_{12} = \pi)$ . Since the extrema used in the amplitude are taken at points along the outer-orbit in which the inner-binary is not moving in the z-direction, this amplitude can safely be determined without the need for numerical computations. As only the second term is time-dependent, the peak-to-peak amplitude does not depend on  $\xi_{\text{in}}$ :

$$A_{\text{BATV}}(e = 0, \text{coplanar}) = \pm 2 \frac{a_{\text{in}} \sin i_{\text{in}}}{c} \left( \frac{a_{\text{in}}}{a_{\text{out}}} \right)^{1/2} \frac{q_{\text{out}}}{(1 + q_{\text{out}})^{1/2}}. \quad (5.39)$$

### 5.9.8 Comparison of Contributions of Effects

Classical LTTE (see §5.7) for the same circular, coplanar, case will contribute peak-to-peak ETVs equivalent to the photon travel time across the outer orbit:

$$A_{\text{LTTE}}(e = 0) = 2 \frac{a_{\text{out}} \sin i_{\text{out}}}{c} \frac{q_{\text{out}}}{1 + q_{\text{out}}}. \quad (5.40)$$

Since we are exploring the coplanar case, we can set  $i_{\text{out}} = i_{\text{in}}$ , and can therefore approximate the ratio between the BATV and LTTE contributions to the ETVs as follows:

$$\frac{A_{\text{BATV}}(e = 0, \text{coplanar})}{A_{\text{LTTE}}(e = 0)} = \pm \left( \frac{a_{\text{in}}}{a_{\text{out}}} \right)^{3/2} (1 + q_{\text{out}})^{1/2}. \quad (5.41)$$

Figure 5.10 shows the magnitude of BATV for circular, coplanar, hierarchical orbits.

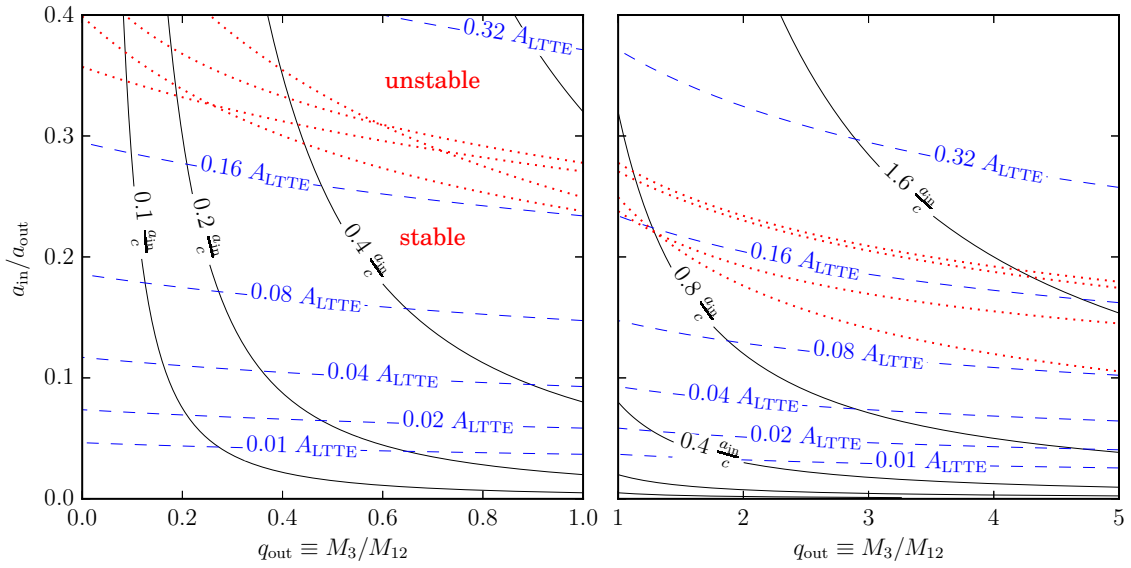


Figure 5.10 Peak-to-peak amplitude of BATV over an entire orbit of the inner-binary within the outer-binary for the circular and coplanar case, viewed edge-on at  $i = 90^\circ$ . The left shows  $q_{\text{out}} < 1$  while the right shows  $1 < q_{\text{out}} < 5$ . The solid black contours are in terms of the photon travel time between the two eclipsing components in the inner-binary,  $a_{\text{in}}/c$ , from Equation (5.39) and the dashed blue contours are in terms of the ratio of the amplitude as compared to classical LTTE,  $A_{\text{LTTE}}$ , from Equation (5.41). The red dotted lines represent the estimated stability limits, for  $q_{\text{in}} = 1$ , according to Harrington (1972), Bailyn (1987), Eggleton and Kiseleva (1995), and Mardling and Aarseth (2001) as compiled by Mikkola (2008).

This effect is maximized as  $q_{\text{out}} \rightarrow \infty$  (so that the inner-binary's velocity through space is increased) and as  $a_{\text{in}} \rightarrow a_{\text{out}}$  (the more tightly packed the system is, the larger the ratio between barycentric and orbital transverse velocity for the inner-binary). Also depicted in Figure 5.10 are various estimates for the stability limit of hierarchical triple systems according to Harrington (1972), Bailyn (1987), Eggleton and Kiseleva (1995), and Mardling and Aarseth (2001) as compiled and summarized by Mikkola (2008). Generally speaking, in the most extreme but still stable scenarios, it is possible for BATV to contribute  $\approx 15 - 20\%$  that of classical LTTE. In the most stable hierarchical systems, however, it is likely that the contribution from BATV will be under 1% that of LTTE.

Nevertheless, without properly accounting for BATV, fitting the LTTE contribution of ETV observations would result in an incorrect measurement of the amplitude of the timing variations caused by LTTE. Since  $A_{\text{LTTE}} \propto P_{\text{out}}^{2/3} \left( m_3 / m_{123}^{2/3} \right)$ , this will result in an overestimate or underestimate in the mass-ratio (and therefore mass of the third body) for prograde and retrograde orbits, respectively (see Figure 5.11).

Figure 5.11 also compares the analytical approximation for LTTE and BATV in Equation 5.38 (assuming nested Keplerian orbits) to the exact numerical solution. The residuals in the case shown are on the order of 1% the amplitude of the BATV contribution and are caused by the approximations used: that the barycenter of the inner-binary does not move in the z-direction and that the eclipsing stars travel in constant and straight trajectories during the photon travel time. When the systematic residuals due to these approximations prove too significant to neglect, Equations (5.19-5.21) can be solved iteratively in conjunction with the relevant equations of motion. Provided that  $\vec{r}_b(t)$ ,  $\vec{r}_f(t)$ , and  $\vec{r}_{\text{bc}}(t)$  can be computed, the scheme is as follows:

- pick a timestamp  $t_b$  (e.g.  $t_{\text{align}}$ ) and compute  $\vec{r}_b(t_b)$ ;
- solve Equation (5.19) for  $t_f$ ; in most cases this needs to be done iteratively, i.e. by employing a Newton-Raphson method;

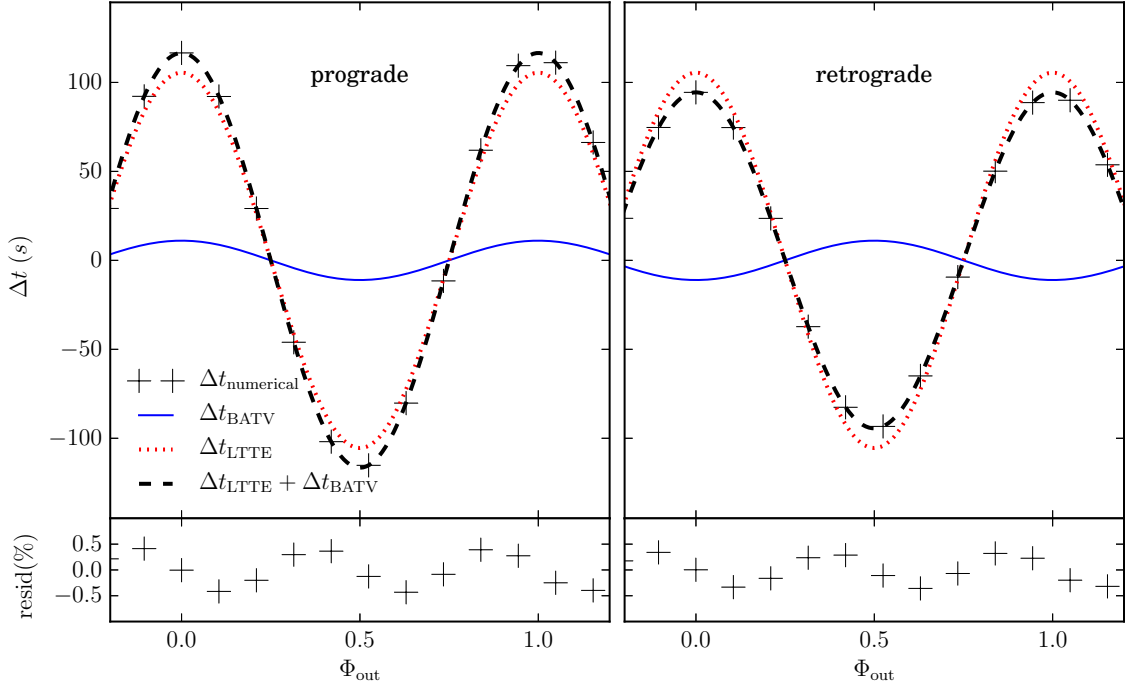


Figure 5.11 Contribution to ETVs by both classical LTTE and the BATV effect for a circular coplanar hierarchical triple, for the case where  $q_{\text{out}} = 10$  and  $a_{\text{in}}/a_{\text{out}} = 0.1$ . On the left is the prograde case, showing an increase in the overall magnitude of the ETVs, whereas the right shows the retrograde case with a decrease in the magnitude. The expressions are plotted here as a continuous function of  $\Phi_{\text{out}}$  but note that they are only applicable at times at which an eclipse of the inner-binary occurs, shown as black +s for the numerical solution. The residuals between the exact numerical solution and the analytic expression (due to the stated approximations) are shown in the lower panel, reaching up to 0.5% of  $A_{\text{BATV}}$ .

- given  $t_f$ , compute  $\vec{r}_f(t_f)$ ;
- given  $\vec{r}_b(t_b)$  and  $\vec{r}_f(t_f)$ , calculate the difference between both sides of Equation (5.20),
$$\Delta = t_f - t_b - [z_f(t_f) - z_b(t_b)]/c;$$
- iterate the scheme over  $t_b$  until  $\Delta \rightarrow 0$  to a required level of precision;
- given  $t_f$  and  $\vec{r}_{bc}(t_0)$ , solve iteratively for  $t_0$  using Equation (5.21).

Similarly to BATV, dynamical effects (see §5.4) increase as the triple system becomes more tightly packed, and therefore also maximize their contribution to the ETVs. The amplitude of this effect can be approximated (see Mayer, 1990; Borkovits et al., 2003,

2011; Rappaport et al., 2013) as:

$$\begin{aligned} A_{\text{dyn}} &= \frac{3}{8\pi} \frac{M_3}{M_{123}} \frac{P_{\text{in}}^2}{P_{\text{out}}} (1 - e^2)^{-3/2} \\ &= \frac{3}{4} G^{-1/2} q_{\text{out}} a_{\text{in}}^3 a_{\text{out}}^{-3/2} M_{123}^{-1/2} (1 - e^2)^{-3/2}. \end{aligned} \quad (5.42)$$

We can then determine the ratio between BATV and dynamical contributions to the ETVs for the circular, coplanar, edge-on case:

$$\frac{A_{\text{BATV}}(e = 0, i = 90^\circ, \text{coplanar})}{A_{\text{dyn}}(e = 0)} = \frac{8}{3} \frac{G^{1/2}}{c} a_{\text{in}}^{-3/2} a_{\text{out}} M_{12}^{1/2}. \quad (5.43)$$

Note that, unlike for LTTE, this ratio does not depend on  $q_{\text{out}}$  but instead on the total mass of the inner binary,  $M_{12}$ . Figure 5.12 shows this ratio with  $a_{\text{out}}$  at the mean stability limit from Harrington (1972), Bailyn (1987), Eggleton and Kiseleva (1995), and Mardling and Aarseth (2001), assuming  $e_{\text{in}} = 0$ ,  $e_{\text{out}} = 0$ , and  $q_{\text{in}} = 1$  (Figure 5.10 shows the discrepancy between these models and the relation with  $q_{\text{in}}$ ). As this ratio (Equation 5.43) scales linearly with  $a_{\text{out}}$ , the contribution from BATV relative to dynamical effects will increase for increasingly stable systems.

For any system, it is likely that either LTTE or dynamical effects will dominate over BATV (see Figure 7 in Rappaport et al. (2013) for a comparison between  $A_{\text{LTTE}}$  and  $A_{\text{dyn}}$  as a function of  $P_{\text{out}}$ ). However, it may still be necessary to account for BATV in order to achieve accurate and precise determinations on the system parameters.

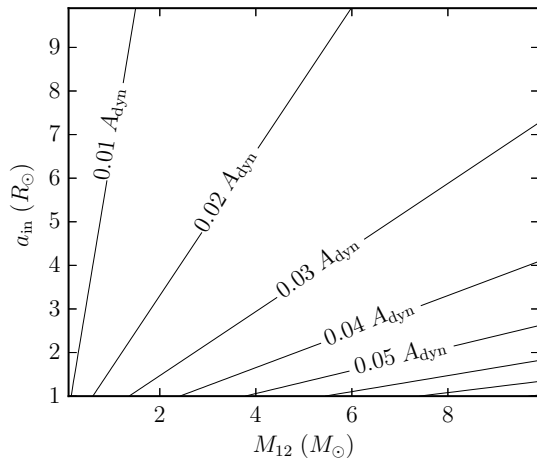


Figure 5.12 Contribution of the peak-to-peak amplitude of BATV as compared to  $A_{\text{dyn}}$  for the circular coplanar case in which  $a_{\text{out}}$  is fixed to be at the mean stability limit (see text for more details). Increasing  $a_{\text{out}}$  (i.e. increasing the stability of the system) will increase this relative contribution linearly.

## Chapter 6

### Robust Modeling of Stellar Triples

*This chapter includes excerpts and figures adapted from Conroy et al. in preparation,  
to be submitted to The Astrophysical Journal Supplement Series.*

For the most part, the underlying infrastructure that is applied to binaries (discretization of surfaces, treatment of atmospheres, limb-darkening, reflection, doppler boosting, etc), presented in §3 and Prša et al. (2016), is easily extended to higher-order systems. These details are not repeated here except when additional considerations need to be made for these higher-order systems.

Two main limitations of the binary implementation, however, need to be redesigned to handle multiple systems: Keplerian dynamics and Roche distortions. Although using Keplerian dynamics by nesting hierarchical orbits (i.e. so that the inner binary is treated as a point mass to a companion object) may be sufficient for truly hierarchical systems, this does not hold for the general case. Instead, in addition to support for nested Keplerian orbits, we also include a full N-body dynamical treatment of all masses in the system within PHOEBE 2. Unfortunately, as the Roche model for stellar distortion is parameterized via Keplerian orbital elements (mass ratio  $q$ , synchronicity parameter  $F$ , separation in units of the semi-major axis  $\delta$ , and the equipotential of the surface  $\Omega$ ), it can no longer be directly utilized when switching to N-body dynamics. We describe below the hybrid approach implemented within PHOEBE 2 for determining the equipotentials used for the distortion of each stellar surface while still using N-body dynamics. A similar, independent approach “merging” WD (Wilson and Devinney, 1971) along with a Burlisch-Stoer N-body implementation within the SWIFT package (Levison and Duncan, 1994) is discussed by Brož (2017).

## 6.1 Defining the System Hierarchy

Before any dynamics or surface distortion can be determined, the system first needs to be defined in a self-consistent manner. Conventionally, a binary system orbit is defined by the mass ratio  $q$ , semi-major axis  $a$ , eccentricity  $e$ , and period  $P$  (along with other “orientation” parameters such as inclination, argument of periastron, and longitude of the ascending node) with the masses then being uniquely determined through Kepler’s third law.

For a triple system, we can use the same parametrization by defining “nested” (i.e. “inner” and “outer”) orbits. The resulting six parameters ( $q_{\text{inner}}$ ,  $q_{\text{outer}}$ ,  $a_{\text{inner}}$ ,  $a_{\text{outer}}$ ,  $P_{\text{inner}}$ ,  $P_{\text{outer}}$ ; see Figure 6.1 for a schematic), however, must be self-consistent so that both instances of Kepler’s third law result in consistent masses. The triple system is then defined by five of the six parameters, with the sixth being constrained by both applications of Kepler’s third laws:

$$\begin{aligned} P_{\text{inner}}^2 &= \frac{4\pi^2}{G(M_1 + M_2)} a_{\text{inner}}^3, \\ P_{\text{outer}}^2 &= \frac{4\pi^2}{G((M_1 + M_2) + M_3)} a_{\text{outer}}^3, \end{aligned} \tag{6.1}$$

where

$$\begin{aligned} q_{\text{inner}} &\equiv \frac{M_2}{M_1}, \\ q_{\text{outer}} &\equiv \frac{M_3}{M_1 + M_2}. \end{aligned} \tag{6.2}$$

In PHOEBE 2, multiple stellar systems are defined with this “nested” hierarchical parameterization with the flexibility to choose any of the five parameters to be constrained by the others ( $q_{\text{inner}}$  is excluded as that would introduce the need to set the mass of either or

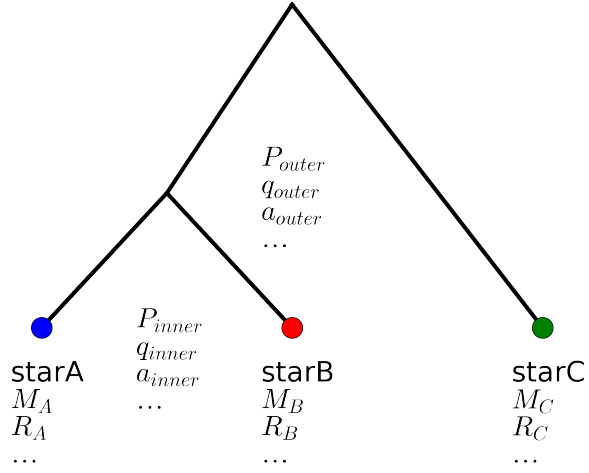


Figure 6.1 Schematic representation of the nested hierarchical parametrization of a triple system.

both stars in the inner binary):

$$\frac{a_{\text{inner}}^3}{P_{\text{inner}}^2} = \frac{a_{\text{outer}}^3}{P_{\text{outer}}^2} \frac{1}{1 + q_{\text{outer}}} . \quad (6.3)$$

For example, if both periods can be fitted and constrained via mutual eclipses,  $q_{\text{inner}}$  and  $a_{\text{inner}}$  via radial velocities, and  $a_{\text{outer}}$  via the amplitude of the ETVs of the inner binary, then it makes most sense to leave  $q_{\text{outer}}$  constrained. If, however, fitting a system in which the third star is instead on a wide orbit with an unknown period, then it may make more sense to leave  $P_{\text{outer}}$  constrained and fit the remaining five free parameters, with  $q_{\text{outer}}$  perhaps constrained by the presence of a triple-lined spectrum.

## 6.2 Dynamics

All parameters within PHOEBE 2 are defined at a reference time,  $t_0$ . This allows orbital elements to change in time due to dynamical interactions. As these orbital elements are expected to change with time in a dynamical multiple star system, using nested Keplerian

orbits alone is not sufficient. Instead, we determine the initial positions and velocities of all components at  $t_0$  using the nested Keplerian orbits, and use an N-body integrator to determine their positions and velocities at all other necessary times.

Within PHOEBE 2, we have incorporated the `rebound`<sup>1</sup> package (Rein and Liu, 2012) to handle N-body integration. This python package currently includes support for the following integrators: IAS15 (Rein and Spiegel, 2015), WHFAST (Rein and Tamayo, 2015; Wisdom and Holman, 1991), WHFASTHELIO, EULER, LEAPFROG, SEI (Rein and Tremaine, 2011), and HERMES.

Note that all dynamics done within PHOEBE 2 currently assume the stars are point masses, effectively ignoring any effects tides may have on the orbits. This assumption and its consequences are discussed further in §6.6.1.

Light time effects (both Rømer delay discussed in §5.6 and LTTE discussed in §5.7) are accounted for in PHOEBE 2 by advancing or retarding each component in its own orbit such that its light will reach the barycenter of the system (and therefore the observer on Earth) simultaneously. The implementation for Keplerian orbits is discussed in §3.1. Here we extend the same basic logic to dynamical N-body orbits. As depicted in Figure 6.2, each object is first placed in orbit according to the N-body integrator at the observation time  $t_{obs}$ . The radial distance between that position and the barycenter  $dz$  is then computed and used to estimate the time-shift  $dt$  required so that the light reaches the barycenter at  $t_{obs}$ . This process is repeated iteratively for each object until all objects are in their orbits as they would be viewed by the observer.

As this is done numerically within an N-body integrator, other effects such as dynamical changes to orbital elements (discussed in §5.4) or barycentric and asymmetric transverse velocities (BATV; discussed in §5.9 and Conroy et al. 2018) are automatically taken into account for each synthetic data point, regardless of whether an eclipse occurs at that time. Additionally, the assumptions made in the expressions provided in §5.9 are not necessary

---

<sup>1</sup><https://github.com/hannorein/rebound>

using this numerical approach — resulting in the most accurate eclipse times and synthetic photometry possible.

Although subtle for binaries without companions, LTTE and BATV can become significant for multiple star systems as the barycenter for each subsystem is in orbit around the system's barycenter itself. Together with dynamical effects, this can result in observable eclipse timing variations (see §6.5).

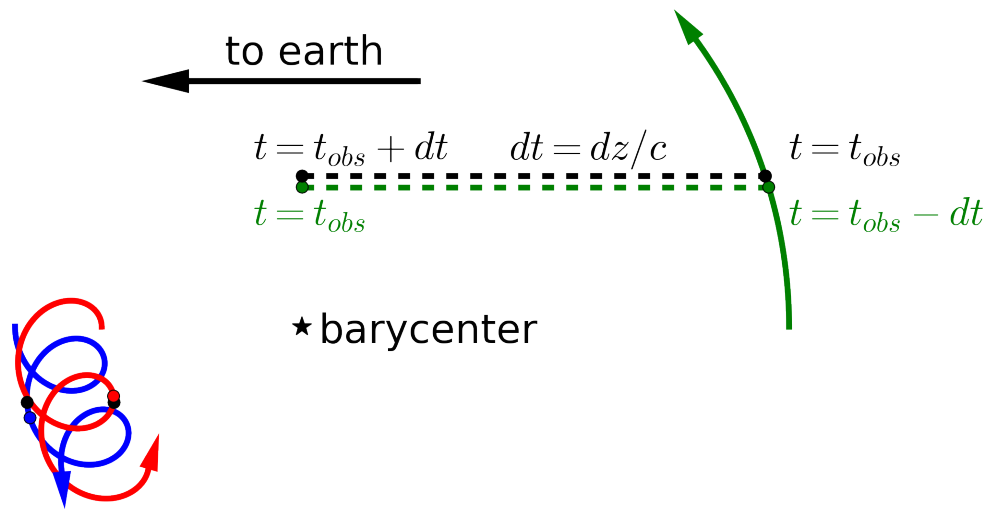


Figure 6.2 Schematic representation of light travel time corrections to the position of each star. Objects are placed in orbit according to N-body dynamics at time  $t = t_{obs}$  (black points and dashed line) and are then moved along their respective orbits by  $dt = dz/c$  so that their light arrives at the barycenter at  $t = t_{obs}$  (colored points and dashed line).

### 6.3 Stellar Surface Distortion

The Roche framework (Equation 3.1) allows for nicely parametrizing the equipotentials of stars in a binary system by describing the equipotentials in the rotating reference frame

of the primary component. This allows for easy surface discretization as well as volume conservation (see §3.2, §3.3, and Prša et al. 2016). Using a generic N-body equipotential becomes overly complicated because of the multiple rotating reference frames and becomes computationally prohibitive for volume conservation.

In order to apply the Roche framework to a system with N-body dynamics, we need to make a few assumptions. First, we assume that there is no mass-transfer and therefore hold all mass ratios fixed. Second, as in eccentric binary systems, we assume the volume of each star remains fixed and do so by recomputing the equipotential  $\Omega$  and re-discretizing the surface at each time as is done in the binary case in §3.3. With these assumptions, we need to compute  $\delta$  and  $F$  at each time from the N-body dynamics.

To do that, we compute an instantaneous Keplerian orbit at a given time that describes the current positions and velocities of each star in relation to its sibling in the defined hierarchy (see Figure 6.3). In the case where the sibling is itself an orbit containing multiple components, we assume that the total mass of those components is placed at the center-of-mass of that sub-system. From the computed instantaneous semi-major axis  $a_{inst}$  and separation, we determine the instantaneous unit-less separation  $\delta_{inst}$ . As the instantaneous orbital period  $P_{inst}$  changes, we adjust the synchronicity parameter  $F_{inst}$  under the assumption that each star’s rotation period remains fixed throughout the model (see §6.6.3 for a discussion on this assumption).

With  $q$  fixed and instantaneous values for  $\delta_{inst}$  and  $F_{inst}$  determined, we apply the volume conservation constraint to determine the surface of the star. Figure 6.3 shows a schematic representation of this process.

This “hybrid” Roche framework naturally only accounts for distortion between each star and its nearest neighbor in the hierarchy. In other words, a star in an inner-binary will not be directly distorted by the presence of a third component. This assumption is discussed in further detail in §6.6.2.

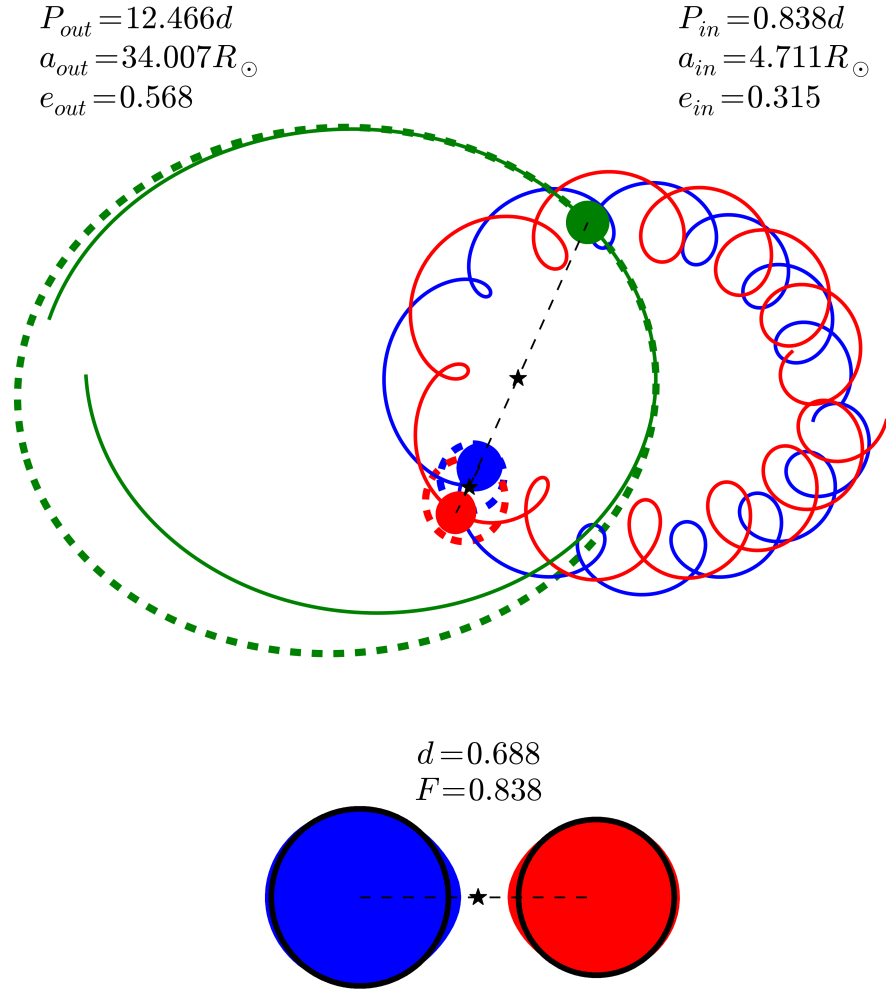


Figure 6.3 Schematic representation of the “hybrid” Roche distortion scheme implemented in PHOEBE. The solid lines represent the N-body dynamical positions provided by `rebound` for each star (red, blue, and green respectively). The dashed black lines represent the hierarchy connecting each star and the center-of-mass of its parent orbit. The dashed colored lines depict the computed instantaneous Keplerian orbit at the time of the current frame, with the orbital parameters on the top of the image and Roche parameters on the bottom of the image. At the bottom are the meshes of the inner stars distorted according to those instantaneous Roche parameters and compared to a sphere of the same radius (black circles).

#### 6.4 Eclipse Detection

There are two main computational bottlenecks in extending PHOEBE from binary stars to higher-order systems. The first of these is in discretization: as the orbits are not strictly Keplerian, the meshes must be recomputed (according to volume conservation) at each

time point. Unless circular hierarchical orbits are assumed, this step cannot be ignored or significantly optimized.

The second bottleneck is in eclipse detection. The cost of eclipse detection, as explained in §3.5 and Prša et al. (2016), goes as  $\sim \mathcal{O}(N^{1.5})$ . Increasing the number of components in a system, therefore, has a significant impact on the cost of eclipse detection. Fortunately, certain shortcuts can be made to optimize the computational cost of this operation.

At any given time, PHOEBE estimates which subset of all stars could possibly be eclipsing each other by determining whether their projected separations on the plane-of-sky are within the sum of their maximum radii. These maximum radii are conservatively determined as the radius of each star at periastron in its (strictly Keplerian) orbit. As the dynamical interactions could at some point bring a star within its Keplerian periastron distance, resulting in a larger radii, a conservative tolerance is used to ensure that eclipses will not be ignored. In practice, PHOEBE computes full eclipse detection for any set of stars that are within a tolerance of 10% of the estimated maximum sum of radii of those stars. Stars that are not deemed to be eclipsing any other star by this check are instead handled by only computing the visibility of elements with respect to the horizon.

## 6.5 Modeling Eclipse Timing Variations

ETVs have long been used to detect third components around eclipsing binary stars (see §4 for our search for third components within the *Kepler* EBs catalog). By measuring the time of the observed eclipses with respect to the linear ephemeris, extra components can be detected by their influence on both the radial position of the binary as it orbits the common center of mass (i.e. light travel time effects) as well as the perturbative effects on the binary’s orbit (i.e. dynamical effects). These various contributing factors are all discussed in detail in §5.

With the upcoming release of PHOEBE 2, ETVs will be a supported “observable” dataset. Although analytical expressions for these perturbations are known in the case of

triple systems (Borkovits et al., 2003, 2007, 2011; Conroy et al., 2018), PHOEBE computes eclipse times directly from the orbit by computing the time that minimizes the projected separation between the two eclipsing objects on the plane of the sky nearest to the expected time of eclipse from the provided epoch number (see Figure 6.4). Even for ellipsoidal variables in which an eclipse technically does not occur, this time still represents the measurable time of minimum flux due to the distorted surfaces of the stars.

With nested-Keplerian orbits (instead of the hybrid-method with dynamical treatment), Figure 6.5 shows that these ETVs roughly match the sum of those from the analytical LTTE expression given in Rappaport et al. (2013) and BATV given in §5.9 and Conroy

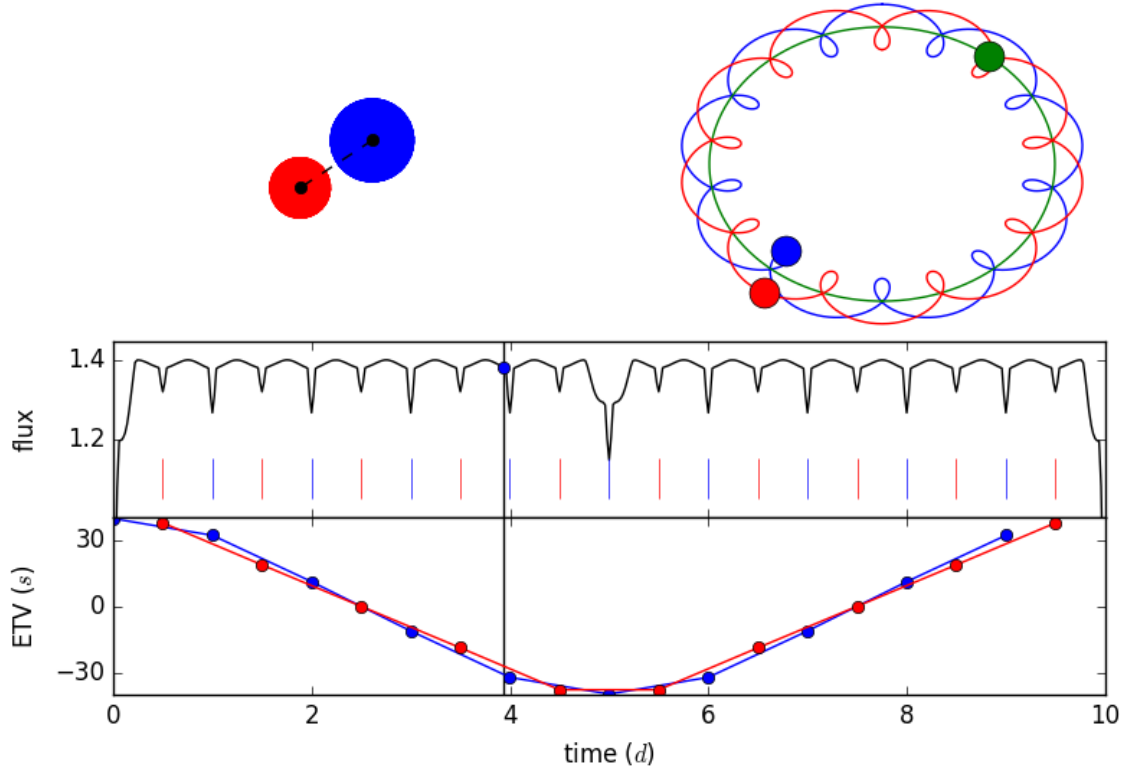


Figure 6.4 Eclipse times are computed by minimizing the projected distance (dashed line) on the plane-of-sky (upper-left). The middle panel shows the light curve with colored dashes marking the computed eclipse times, and the bottom panel shows the resulting ETV curve when subtracting the linear ephemeris.

et al. (2018).

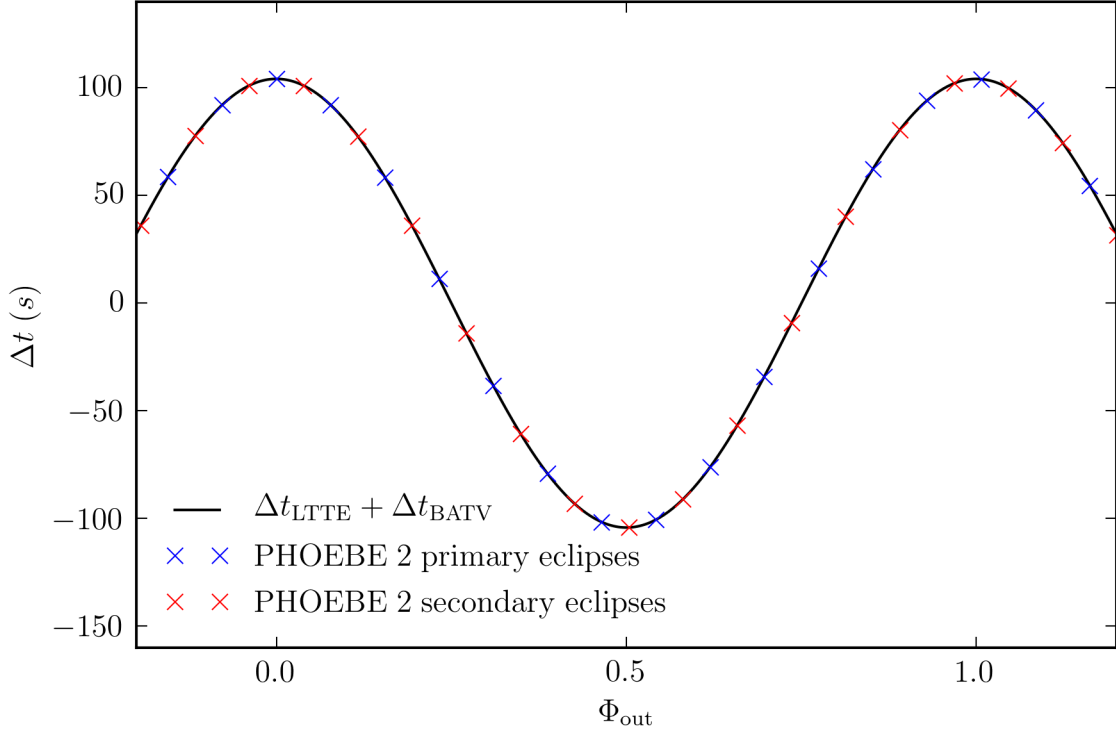


Figure 6.5 Computed ETVs for primary (blue) and secondary (red) eclipses for nested-Keplerian orbits compared to the analytical light travel time effect LTTE and BATV contributions.

## 6.6 Justification of Assumptions

In order to devise the “hybrid” approach that handles dynamical orbits with surface distortion in a computationally feasible manner - several assumptions and approximations had to be made. In the sections below, I list and justify those assumptions and discuss when a more robust method may be necessary.

### 6.6.1 Point Masses

Although the dynamical treatment implemented in PHOEBE 2 can handle changing orbits due to interactions between all masses in the system, these masses are all treated as point masses - effectively ignoring the tidal effects due to the distortions themselves.

Handling tidal effects could be possible and may be considered as an additional feature in the future, but would come with significant computational cost. In order to achieve this, each time-step would need to iterate between the dynamics changing the instantaneous orbits which affect the distortions and then those distortions in turn affecting the mass-distribution within each star feeding back into dynamical corrections. This would need to be an iterative procedure until the result converges within some acceptable tolerance. In addition to the computational complexity, the physical model would need to include the distribution of mass within the star and account for how (and how quickly) that mass redistributes to the “instantaneously” reacting outer layers.

Although tidal forces are known to affect orbits in some cases (e.g. apsidal motion in eccentric cases), the outer layers of a star contain a small percentage of the overall mass. Furthermore, the effect of these tides on the orbit occurs over a long timescale. With the exception of *extremely* distorted stars in eccentric orbits, the assumption of point masses for dynamics should hold over observable timescales.

### 6.6.2 Distortion Between Pairs

In order to still use the Roche framework, this hybrid approach in PHOEBE 2 only accounts for the surface distortion due to a component’s nearest neighbor in the hierarchy (i.e. in a hierarchical triple, the distortion of the stars in the inner binary only react to each other, and not the third mass, whereas the third component reacts to the inner binary as if it were a point mass located at the subsystem’s center of mass). For most *stable* hierarchical systems, this assumption should be fairly safe.

In order for a triple system to be dynamically stable it must be sufficiently hierarchical. According to Mikkola (2008), the stability limit can be generalized as  $d_{\text{outer, peri}}/a_{\text{inner}} > 3 - 4$  (see also Harrington, 1972; Bailyn, 1987; Eggleton and Kiseleva, 1995; Mardling and Aarseth, 2001). Since the stars in the inner binary will be most affected by the outer component when at closest approach, and distortion scales as  $(R/d)^6$  (where  $R$  is the radius of

the star and  $d$  is the separation between the two sibling stars), under the most conservative estimates the distortion on any of the stars in the inner binary due to the outer star is *at most* 0.07% of the distortion due to its pair:

$$\frac{(R/d_{\text{outer, peri}})^6}{(R/a_{\text{inner}})^6} = \left(\frac{a_{\text{inner}}}{d_{\text{outer, peri}}}\right)^6 = \left(\frac{1}{3}\right)^6 = 0.0007. \quad (6.4)$$

For these reasons, for any system which is dynamically stable, the assumption of distortions due to the nearest pair alone should be sufficient to within  $\sim 0.1\%$ . Although a more robust and generic equipotential could be computed, inverting the equations to solve for volume conservation would become much more computationally expensive.

### 6.6.3 Fixed Rotation Periods

As described in §6.3, we choose to retain the rotation period of each star and instead allow for the synchronicity Roche parameter  $F_{\text{inst}}$  to adjust to any change in the orbital period and/or semi-major axis of the instantaneous Keplerian orbit.

The obvious assumption may be to conserve the angular momentum of the entire system. However, there is no obvious way to distribute the changing orbital angular momentum between the individual stars in the system. Therefore, the simplest two assumptions to make would either be to preserve each star's synchronicity or rotational period. As the synchronicity timescale in an eccentric binary (Zahn, 2008; Moreno et al., 2011) is orders of magnitude longer than any observable timescale that would be used within PHOEBE 2 and therefore also longer than the observable dynamical effects, we instead preserve the initial rotational periods (even if at the cost of conserving total angular momentum).

In a sense this is similar to how stellar rotation is handled for eccentric binaries. The synchronicity parameter sets the rotation period (i.e. a synchronicity parameter of exactly one sets the rotation period to be exactly the orbital period). The rotational velocity is then held fixed throughout the orbit, regardless of the orbital velocity at a given time.

#### 6.6.4 Instantaneous Keplerian Orbits

The last approximation used in this hybrid method is that an unclosed N-body orbit can be instantaneously represented by a closed Keplerian orbit. This assumption is again safe as long as the given system is sufficiently hierarchical. The dynamical interactions between the components should only contribute a *perturbative* correction to the nested Keplerian orbits, making this approximation reasonable. In extreme, either short-lived or unphysical situations, this approximation may begin to breakdown, resulting in quick or even discontinuous changes to the underlying Keplerian orbits and therefore the resulting stellar distortions.

### 6.7 Utilizing Multiple Backends

As mentioned in §3.5, PHOEBE 2 is already inherently slower than other codes that include more approximations. This becomes even more significant for the higher-order systems. Although we have made efforts to optimize the code, PHOEBE 2 will likely always be significantly slower than many other codes.

For this reason, as well as to test the validity of various models, the PHOEBE 2 frontend has been designed with the capability of calling multiple backends. In the case of higher-order systems, `photodynam`<sup>2</sup> (Carter et al., 2011; Pál, 2012) is a highly-optimized code that can compute light curves of systems with generic hierarchies, but lacks surface distortion or advanced stellar atmospheres. We therefore include `photodynam` as an alternate-backend within the PHOEBE 2 frontend interface and handle translating between the parameterizations between the two backends.

This allows for fitting a higher-order system computationally feasible. An MCMC fitting run can be started with wide, conservative, priors to sample the entire parameter space using the optimized `photodynam`. Once the parameter space has been well-explored

---

<sup>2</sup>A forked version is available at <http://github.com/phoebe-project/photodynam>

and the posteriors begin to converge on a final solution, the user can switch to using the PHOEBE 2 backend and enable the advanced, but computationally expensive, effects — including the hybrid surface distortion.

Figure 6.6 shows an example triple system, highlighting the importance of surface distortion on the final light curve. However, the model with spherical stars still roughly models the timing and shapes of the triple events. Here in this system, the full “hybdrid” distortion model will be necessary for both the ellipsoidal variables for the inner binary and for the exact shape of the triple eclipse events.

By utilizing this approach, PHOEBE 2 will allow for fitting the triple and higher-order systems to unprecedented accuracy and precision, with the use of moderate HPC computing resources. With these robust models and parameter uncertainties, we can provide both benchmark stellar parameters as well as test the distributions of orbital parameters provided by KCTF and other binary formation theories.

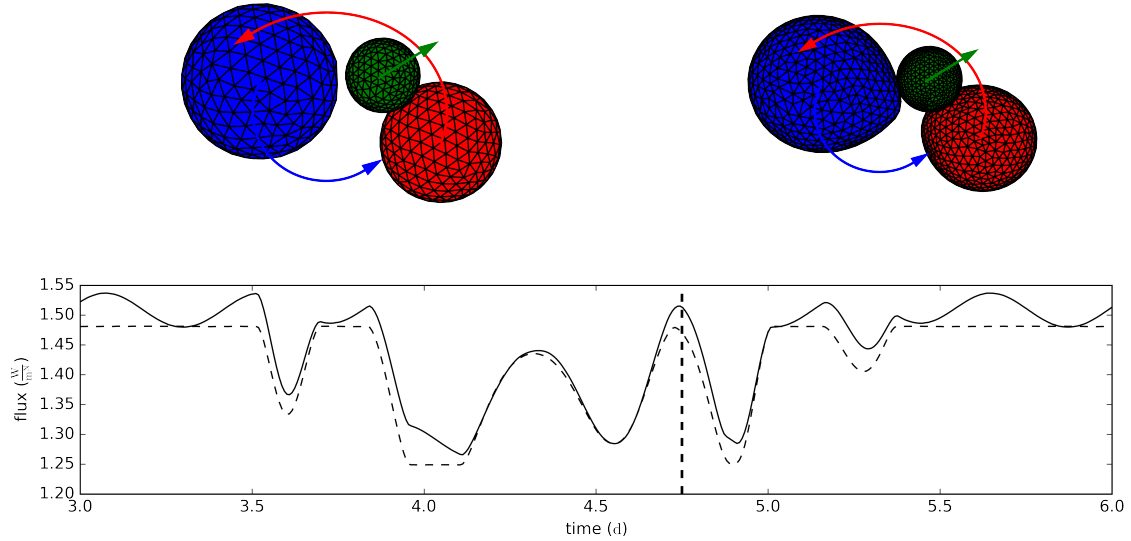


Figure 6.6 Light curve of an example triple system with the “hybrid” Roche distortions (solid) compared to spherical stars (dashed). The meshes above are shown at the time indicated with the vertical dashed lines and are also shown both with the “hybrid” Roche distortions (upper-right) and spherical stars (upper-left). At this time in particular, the distortions clearly make a noticeable difference in whether the third (green) component eclipses the inner binary (red and blue).

## Chapter 7

### Discussion and Conclusions

The work in this dissertation represents the first steps towards robustly modeling stellar triples and higher-order systems to the precision available by modern photometric surveys. To accomplish this, I led the effort to identify these candidate triple systems from *Kepler* EBs by measuring their ETVs, obtain additional follow-up data including spectroscopy from the ground, and introduced a novel hybrid approach to handling the subtleties of modeling these systems within PHOEBE 2 — including various astrophysical contributions to the eclipse timings, dynamical perturbations caused by the multiple stars in the system, and stellar distortion.

I have also described the theoretical formulation and consequences of a previously-overlooked contribution to ETVs, called BATV, which is necessary to reach this same desired level of precision when modeling ETVs. In addition to multiple star systems, BATV also has consequences for EBs in which there is a systemic velocity on the plane of sky. This manifests itself in several physical cases: including apsidal motion, a change in inclination, and the measurement of mass ratio from the phase separation between primary and secondary eclipses.

With the framework now in place in PHOEBE 2 to model these systems to the necessary precision, the modeling of individual triple and higher-order systems can finally begin. As already mentioned in §4.2.2, KIC 2835289 is a perfect example of a tight inner binary with a wide and eccentric third body identified both in the ETVs and in mutual eclipsing events. This system is particularly interesting scientifically as it may be a post-KCTF system that can test the predictions of the expected mutual inclination. Initial rough models show that the mutual inclination may agree well with these predictions (Conroy et al., 2015).

This work enables the modeling of dynamical multiple stellar systems, and with sev-

eral systems already identified in the *Kepler* EB sample ready for detailed modeling and more expected from future high-precision missions on the horizon, we will soon be able to quickly expand the sample of higher-order systems with precise solution. By obtaining the high-precision data necessary and then robustly modeling these systems, we can slowly acquire the statistical sample needed to test theories of close binary formation by comparing the observed distribution in mutual inclination verse those expected from simulations by Fabrycky and Tremaine (2007).

As these samples are being assembled, we will be able to constrain the stellar parameters of the close binaries to unprecedented precision — thanks to the mutual eclipse events that will break the solution degeneracies that have limited our abilities to model EBs to higher precision. These will become new benchmark systems, with an improvement up to an order of magnitude in precision better than has been possible with EBs. These new benchmark systems can then play a crucial role in informing and calibrating stellar population studies.

## Appendix A

### Orbital Elements for BATV

### Orbital Elements for Binary Systems

We can write several of the terms in Equation (5.28) with orbital elements of a binary star system.

For the velocity of the front star (f) in our binary (fb), we want the velocity projected along the longitude of ascending node. That can be represented as follows:

$$v_{x,f,\text{orb}} = \sqrt{\frac{G}{M_{\text{fb}} a_{\text{fb}} (1 - e_{\text{fb}}^2)}} M_{\text{b}} \left[ -\sin(v_f(t)) \cos \omega_{\text{fb}} + [\cos(v_f(t)) + e_{\text{fb}}] \sin \omega_{\text{fb}} \right], \quad (\text{A.1})$$

where  $v(t)$  is the true anomaly of a given star at time  $t$ ,  $M$  is mass,  $\omega$  is the argument of periastron,  $a$  is the semi-major, and  $e$  is the eccentricity of the orbit.

The separation between the front and back components projected along the line-of-sight,  $\Delta z_{\text{fb}}$ , can be written as follows:

$$\Delta z_{\text{fb}} = \frac{a_{\text{fb}} (1 - e_{\text{fb}}^2)}{1 + e_{\text{fb}} \cos(v_f(t))} \sin_{\text{fb}} [\cos(\omega_{\text{fb}} + v_f(t)) + e_{\text{fb}} \cos \omega_{\text{fb}}]. \quad (\text{A.2})$$

### Orbital Elements for Hierarchical Triple Systems

In the case of a hierarchical triple system, Equation (5.28) can be expressed in terms of orbital elements of both the inner and outer Keplerian orbits.

For the velocity of the eclipsing component (f) in our inner-binary (fb), we want the velocity projected along the longitude of ascending node for that same orbit (fb) and there-

fore can use the same Equation (A.1), as for a single binary system. Likewise, we can use Equation (A.2) for  $\Delta z_{\text{fb}}$ .

The barycentric transverse velocity,  $v_{x,\text{bary}}$  is the velocity of the inner-binary (fb) caused by its motion within the outer-orbit (fbt) projected along the same direction as  $v_{x,\text{f,orb}}$ :

$$v_{x,\text{bary}} = \sqrt{\frac{G}{M_{\text{fbt}} a_{fbt} (1 - e_{fbt}^2)}} m_t \left[ -\sin(v_{fb}(t)) \cos \omega_{fbt} + [\cos(v_{fb}(t)) + e_{fbt}] \sin \omega_{fbt} \right] \cos(\Omega_{fbt} - \Omega_{fb}). \quad (\text{A.3})$$

## REFERENCES

- M. Abdul-Masih, A. Prša, K. Conroy, S. Bloemen, T. Boyajian, L. R. Doyle, C. Johnston, V. Kostov, D. W. Latham, G. Matijević, A. Shporer, and J. Southworth. Kepler Eclipsing Binary Stars. VIII. Identification of False Positive Eclipsing Binaries and Re-extraction of New Light Curves. *AJ*, 151:101, April 2016. doi: 10.3847/0004-6256/151/4/101.
- J. H. Applegate. A mechanism for orbital period modulation in close binaries. *ApJ*, 385: 621–629, February 1992. doi: 10.1086/170967.
- Annie Baglin. Corot: A minisat for pionnier science, asteroseismology and planets finding. *Advances in Space Research*, 31:345, 2003. doi: 10.1016/S0273-1177(02)00624-5.
- C. D. Bailyn. *Low mass X-ray binaries in globular clusters and hierarchical triple systems*. PhD thesis, Harvard University, Cambridge, MA., 1987.
- B. N. Barlow, R. A. Wade, and S. E. Liss. The Rømer Delay and Mass Ratio of the sdB+dM Binary 2M 1938+4603 from Kepler Eclipse Timings. *ApJ*, 753:101, July 2012. doi: 10.1088/0004-637X/753/2/101.
- N. M. Batalha, W. J. Borucki, D. G. Koch, S. T. Bryson, M. R. Haas, T. M. Brown, D. A. Caldwell, J. R. Hall, R. L. Gilliland, D. W. Latham, S. Meibom, and D. G. Monet. Selection, Prioritization, and Characteristics of Kepler Target Stars. *ApJL*, 713:L109–L114, April 2010. doi: 10.1088/2041-8205/713/2/L109.
- P. G. Beck, K. Hambleton, J. Vos, T. Kallinger, S. Bloemen, A. Tkachenko, R. A. García, R. H. Østensen, C. Aerts, D. W. Kurtz, J. De Ridder, S. Hekker, K. Pavlovski, S. Mathur, K. De Smedt, A. Derekas, E. Corsaro, B. Mosser, H. Van Winckel, D. Huber, P. De-groote, G. R. Davies, A. Prša, J. Debosscher, Y. Elsworth, P. Nemeth, L. Siess, V. S. Schmid, P. I. Pápics, B. L. de Vries, A. J. van Marle, P. Marcos-Arenal, and A. Lobel.

Pulsating red giant stars in eccentric binary systems discovered from Kepler space-based photometry. A sample study and the analysis of KIC 5006817. *A&A*, 564:A36, April 2014. doi: 10.1051/0004-6361/201322477.

I. A. Bonnell. The Formation of Close Binary Stars. In H. Zinnecker and R. Mathieu, editors, *The Formation of Binary Stars*, volume 200 of *IAU Symposium*, page 23, 2001.

T. Borkovits, B. Érdi, E. Forgács-Dajka, and T. Kovács. On the detectability of long period perturbations in close hierarchical triple stellar systems. *A&A*, 398:1091–1102, February 2003. doi: 10.1051/0004-6361:20021688.

T. Borkovits, E. Forgács-Dajka, and Z. Regály. Tidal and rotational effects in the perturbations of hierarchical triple stellar systems. II. Eccentric systems - the case of AS Camelopardalis. *A&A*, 473:191–206, October 2007. doi: 10.1051/0004-6361:20077793.

T. Borkovits, S. Csizmadia, E. Forgács-Dajka, and T. Hegedüs. Transit timing variations in eccentric hierarchical triple exoplanetary systems. I. Perturbations on the time scale of the orbital period of the perturber. *A&A*, 528:A53, April 2011. doi: 10.1051/0004-6361/201015867.

W. J. Borucki, D. G. Koch, G. Basri, N. Batalha, T. M. Brown, S. T. Bryson, D. Caldwell, J. Christensen-Dalsgaard, W. D. Cochran, E. DeVore, E. W. Dunham, T. N. Gautier, III, J. C. Geary, R. Gilliland, A. Gould, S. B. Howell, J. M. Jenkins, D. W. Latham, J. J. Lissauer, G. W. Marcy, J. Rowe, D. Sasselov, A. Boss, D. Charbonneau, D. Ciardi, L. Doyle, A. K. Dupree, E. B. Ford, J. Fortney, M. J. Holman, S. Seager, J. H. Stefanen, J. Tarter, W. F. Welsh, C. Allen, L. A. Buchhave, J. L. Christiansen, B. D. Clarke, S. Das, J.-M. Désert, M. Endl, D. Fabrycky, F. Fressin, M. Haas, E. Horch, A. Howard, H. Isaacson, H. Kjeldsen, J. Kolodziejczak, C. Kulesa, J. Li, P. W. Lucas, P. Machalek, D. McCarthy, P. MacQueen, S. Meibom, T. Miquel, A. Prsa, S. N. Quinn, E. V. Quintana,

D. Ragozzine, W. Sherry, A. Shporer, P. Tenenbaum, G. Torres, J. D. Twicken, J. Van Cleve, L. Walkowicz, F. C. Witteborn, and M. Still. Characteristics of Planetary Candidates Observed by Kepler. II. Analysis of the First Four Months of Data. *ApJ*, 736:19, July 2011. doi: 10.1088/0004-637X/736/1/19.

William Borucki, David Koch, Gibor Basri, Natalie Batalha, Timothy Brown, Douglas Caldwell, John Caldwell, Jrgen Christensen-Dalsgaard, William Cochran, Edna DeVore, Edward Dunham, Andrea Dupree, Thomas Gautier, John Geary, Ronald Gilliland, Alan Gould, Steve Howell, Jon Jenkins, Yoji Kondo, David Latham, Geoffrey Marcy, Sren Meibom, Hans Kjeldsen, Jack Lissauer, David Monet, David Morrison, Dimitar Sasselov, Jill Tarter, Alan Boss, Don Brownlee, Toby Owen, Derek Buzasi, David Charbonneau, Laurance Doyle, Jonathan Fortney, Eric Ford, Matthew Holman, Sara Seager, Jason Steffen, William Welsh, Jason Rowe, Howard Anderson, Lars Buchhave, David Ciardi, Lucianne Walkowicz, William Sherry, Elliott Horch, Howard Isaacson, Mark Everett, Debra Fischer, Guillermo Torres, John Johnson, Michael Endl, Phillip MacQueen, Stephen Bryson, Jessie Dotson, Michael Haas, Jeffrey Kolodziejczak, Cleve Va, Hema Chandrasekaran, Joseph Twicken, Elisa Quintana, Bruce Clarke, Christopher Allen, Jie Li, Haley Wu, Peter Tenenbaum, Ekaterina Verner, Frederick Bruhweiler, Jason Barnes, and Andrej Prsa. Kepler planet-detection mission: Introduction and first results. *Science*, 327:977, 2010. doi: 10.1126/science.1185402.

M. Brož. An Advanced N-body Model for Interacting Multiple Stellar Systems. *ApJS*, 230:19, June 2017. doi: 10.3847/1538-4365/aa7207.

D. A. Caldwell, J. J. Kolodziejczak, J. E. Van Cleve, J. M. Jenkins, P. R. Gazis, V. S. Aragabright, E. E. Bachtell, E. W. Dunham, J. C. Geary, R. L. Gilliland, H. Chandrasekaran, J. Li, P. Tenenbaum, H. Wu, W. J. Borucki, S. T. Bryson, J. L. Dotson, M. R. Haas, and D. G. Koch. Instrument Performance in Kepler's First Months. *ApJL*, 713:L92–L96, April 2010. doi: 10.1088/2041-8205/713/2/L92.

J. A. Carter, D. C. Fabrycky, D. Ragozzine, M. J. Holman, S. N. Quinn, D. W. Latham, L. A. Buchhave, J. Van Cleve, W. D. Cochran, M. T. Cote, M. Endl, E. B. Ford, M. R. Haas, J. M. Jenkins, D. G. Koch, J. Li, J. J. Lissauer, P. J. MacQueen, C. K. Middour, J. A. Orosz, J. F. Rowe, J. H. Steffen, and W. F. Welsh. KOI-126: A Triply Eclipsing Hierarchical Triple with Two Low-Mass Stars. *Science*, 331:562, February 2011. doi: 10.1126/science.1201274.

K. Conroy, K. A. Prsa, Stassun, and J. Orosz. Call for Follow-Up Observations of the Dynamically Changing Triple Star KIC 2835289. *Information Bulletin on Variable Stars*, 6138, April 2015.

K. E. Conroy, A. Prša, K. G. Stassun, S. Bloemen, M. Parvizi, B. Quarles, T. Boyajian, T. Barclay, A. Shporer, D. W. Latham, and M. Abdul-Masih. Kepler Eclipsing Binary Stars. V. Identification of 31 Candidate Eclipsing Binaries in the K2 Engineering Dataset. , 126:914, October 2014a. doi: 10.1086/678953.

K. E. Conroy, A. Prša, K. G. Stassun, J. A. Orosz, D. C. Fabrycky, and W. F. Welsh. Kepler Eclipsing Binary Stars. IV. Precise Eclipse Times for Close Binaries and Identification of Candidate Three-body Systems. *AJ*, 147:45, February 2014b. doi: 10.1088/0004-6256/147/2/45.

K. E. Conroy, A. Prša, M. Horvat, and K. G. Stassun. The Effects of Barycentric and Asymmetric Transverse Velocities on Eclipse and Transit Times. *ApJ*, 854:163, February 2018. doi: 10.3847/1538-4357/aaa3ea.

J. H. J. de Bruijne. Science performance of Gaia, ESA's space-astrometry mission. *Ap&SS*, 341:31–41, September 2012. doi: 10.1007/s10509-012-1019-4.

A. Derekas, L. L. Kiss, and T. R. Bedding. Eclipsing Binaries in the MACHO Database: New Periods and Classifications for 3031 Systems in the Large Magellanic Cloud. *ApJ*, 663:249–257, July 2007. doi: 10.1086/517994.

- J. Devor. Solutions for 10,000 Eclipsing Binaries in the Bulge Fields of OGLE II Using DEBiL. *ApJ*, 628:411–425, July 2005. doi: 10.1086/431170.
- S. Dhital, A. A. West, K. G. Stassun, and J. J. Bochanski. Sloan Low-mass Wide Pairs of Kinematically Equivalent Stars (SLoWPoKES): A Catalog of Very Wide, Low-mass Pairs. *AJ*, 139:2566–2586, June 2010. doi: 10.1088/0004-6256/139/6/2566.
- L. R. Doyle, J. A. Carter, D. C. Fabrycky, R. W. Slawson, S. B. Howell, J. N. Winn, J. A. Orosz, A. Prša, W. F. Welsh, S. N. Quinn, D. Latham, G. Torres, L. A. Buchhave, G. W. Marcy, J. J. Fortney, A. Shporer, E. B. Ford, J. J. Lissauer, D. Ragozzine, M. Rucker, N. Batalha, J. M. Jenkins, W. J. Borucki, D. Koch, C. K. Middour, J. R. Hall, S. McCauliff, M. N. Fanelli, E. V. Quintana, M. J. Holman, D. A. Caldwell, M. Still, R. P. Stefanik, W. R. Brown, G. A. Esquerdo, S. Tang, G. Furesz, J. C. Geary, P. Berlind, M. L. Calkins, D. R. Short, J. H. Steffen, D. Sasselov, E. W. Dunham, W. D. Cochran, A. Boss, M. R. Haas, D. Buzasi, and D. Fischer. Kepler-16: A Transiting Circumbinary Planet. *Science*, 333:1602, September 2011. doi: 10.1126/science.1210923.
- P. Eggleton and L. Kiseleva. An Empirical Condition for Stability of Hierarchical Triple Systems. *ApJ*, 455:640, December 1995. doi: 10.1086/176611.
- D. Fabrycky and S. Tremaine. Shrinking Binary and Planetary Orbits by Kozai Cycles with Tidal Friction. *ApJ*, 669:1298–1315, November 2007. doi: 10.1086/521702.
- D. C. Fabrycky. Non-Keplerian Dynamics of Exoplanets. In S. Seager, editor, *Exoplanets*, pages 217–238. University of Arizona Press, December 2010.
- G. Ferrero, R. Gamen, O. Benvenuto, and E. Fernández-Lajús. Apsidal motion in massive close binary systems - I. HD 165052, an extreme case? *MNRAS*, 433:1300–1311, August 2013. doi: 10.1093/mnras/stt812.
- D. A. Fischer, M. E. Schwamb, K. Schawinski, C. Lintott, J. Brewer, M. Giguere, S. Lynn, M. Parrish, T. Sartori, R. Simpson, A. Smith, J. Spronck, N. Batalha, J. Rowe, J. Jenkins,

S. Bryson, A. Prsa, P. Tenenbaum, J. Crepp, T. Morton, A. Howard, M. Beleu, Z. Kaplan, N. Vannispern, C. Sharzer, J. Defouw, A. Hajduk, J. P. Neal, A. Nemec, N. Schuepbach, and V. Zimmermann. Planet Hunters: the first two planet candidates identified by the public using the Kepler public archive data. *MNRAS*, 419:2900–2911, February 2012. doi: 10.1111/j.1365-2966.2011.19932.x.

Gaia Collaboration, A. G. A. Brown, A. Vallenari, T. Prusti, J. H. J. de Bruijne, F. Mignard, R. Drimmel, C. Babusiaux, C. A. L. Bailer-Jones, U. Bastian, and et al. Gaia Data Release 1. Summary of the astrometric, photometric, and survey properties. *A&A*, 595: A2, November 2016a. doi: 10.1051/0004-6361/201629512.

Gaia Collaboration, T. Prusti, J. H. J. de Bruijne, A. G. A. Brown, A. Vallenari, C. Babusiaux, C. A. L. Bailer-Jones, U. Bastian, M. Biermann, D. W. Evans, and et al. The Gaia mission. *A&A*, 595:A1, November 2016b. doi: 10.1051/0004-6361/201629272.

B. S. Gaudi, K. G. Stassun, K. A. Collins, T. G. Beatty, G. Zhou, D. W. Latham, A. Bieryla, J. D. Eastman, R. J. Siverd, J. R. Crepp, E. J. Gonzales, D. J. Stevens, L. A. Buchhave, J. Pepper, M. C. Johnson, K. D. Colon, E. L. N. Jensen, J. E. Rodriguez, V. Bozza, S. C. Novati, G. D’Ago, M. T. Dumont, T. Ellis, C. Gaillard, H. Jang-Condell, D. H. Kasper, A. Fukui, J. Gregorio, A. Ito, J. F. Kielkopf, M. Manner, K. Matt, N. Narita, T. E. Oberst, P. A. Reed, G. Scarpetta, D. C. Stephens, R. R. Yeigh, R. Zambelli, B. J. Fulton, A. W. Howard, D. J. James, M. Penny, D. Bayliss, I. A. Curtis, D. L. Depoy, G. A. Esquerdo, A. Gould, M. D. Joner, R. B. Kuhn, J. Labadie-Bartz, M. B. Lund, J. L. Marshall, K. K. McLeod, R. W. Pogge, H. Relles, C. Stockdale, T. G. Tan, M. Trueblood, and P. Trueblood. A giant planet undergoing extreme-ultraviolet irradiation by its hot massive-star host. *Nature*, 546:514–518, June 2017. doi: 10.1038/nature22392.

P. Gaulme, J. McKeever, M. L. Rawls, J. Jackiewicz, B. Mosser, and J. A. Guzik. Red Giants in Eclipsing Binary and Multiple-star Systems: Modeling and Asteroseis-

mic Analysis of 70 Candidates from Kepler Data. *ApJ*, 767:82, April 2013. doi: 10.1088/0004-637X/767/1/82.

P. Gaulme, J. Jackiewicz, T. Appourchaux, and B. Mosser. Surface Activity and Oscillation Amplitudes of Red Giants in Eclipsing Binaries. *ApJ*, 785:5, April 2014. doi: 10.1088/0004-637X/785/1/5.

D. R. Gies, S. J. Williams, R. A. Matson, Z. Guo, S. M. Thomas, J. A. Orosz, and G. J. Peters. A Search for Hierarchical Triples using Kepler Eclipse Timing. *AJ*, 143:137, June 2012. doi: 10.1088/0004-6256/143/6/137.

A. Gimenez and J. M. Garcia-Pelayo. A new method for the analysis of apsidal motions in eclipsing binaries. *Ap&SS*, 92:203–222, May 1983. doi: 10.1007/BF00653602.

Herbert Goldstein. *Classical mechanics*. World student series. Addison-Wesley, Reading (Mass.), Menlo Park (Calif.), Amsterdam, 1980. ISBN 0-201-02969-3. URL <http://opac.inria.fr/record=b1078625>.

E. F. Guinan and F. P. Maloney. The apsidal motion of the eccentric eclipsing binary DI Herculis - an apparent discrepancy with general relativity. *AJ*, 90:1519–1528, August 1985. doi: 10.1086/113865.

E. F. Guinan, E. L. Fitzpatrick, L. E. DeWarf, F. P. Maloney, P. A. Maurone, I. Ribas, J. D. Pritchard, D. H. Bradstreet, and A. Giménez. The Distance to the Large Magellanic Cloud from the Eclipsing Binary HV 2274. *ApJL*, 509:L21–L24, December 1998. doi: 10.1086/311760.

K. Hambleton, D. W. Kurtz, A. Prša, S. N. Quinn, J. Fuller, S. J. Murphy, S. E. Thompson, D. W. Latham, and A. Shporer. KIC 3749404: a heartbeat star with rapid apsidal advance indicative of a tertiary component. *MNRAS*, 463:1199–1212, December 2016. doi: 10.1093/mnras/stw1970.

- K. M. Hambleton, D. W. Kurtz, A. Prša, J. A. Guzik, K. Pavlovski, S. Bloemen, J. Southworth, K. Conroy, S. P. Littlefair, and J. Fuller. KIC 4544587: an eccentric, short-period binary system with  $\delta$  Sct pulsations and tidally excited modes. *MNRAS*, 434:925–940, September 2013. doi: 10.1093/mnras/stt886.
- R. S. Harrington. Dynamical evolution of triple stars. *AJ*, 73:190–194, April 1968. doi: 10.1086/110614.
- R. S. Harrington. The Stellar Three-Body Problem. *Celestial Mechanics*, 1:200–209, June 1969. doi: 10.1007/BF01228839.
- R. S. Harrington. Stability Criteria for Triple Stars. *Celestial Mechanics*, 6:322–327, November 1972. doi: 10.1007/BF01231475.
- J. D. Hartman and G. Á. Bakos. VARTOOLS: A program for analyzing astronomical time-series data. *Astronomy and Computing*, 17:1–72, October 2016. doi: 10.1016/j.ascom.2016.05.006.
- E. Hartmann. A marching method for the triangulation of surfaces. *The Visual Computer*, 14:95–108, 1998.
- R. W. Hilditch. *An Introduction to Close Binary Stars*. May 2001.
- John F. Hughes, Andries van Dam, Morgan McGuire, David F. Sklar, James D. Foley, Steven K. Feiner, and Kurt Akeley. *Computer graphics: principles and practice (3rd ed.)*. Addison-Wesley Professional, Boston, MA, USA, July 2013. ISBN 0321399528.
- J. M. Jenkins, D. A. Caldwell, H. Chandrasekaran, J. D. Twicken, S. T. Bryson, E. V. Quintana, B. D. Clarke, J. Li, C. Allen, P. Tenenbaum, H. Wu, T. C. Klaus, J. Van Cleve, J. A. Dotson, M. R. Haas, R. L. Gilliland, D. G. Koch, and W. J. Borucki. Initial Characteristics of Kepler Long Cadence Data for Detecting Transiting Planets. *ApJL*, 713:L120–L125, April 2010. doi: 10.1088/2041-8205/713/2/L120.

J. Juryšek, P. Zasche, M. Wolf, J. Vraštil, D. Vokrouhlický, M. Skarka, J. Liška, J. Janík, M. Zejda, P. Kurfürst, and E. Paunzen. New inclination changing eclipsing binaries in the Magellanic Clouds. *ArXiv e-prints*, September 2017.

Nicholas Kaiser, Herve Aussel, Barry Burke, Hans Boesgaard, Ken Chambers, Mark Chun, James Heasley, Klaus-Werner Hodapp, Bobby Hunt, Robert Jedicke, D. Jewitt, Rolf Kudritzki, Gerard Luppino, Michael Maberry, Eugene Magnier, David Monet, Peter Onaka, Andrew Pickles, Pui Rhoads, Theodore Simon, Alexander Szalay, Istvan Szapudi, David Tholen, John Tonry, Mark Waterson, and John Wick. Pan-starrs: A large synoptic survey telescope array. *Survey and Other Telescope Technologies and Discoveries*, 4836:154, 2002. doi: 10.1117/12.457365.

D. L. Kaplan. Mass Constraints from Eclipse Timing in Double White Dwarf Binaries. *ApJL*, 717:L108–L112, July 2010. doi: 10.1088/2041-8205/717/2/L108.

D. L. Kaplan, T. R. Marsh, A. N. Walker, L. Bildsten, M. C. P. Bours, E. Breedt, C. M. Copperwheat, V. S. Dhillon, S. B. Howell, S. P. Littlefair, A. Shporer, and J. D. R. Steinfadt. Properties of an Eclipsing Double White Dwarf Binary NLTT 11748. *ApJ*, 780:167, January 2014. doi: 10.1088/0004-637X/780/2/167.

B. Kirk, K. Conroy, A. Prša, M. Abdul-Masih, A. Kochoska, G. Matijević, K. Hambleton, T. Barclay, S. Bloemen, T. Boyajian, L. R. Doyle, B. J. Fulton, A. J. Hoekstra, K. Jek, S. R. Kane, V. Kostov, D. Latham, T. Mazeh, J. A. Orosz, J. Pepper, B. Quarles, D. Ragozzine, A. Shporer, J. Southworth, K. Stassun, S. E. Thompson, W. F. Welsh, E. Agol, A. Derekas, J. Devor, D. Fischer, G. Green, J. Gropp, T. Jacobs, C. Johnston, D. M. LaCourse, K. Saetre, H. Schwengeler, J. Toczyski, G. Werner, M. Garrett, J. Gore, A. O. Martinez, I. Spitzer, J. Stevick, P. C. Thomadis, E. H. Vrijmoet, M. Yenawine, N. Batalha, and W. Borucki. Kepler Eclipsing Binary Stars. VII. The Catalog of Eclipsing Binaries Found in the Entire Kepler Data Set. *AJ*, 151:68, March 2016. doi: 10.3847/0004-6256/151/3/68.

L. G. Kiseleva, P. P. Eggleton, and S. Mikkola. Tidal friction in triple stars. *MNRAS*, 300: 292–302, October 1998. doi: 10.1046/j.1365-8711.1998.01903.x.

D. G. Koch, W. J. Borucki, G. Basri, N. M. Batalha, T. M. Brown, D. Caldwell, J. Christensen-Dalsgaard, W. D. Cochran, E. DeVore, E. W. Dunham, T. N. Gautier, III, J. C. Geary, R. L. Gilliland, A. Gould, J. Jenkins, Y. Kondo, D. W. Latham, J. J. Lissauer, G. Marcy, D. Monet, D. Sasselov, A. Boss, D. Brownlee, J. Caldwell, A. K. Dupree, S. B. Howell, H. Kjeldsen, S. Meibom, D. Morrison, T. Owen, H. Reitsema, J. Tarter, S. T. Bryson, J. L. Dotson, P. Gazis, M. R. Haas, J. Kolodziejczak, J. F. Rowe, J. E. Van Cleve, C. Allen, H. Chandrasekaran, B. D. Clarke, J. Li, E. V. Quintana, P. Tenenbaum, J. D. Twicken, and H. Wu. Kepler Mission Design, Realized Photometric Performance, and Early Science. *ApJL*, 713:L79, April 2010. doi: 10.1088/2041-8205/713/2/L79.

Y. Kozai. Secular perturbations of asteroids with high inclination and eccentricity. *AJ*, 67: 591, November 1962. doi: 10.1086/108790.

D. M. LaCourse, K. J. Jek, T. L. Jacobs, T. Winarski, T. S. Boyajian, S. A. Rappaport, R. Sanchis-Ojeda, K. E. Conroy, L. Nelson, T. Barclay, D. A. Fischer, J. R. Schmitt, J. Wang, K. G. Stassun, J. Pepper, J. L. Coughlin, A. Shporer, and A. Prša. Kepler eclipsing binary stars - VI. Identification of eclipsing binaries in the K2 Campaign 0 data set. *MNRAS*, 452:3561–3592, October 2015. doi: 10.1093/mnras/stv1475.

C. H. S. Lacy, B. E. Helt, and L. P. R. Vaz. V907 Scorpii: A Remarkable Binary Star Whose Eclipses Turn On and Off and On and Off. *AJ*, 117:541–547, January 1999. doi: 10.1086/300710.

N. M. Law, S. Dhital, A. Kraus, K. G. Stassun, and A. A. West. The High-order Multiplicity of Unusually Wide M Dwarf Binaries: Eleven New Triple and Quadruple Systems. *ApJ*, 720:1727–1737, September 2010. doi: 10.1088/0004-637X/720/2/1727.

H. F. Levison and M. J. Duncan. The long-term dynamical behavior of short-period comets. *Icarus*, 108:18–36, March 1994. doi: 10.1006/icar.1994.1039.

M. L. Lidov. The evolution of orbits of artificial satellites of planets under the action of gravitational perturbations of external bodies. *Planet. Space Sci.*, 9:719–759, October 1962. doi: 10.1016/0032-0633(62)90129-0.

L. Lindegren, U. Lammers, U. Bastian, J. Hernández, S. Klioner, D. Hobbs, A. Bombrun, D. Michalik, M. Ramos-Lerate, A. Butkevich, G. Comoretto, E. Joliet, B. Holl, A. Hutton, P. Parsons, H. Steidelmüller, U. Abbas, M. Altmann, A. Andrei, S. Anton, N. Bach, C. Barache, U. Becciani, J. Berthier, L. Bianchi, M. Biermann, S. Bouquillon, G. Bourda, T. Brüsemeister, B. Bucciarelli, D. Busonero, T. Carlucci, J. Castañeda, P. Charlot, M. Clotet, M. Crosta, M. Davidson, F. de Felice, R. Drimmel, C. Fabricius, A. Fienga, F. Figueras, E. Fraile, M. Gai, N. Garralda, R. Geyer, J. J. González-Vidal, R. Guerra, N. C. Hambly, M. Hauser, S. Jordan, M. G. Lattanzi, H. Lenhardt, S. Liao, W. Löffler, P. J. McMillan, F. Mignard, A. Mora, R. Morbidelli, J. Portell, A. Riva, M. Sarasso, I. Serraller, H. Siddiqui, R. Smart, A. Spagna, U. Stampa, I. Steele, F. Taris, J. Torra, W. van Reeven, A. Vecchiato, S. Zschocke, J. de Bruijne, G. Gracia, F. Raison, T. Lister, J. Marchant, R. Messineo, M. Soffel, J. Osorio, A. de Torres, and W. O’Mullane. Gaia Data Release 1. Astrometry: one billion positions, two million proper motions and parallaxes. *A&A*, 595:A4, November 2016. doi: 10.1051/0004-6361/201628714.

C. J. Lintott, K. Schawinski, A. Slosar, K. Land, S. Bamford, D. Thomas, M. J. Raddick, R. C. Nichol, A. Szalay, D. Andreescu, P. Murray, and J. Vandenberg. Galaxy Zoo: morphologies derived from visual inspection of galaxies from the Sloan Digital Sky Survey. *MNRAS*, 389:1179–1189, September 2008. doi: 10.1111/j.1365-2966.2008.13689.x.

R. A. Mardling and S. J. Aarseth. Tidal interactions in star cluster simulations. *MNRAS*, 321:398–420, March 2001. doi: 10.1046/j.1365-8711.2001.03974.x.

- G. Matijevič, A. Prša, J. A. Orosz, W. F. Welsh, S. Bloemen, and T. Barclay. Kepler Eclipsing Binary Stars. III. Classification of Kepler Eclipsing Binary Light Curves with Locally Linear Embedding. *AJ*, 143:123, May 2012. doi: 10.1088/0004-6256/143/5/123.
- P. Mayer. Eclipsing binaries with light-time effect. *Bulletin of the Astronomical Institutes of Czechoslovakia*, 41:231–236, July 1990.
- T. Mazeh and J. Shaham. The orbital evolution of close triple systems - The binary eccentricity. *A&A*, 77:145–151, August 1979.
- K. J. Michell and P. Plavchan. Period Error Estimation for the Kepler Eclipsing Binary Catalog. *AJ*, 145:148, June 2013. doi: 10.1088/0004-6256/145/6/148.
- S. Mikkola. Dynamics and Stability of Triple Stars. In S. Hubrig, M. Petr-Gotzens, and A. Tokovinin, editors, *Multiple Stars Across the H-R Diagram*, page 11, 2008. doi: 10.1007/978-3-540-74745-1\_2.
- E. Moreno, G. Koenigsberger, and D. M. Harrington. Eccentric binaries. Tidal flows and periastron events. *A&A*, 528:A48, April 2011. doi: 10.1051/0004-6361/201015874.
- F. Mullally, J. L. Coughlin, S. E. Thompson, J. Rowe, C. Burke, D. W. Latham, N. M. Batalha, S. T. Bryson, J. Christiansen, C. E. Henze, A. Ofir, B. Quarles, A. Shporer, V. Van Eylen, C. Van Laerhoven, Y. Shah, A. Wolfgang, W. J. Chaplin, J.-W. Xie, R. Akeson, V. Argabright, E. Bachtell, T. Barclay, W. J. Borucki, D. A. Caldwell, J. R. Campbell, J. H. Catanzarite, W. D. Cochran, R. M. Duren, S. W. Fleming, D. Fraquelli, F. R. Girouard, M. R. Haas, K. G. Hełminiak, S. B. Howell, D. Huber, K. Larson, T. N. Gautier, III, J. M. Jenkins, J. Li, J. J. Lissauer, S. McArthur, C. Miller, R. L. Morris, A. Patil-Sabale, P. Plavchan, D. Putnam, E. V. Quintana, S. Ramirez, V. Silva Aguirre, S. Seader, J. C. Smith, J. H. Steffen, C. Stewart, J. Stober, M. Still, P. Tenenbaum, J. Troeltzsch, J. D. Twicken, and K. A. Zamudio. Planetary Candidates Observed by

Kepler. VI. Planet Sample from Q1–Q16 (47 Months). *ApJS*, 217:31, April 2015. doi: 10.1088/0067-0049/217/2/31.

S. Naoz and D. C. Fabrycky. Mergers and Obliquities in Stellar Triples. *ApJ*, 793:137, October 2014. doi: 10.1088/0004-637X/793/2/137.

S. Naoz, W. M. Farr, Y. Lithwick, F. A. Rasio, and J. Teyssandier. Secular dynamics in hierarchical three-body systems. *MNRAS*, 431:2155–2171, May 2013a. doi: 10.1093/mnras/stt302.

S. Naoz, B. Kocsis, A. Loeb, and N. Yunes. Resonant Post-Newtonian Eccentricity Excitation in Hierarchical Three-body Systems. *ApJ*, 773:187, August 2013b. doi: 10.1088/0004-637X/773/2/187.

C. P. Nicholls and P. R. Wood. Eccentric ellipsoidal red giant binaries in the LMC: complete orbital solutions and comments on interaction at periastron. *MNRAS*, 421:2616–2628, April 2012. doi: 10.1111/j.1365-2966.2012.20492.x.

J. A. Orosz. Triple Stars Observed by Kepler. In S. M. Rucinski, G. Torres, and M. Zejda, editors, *Living Together: Planets, Host Stars and Binaries*, volume 496 of *Astronomical Society of the Pacific Conference Series*, page 55, July 2015.

B. Paczyński, D. M. Szczygieł, B. Pilecki, and G. Pojmański. Eclipsing binaries in the All Sky Automated Survey catalogue. *MNRAS*, 368:1311–1318, May 2006. doi: 10.1111/j.1365-2966.2006.10223.x.

A. Pál. Light-curve modelling for mutual transits. *MNRAS*, 420:1630–1635, February 2012. doi: 10.1111/j.1365-2966.2011.20151.x.

M. Parvizi, M. Paegert, and K. G. Stassun. The Eb Factory Project. II. Validation With the Kepler Field in Preparation for K2 and Tess. *AJ*, 148:125, December 2014. doi: 10.1088/0004-6256/148/6/125.

M. Pettini. Structure and evolution of stars lecture 18. <http://www.ast.cam.ac.uk/~pettini/STARS/Lecture18.pdf>, June 2013. [Online; accessed 28-February-2018].

A. Prša and T. Zwitter. A Computational Guide to Physics of Eclipsing Binaries. I. Demonstrations and Perspectives. *ApJ*, 628:426–438, July 2005. doi: 10.1086/430591.

A. Prša, E. F. Guinan, E. J. Devinney, M. DeGeorge, D. H. Bradstreet, J. M. Giamarco, C. R. Alcock, and S. G. Engle. Artificial Intelligence Approach to the Determination of Physical Properties of Eclipsing Binaries. I. The EBAI Project. *ApJ*, 687:542-565, November 2008. doi: 10.1086/591783.

A. Prša, N. Batalha, R. W. Slawson, L. R. Doyle, W. F. Welsh, J. A. Orosz, S. Seager, M. Rucker, K. Mjaseth, S. G. Engle, K. Conroy, J. Jenkins, D. Caldwell, D. Koch, and W. Borucki. Kepler Eclipsing Binary Stars. I. Catalog and Principal Characterization of 1879 Eclipsing Binaries in the First Data Release. *AJ*, 141:83, March 2011a. doi: 10.1088/0004-6256/141/3/83.

A. Prša, J. Pepper, and K. G. Stassun. Expected Large Synoptic Survey Telescope (LSST) Yield of Eclipsing Binary Stars. *AJ*, 142:52, August 2011b. doi: 10.1088/0004-6256/142/2/52.

A. Prša, A. Robin, and T. Barclay. Stellar statistics along the ecliptic and the impact on the K2 mission concept. *International Journal of Astrobiology*, 14:165–172, April 2015. doi: 10.1017/S1473550414000329.

A. Prša, K. E. Conroy, M. Horvat, H. Pablo, A. Kochoska, S. Bloemen, J. Giamarco, K. M. Hambleton, and P. Degroote. Physics Of Eclipsing Binaries. II. Toward the Increased Model Fidelity. *ApJS*, 227:29, December 2016. doi: 10.3847/1538-4365/227/2/29.

R. R. Rafikov. Stellar Proper Motion and the Timing of Planetary Transits. *ApJ*, 700: 965–970, August 2009. doi: 10.1088/0004-637X/700/2/965.

- S. Rappaport, K. Deck, A. Levine, T. Borkovits, J. Carter, I. El Mellah, R. Sanchis-Ojeda, and B. Kalomeni. Triple-star Candidates among the Kepler Binaries. *ApJ*, 768:33, May 2013. doi: 10.1088/0004-637X/768/1/33.
- G. Rauw, S. Rosu, A. Noels, L. Mahy, J. H. M. M. Schmitt, M. Godart, M.-A. Dupret, and E. Gosset. Apsidal motion in the massive binary HD 152218. *A&A*, 594:A33, October 2016. doi: 10.1051/0004-6361/201628766.
- H. Rein and S.-F. Liu. REBOUND: an open-source multi-purpose N-body code for collisional dynamics. *A&A*, 537:A128, January 2012. doi: 10.1051/0004-6361/201118085.
- H. Rein and D. S. Spiegel. IAS15: a fast, adaptive, high-order integrator for gravitational dynamics, accurate to machine precision over a billion orbits. *MNRAS*, 446:1424–1437, January 2015. doi: 10.1093/mnras/stu2164.
- H. Rein and D. Tamayo. WHFAST: a fast and unbiased implementation of a symplectic Wisdom-Holman integrator for long-term gravitational simulations. *MNRAS*, 452:376–388, September 2015. doi: 10.1093/mnras/stv1257.
- H. Rein and S. Tremaine. Symplectic integrators in the shearing sheet. *MNRAS*, 415: 3168–3176, August 2011. doi: 10.1111/j.1365-2966.2011.18939.x.
- N. D. Richardson, A. F. J. Moffat, R. Maltais-Tariant, H. Pablo, D. R. Gies, H. Saio, N. St-Louis, G. Schaefer, A. S. Miroshnichenko, C. Farrington, E. J. Aldoeretta, É. Artigau, T. S. Boyajian, K. Gordon, J. Jones, R. Matson, H. A. McAlister, D. O’Brien, D. Raghavan, T. Ramiaramanantsoa, S. T. Ridgway, N. Scott, J. Sturmann, L. Sturmann, T. t. Brummelaar, J. D. Thomas, N. Turner, N. Vargas, S. Zharikov, J. Matthews, C. Cameron, D. Guenther, R. Kuschnig, J. Rowe, S. Rucinski, D. Sasselov, and W. Weiss. Spectroscopy, MOST photometry, and interferometry of MWC 314: is it an LBV or an interacting binary? *MNRAS*, 455:244–257, January 2016. doi: 10.1093/mnras/stv2291.

G. R. Ricker, J. N. Winn, R. Vanderspek, D. W. Latham, G. Á. Bakos, J. L. Bean, Z. K. Berta-Thompson, T. M. Brown, L. Buchhave, N. R. Butler, R. P. Butler, W. J. Chaplin, D. Charbonneau, J. Christensen-Dalsgaard, M. Clampin, D. Deming, J. Doty, N. De Lee, C. Dressing, E. W. Dunham, M. Endl, F. Fressin, J. Ge, T. Henning, M. J. Holman, A. W. Howard, S. Ida, J. M. Jenkins, G. Jernigan, J. A. Johnson, L. Kaltenegger, N. Kawai, H. Kjeldsen, G. Laughlin, A. M. Levine, D. Lin, J. J. Lissauer, P. MacQueen, G. Marcy, P. R. McCullough, T. D. Morton, N. Narita, M. Paegert, E. Palle, F. Pepe, J. Pepper, A. Quirrenbach, S. A. Rinehart, D. Sasselov, B. Sato, S. Seager, A. Sozzetti, K. G. Stassun, P. Sullivan, A. Szentgyorgyi, G. Torres, S. Udry, and J. Villasenor. Transiting Exoplanet Survey Satellite (TESS). *Journal of Astronomical Telescopes, Instruments, and Systems*, 1(1):014003, January 2015. doi: 10.1117/1.JATIS.1.1.014003.

S. T. Roweis and L. K. Saul. Nonlinear Dimensionality Reduction by Locally Linear Embedding. *Science*, 290:2323–2326, December 2000. doi: 10.1126/science.290.5500.2323.

C. A. Scharf. Exoplanet Transit Parallax. *ApJ*, 661:1218–1221, June 2007. doi: 10.1086/517504.

G. Schwarz. Estimating the Dimension of a Model. *Annals of Statistics*, 6:461–464, July 1978.

I. S. Shklovskii. Possible Causes of the Secular Increase in Pulsar Periods. *Soviet Ast.*, 13: 562, February 1970.

R. W. Slawson, A. Prša, W. F. Welsh, J. A. Orosz, M. Rucker, N. Batalha, L. R. Doyle, S. G. Engle, K. Conroy, J. Coughlin, T. A. Gregg, T. Fetherolf, D. R. Short, G. Windmiller, D. C. Fabrycky, S. B. Howell, J. M. Jenkins, K. Uddin, F. Mullally, S. E. Seader, S. E. Thompson, D. T. Sanderfer, W. Borucki, and D. Koch. Kepler Eclipsing Binary Stars.

II. 2165 Eclipsing Binaries in the Second Data Release. *AJ*, 142:160, November 2011.  
doi: 10.1088/0004-6256/142/5/160.

S. Soderhjelm. AY Mus: a Triple System? *Information Bulletin on Variable Stars*, 885, April 1974.

S. Soderhjelm. The three-body problem and eclipsing binaries - Application to algol and lambda Tauri. *A&A*, 42:229–236, August 1975.

S. Soderhjelm. Studies of the stellar three-body problem. *A&A*, 107:54–60, March 1982.

K. G. Stassun. Astrophysics: A pas de trois birth for wide binary stars. *Nature*, 492: 191–192, December 2012. doi: 10.1038/nature11762.

K. G. Stassun, G. A. Feiden, and G. Torres. Empirical tests of pre-main-sequence stellar evolution models with eclipsing binaries. *NewAR*, 60:1–28, June 2014. doi: 10.1016/j.newar.2014.06.001.

K. Stępień and M. Kiraga. Evolution of Cool Close Binaries - Rapid Mass Transfer and Near Contact Binaries. *AcA*, 63:239–266, June 2013.

J. Teyssandier, S. Naoz, I. Lizarraga, and F. A. Rasio. Extreme Orbital Evolution from Hierarchical Secular Coupling of Two Giant Planets. *ApJ*, 779:166, December 2013. doi: 10.1088/0004-637X/779/2/166.

S. E. Thompson, M. Everett, F. Mullally, T. Barclay, S. B. Howell, M. Still, J. Rowe, J. L. Christiansen, D. W. Kurtz, K. Hambleton, J. D. Twicken, K. A. Ibrahim, and B. D. Clarke. A Class of Eccentric Binaries with Dynamic Tidal Distortions Discovered with Kepler. *ApJ*, 753:86, July 2012. doi: 10.1088/0004-637X/753/1/86.

I. Todoran. On the Orbital Eccentricity of an Eclipsing Binary System. *Ap&SS*, 15:229–235, February 1972. doi: 10.1007/BF00649917.

- A. Tokovinin. Comparative statistics and origin of triple and quadruple stars. *MNRAS*, 389:925–938, September 2008. doi: 10.1111/j.1365-2966.2008.13613.x.
- A. Tokovinin. From Binaries to Multiples. I. Data on F and G Dwarfs within 67 pc of the Sun. *AJ*, 147:86, April 2014a. doi: 10.1088/0004-6256/147/4/86.
- A. Tokovinin. From Binaries to Multiples. II. Hierarchical Multiplicity of F and G Dwarfs. *AJ*, 147:87, April 2014b. doi: 10.1088/0004-6256/147/4/87.
- A. Tokovinin, S. Thomas, M. Sterzik, and S. Udry.
- A. A. Tokovinin. On the multiplicity of spectroscopic binary stars. *Astronomy Letters*, 23: 727–730, November 1997.
- G. Torres. The Change in the Inclination Angle of the Noneclipsing Binary SS Lacertae: Future Eclipses. *AJ*, 121:2227–2238, April 2001. doi: 10.1086/319942.
- G. Torres, J. Andersen, and A. Giménez. Accurate masses and radii of normal stars: modern results and applications. *A&A Rv*, 18:67–126, February 2010. doi: 10.1007/s00159-009-0025-1.
- K. Tran, A. Levine, S. Rappaport, T. Borkovits, S. Csizmadia, and B. Kalomeni. The Anticorrelated Nature of the Primary and Secondary Eclipse Timing Variations for the Kepler Contact Binaries. *ApJ*, 774:81, September 2013. doi: 10.1088/0004-637X/774/1/81.
- J. Tyson and Collaboration LSST. The large synoptic survey telescope: Opening new windows. *American Astronomical Society Meeting Abstracts*, 201:134.01, 2002.
- A. Vanderburg and J. A. Johnson. A Technique for Extracting Highly Precise Photometry for the Two-Wheeled Kepler Mission. , 126:948, October 2014. doi: 10.1086/678764.

Bala R. Vatti. A generic solution to polygon clipping. *Commun. ACM*, 35(7):56–63, July 1992. ISSN 0001-0782. doi: 10.1145/129902.129906. URL <http://doi.acm.org/10.1145/129902.129906>.

Gordon Walker, Jaymie Matthews, Rainer Kuschnig, Ron Johnson, Slavek Rucinski, John Pazder, Gregory Burley, Andrew Walker, Kristina Skaret, Robert Zee, Simon Grocott, Kieran Carroll, Peter Sinclair, Don Sturgeon, and John Harron. The most asteroseismology mission: Ultraprecise photometry from space. *Publications of the Astronomical Society of the Pacific*, 115:1023, 2003. doi: 10.1086/377358.

R. E. Wilson. Eccentric orbit generalization and simultaneous solution of binary star light and velocity curves. *ApJ*, 234:1054–1066, December 1979. doi: 10.1086/157588.

R. E. Wilson. Computation Methods and Organization for Close Binary Observables. In K.-C. Leung and I.-S. Nha, editors, *New Frontiers in Binary Star Research*, volume 38 of *Astronomical Society of the Pacific Conference Series*, page 91, January 1993.

R. E. Wilson. Eclipsing Binary Solutions in Physical Units and Direct Distance Estimation. *ApJ*, 672:575-589, January 2008. doi: 10.1086/523634.

R. E. Wilson and E. J. Devinney. Realization of Accurate Close-Binary Light Curves: Application to MR Cygni. *ApJ*, 166:605, June 1971. doi: 10.1086/150986.

R. E. Wilson and W. Van Hamme. Unification of Binary Star Ephemeris Solutions. *ApJ*, 780:151, January 2014. doi: 10.1088/0004-637X/780/2/151.

J. Wisdom and M. Holman. Symplectic maps for the n-body problem. *AJ*, 102:1528–1538, October 1991. doi: 10.1086/115978.

J.-P. Zahn. Tidal dissipation in binary systems. In M.-J. Goupil and J.-P. Zahn, editors, *EAS Publications Series*, volume 29 of *EAS Publications Series*, pages 67–90, 2008. doi: 10.1051/eas:0829002.